This thesis was submitted for examination in June 2008. It does not necessarily represent the final form of the thesis as deposited in the University after examination.

U N I V E R S I T Y O F S O U T H A M P T O N

High-Throughput Synthesis and Characterization of Vanadium Mixed Metal Oxide Pigments Using Synchrotron Radiation

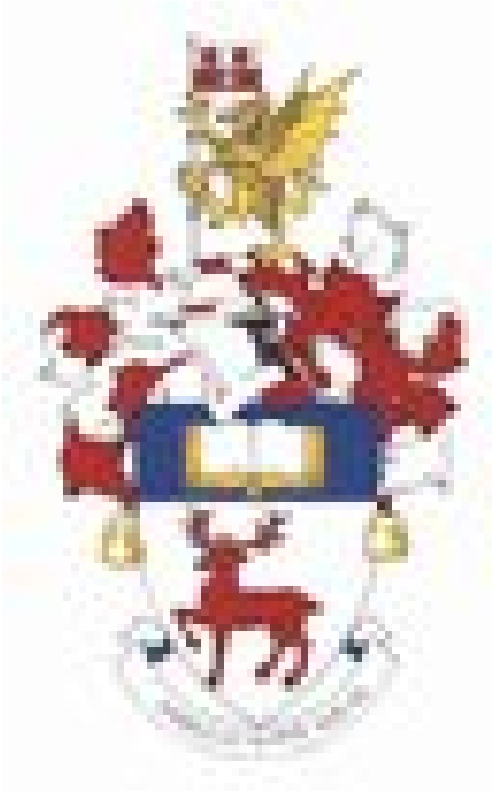

A thesis submitted for the Degree of Doctor of Philosophy

by

Sergio Russu

SCHOOL OF CHEMISTRY

FACULTY OF SCIENCE, ENGINEERING AND MATHEMATICS

June 2008

UNIVERSITY OF SOUTHAMPTON

ABSTRACT

FACULTY OF SCIENCE, ENGINEERING AND MATHEMATICS
SCHOOL OF CHEMISTRY

Doctor of Philosophy

High-Throughput Synthesis and Characterization of Vanadium Mixed Metal Oxide Pigments Using Synchrotron Radiation

By Sergio Russu

A range of inorganic vanadium mixed metal oxides, with potential applications as inorganic pigments, have been synthesised and characterised in terms of their crystal structure, and band gap energies using powder X-ray diffraction (PXD), synchrotron-based X-ray absorption fine structure (XAFS) spectroscopy, solid state UV-Visible and Raman spectroscopy, Scanning and Transmission electron microscopy (SEM and TEM).

Vanadium mixed metal oxide BiMeVOX with Me = Mo, Cu and Fe, and calcium pyrovanadate with Me = Pb, Cd, Sr, doped systems, have been synthesised in sequential and high throughput array by peroxo sol-gel methods and calcined at 700°C in an oxygen atmosphere. Powder X-ray diffraction studies show the synthesised BiMoVOX ($Bi_{1-x/3}Mo_{1-x}V_xO_4$) to have a tetragonal crystal structure in the space group *I 41/a*, BiCuVOX and BiFeVOX ($Bi_2V_{1-x}Me_xO_{5.5-\delta}$) to have a tetragonal crystal structure in the space group *I 4/mmm*, and pyrovanadate ($(Ca_{2-x},Me_x)V_2O_7$) to have triclinic in the space group *P-1*. PXD profiles have displayed phase transitions from monoclinic to tetragonal crystal phase together with peak positions shift, reflecting the changes in d-spacing and consequent volume cell growth by incorporation of the different ions into BiMeVOX; the calcium pyrovanadate kept their triclinic crystal structure.

Raman and XAFS spectroscopy data analysis have shown isolated metal-oxygen tetrahedra for both vanadium and molybdenum cations in the BiMoVOX materials. Vanadium coordination in both the BiFeVOX and the BiCuVOX materials is more complex with three different cases: octahedral distorted, trigonal bipyramid and tetragonal; these structure consists of alternating layers of $[Bi_2O_2]^{2+}$ and $[VO_{3.5}\check{I}_{0.5}]^{2-}$, where Ĭ represents oxide ion vacancies. Calcium pyrovanadate materials display vanadium-oxygen polyhedra for a tetrameric chain comprising two edge-shared VO_5 pyramids, and each also sharing a corner with a VO_4 tetrahedron.

UV-Visible spectroscopy of these materials reveals broad reflectance bands and a steep absorption edge, which is directly related to the band gap energy of the compound. By varying the doping levels on the vanadium and calcium site with different cations the colour of the compounds can be seen to visibly alter. This can be attributed to a modification in the band gap energies as direct result of the fine-tuning of the electronegativity difference between cations and anions, their overall contribution to the molecular orbitals of the materials, and the total concentration of oxygen vacancies.

SEM and TEM analysis showed a more round particle shape for samples made by the peroxo sol-gel reaction compared to samples made by calcinations reaction in the BiMoVOX series.

DECLARATION

The material in this Thesis has not been submitted for examination for any other degree or part thereof, at the University of Southampton or any other institution. At no time during the registration for the degree of Doctor of Philosophy has the author been registered for any other university award. The material contained herein is the sole work of the author except where formally acknowledged by reference.

Signed ……..

Date ……..

ACKNOWLEDGEMENTS

Foremost I am very grateful to my supervisor, Professor John Evans, for his continual encouragement and support. His academic guidance throughout this project has been most appreciated.

In addition, I would like to thank Professor Mark Weller for his expert advice and helpful assistance over the past three years in the art of pigment synthesis and characterisation. I would also like to thank Dr. Moniek Tromp for her technical and scientific support during the High-Throughput project.

I would also like to express thanks to the EPSRC for their contribution to the funding of my PhD and the conferences I have attended.

I thank all the people involved in the High-Throughput project for their constant scientific support during these three years.

I would like to acknowledge Mr Norman Binsted for his valuable scientific support, and for his help in doing the RMC calculation for the BiMoVOX materials.

Thanks to Dr. Stuart Henderson for his practical advice on the High-Throughput synthesis techniques, and Mr Peter Hickey for passing on his invaluable GSAS knowledge.

Thank you to Miss Alexandra Lieb and Miss Eleni Kotsapa for their kind help with the drawing of the crystal structure.

I also must thank the Evans group and everyone else who has worked within the Weller group during the past three years.

A special mention must go to Josefine, Terence, Vassili, Nikos, Sue, Benedetta, Marcella, Simona, Paolo, Michal, Ewa, Ania, Karol, Peter, Sarah, Otello, Rosa, Peppe, Maria, Gerardo, Pietro, Riccardo, Luca, Claudia, and to the Italian, Greek & Polish communities for the unique and unforgettable time we had together in these three years.

Finally, I would like to thank my family for all their encouragement and support.

ABBREVIATIONS

Some commonly used abbreviations in this work:

HTP	High-Throughput
PXD	Powder X-ray Diffraction
XAFS	X-Ray Absorption Fine Structure
EXAFS	Extended X-Ray Absorption Fine Structure
XANES	X-Ray Absorption Near Edge Structure
SEM	Scanning Electron Microscopy
TEM	Transmission Electron Microscopy
UV-Vis	Ultraviolet-Visible
FWHM	Full Width at Half Maximum
JCPDS	Joint Committee on Powder Diffraction Standards
RMC	Reverse Monte-Carlo
GSAS	General Structure Analysis System

TABLE OF CONTENTS

CHAPTER TWO:

CHAPTER THREE:

CHAPTER FOUR:

CHAPTER FIVE:

CHAPTER SIX:

CHAPTER SEVEN:

CHAPTER ONE

INTRODUCTION

Chapter One: Introduction

1.1 Inorganic Pigments

1.1.1 Definition of a Pigment

The word “pigment” has its origin from the Latin language and it was used to indicate a substance that produces a characteristic colour in the matter. Nowadays the meanings of the word pigments indicate a finely divided material which contributes to optical and other properties of paint, finishes, and coatings [1]. In order to discriminate between dyes and pigments, as first approximation, we can say that pigments are insoluble in the coating material, whereas dyes dissolve in and colour the coating. Normally pigments are mechanically mixed with the coating and then deposited on a specific support.

The physical properties of pigments are generally not changed by incorporation and deposition from the vehicle. It is possible to classify the pigments according to their composition, inorganic or organic, or by their source, natural or synthetic. However, the most useful classification is by their colour (for example white, coloured or black) and by their use (for example in ceramics, paint, foods, cosmetics, and so on).

1.1.2 Classification of Pigments

The classification of the inorganic pigment, due to wide variety of pigments available on the market, can be done from different points of view. According with the optical process which could occurs once a beam of light rich the surface of a pigment (absorption, scattering or diffusion), it is possible to classify the inorganic pigments in five classes [1], Table 1.1.

Table 1.1 - Classification of inorganic pigments

Type	Optical effect
White pigments	Non-selective light scattering (e.g.: titanium dioxide and zinc sulphide pigments)
Coloured pigments	Selective light absorption and selective light scattering (e.g.: iron oxides, ultramarine and cadmium pigments)
Black pigments	Non-selective light absorption (e.g.: carbon black pigment and iron oxide black)
Lustre pigments	Regular reflection or interference (e.g.: aluminium flakes and titanium dioxide on mica)
Luminescent pigments	Capacity to absorb radiation and to emit it as light of a longer wavelength (e.g.: silver-doped zinc sulphide and copper-doped zinc sulphide)

1.1.3 Economic Aspect

Inorganic pigments productions represent about 95 % of world-wide pigments production. Furthermore, as a consequence of its wide range of applications the pigment industry is still a growth market. In Table 1.2, we confined our attention to the commercial developments of the coloured pigment sector [2].

Table 1.2 - Total world production of synthetic coloured inorganic pigments

Pigment	Production (10^3 tonnes/y)	Supplier	Country
Iron Oxide	500 – 580	Lanxess / Elementis / Rockwood	China/ Germany / Italy / U.S.
Manganese	150 - 200	Holliday Pigments / Nandolia	Northern - North-western Europe / U.S. / India
Ultramarine	80	Holliday Pigments / Nubiola / Dainichiseika	England / France / Spain / Japan
Mixed metal Oxide	30	Ferro / BASF / Ciba / Engelhard / Ishihara / Johnson Matthey	U.S. / Germany / China / Worldwide
Chromium Oxide	19	Elementis / Lanxess / Nippon Denko / Nippon Chemical	Germany / China / Japan
Zirconia	8.5 - 10	Ferro / Johnson Matthey	U.S. / Worldwide
Bismuth Vanadate	1.2	BASF / Ciba / Gebroeders C.	Germany / China / Belgium

Beside the synthetic production of Iron oxides, it is noteworthy to mention that the world production of natural iron oxide pigments estimated by the U.S. Geological Survey, is about 550.000 tonnes/y with India as the most important supplier.

1.2 Types of Coloured Pigments

1.2.1 Iron Oxide Pigments

As shown in Table 1.2, both the natural and the synthetic iron oxide pigments represent one of the most important sectors of the world-wide industrial coloured pigments production. The reason is behind either their non-toxicity, chemical stability, and their wide range of colours going from yellow, orange and red to brown and black pigments; furthermore they are also quite cheap to produce. Synthetic iron oxide pigments are mainly single-component form, and their colours are strongly related to the synthesis condition, i.e. particle size, particle size distribution and particle shape [1, 3]. For example haematite (α-Fe_2O_3) displays colour from red to dark violet [4, 5], goethite (α-FeOOH) displays colour form green-yellow to brown-yellow [6], and lepidocrocite (γ-FeOOH) displays colour from yellow to orange [7] together with the increasing of its particle size [8]. Another important iron oxide pigment is the magnetite (Fe_3O_4), which displays a black colour [9]; usually brown iron oxide pigments are made by reaction of α-FeOOH with small amount of manganese compounds.
Three mainly different industrial processes are used for the production of synthetic iron oxide pigments [1]:

- Solid state reaction (including calcinations, milling, thermal decomposition)
- Precipitation process (from solution of iron salts)
- Laux process (involving reduction of nitrobenzene)

Iron oxide pigments are mainly used in the construction and coating industries.

1.2.2 Manganese Pigments

Manganese pigments consist of homogeneous solutions of manganese dioxides mixed with, for example, titanium oxides to obtain brown manganese titanate, iron(II) oxide to obtain black spinel pigments, alkaline earth metal oxides, and chromium oxide to obtain coloured pigments [10]. These pigments are added into or applied onto materials such as paints, inks, plastics, glasses, ceramics, and for pigmenting building materials [1].

1.2.3 Ultramarine Pigments

The natural mineral *Lapis lazuli* normally called the ultramarine pigment displays a deep blue colour. Because of the few places around the world in which it was possible to find the best quality of this mineral together with the high request of it from the most famous artists in the 1800, it has been more expensive even than gold [11]. The ultramarine crystal structure can be seen as a three-dimensional aluminosilicate lattice with a sulphur group and sodium cation entrapped within the cavities of the lattice. Synthetic ultramarine pigments are commercially available in three different colours: reddish blue [12, 13], violet and pink [14, 15].
The industrial production of ultramarine is made from relative economic starting materials as china clay, feldspar, sodium carbonate, and sulphur; the process requires several steps with calcinations, blending, oxidation and purification/refinement [1].

1.2.4 Mixed Metal Oxide Pigments

Mixed metal oxide pigments displays a wide range of applications, such as paints, plastic, building materials, ceramics and coatings, due to their physical properties. From a chemical point of view, they are homogeneous solid solutions in which different metal oxides are uniformly distributed in one crystal lattice [1]. Mixed metal oxides consist of a well defined structure which can be modified by several different metal oxides in order to change their colour properties.
There are several types of mixed oxide pigments, with three mainly different crystal structures: rutile [16], spinel [17] and haematite [18]. Examples of pigments with a rutile structure are mixed Ni(II), Sb(V),Ti(IV) oxides (yellow pigment) or mixed Mn(II), Sb(V), Ti(IV) oxides (brown pigment); mixed Zn(II), Fe(II,III) oxides (yellow pigment) and mixed Co(II), Cr(III), Al(III) (blue pigment) belong to the spinel type pigments. Finally mixed Fe(II), Cr(III) oxides are an example of the hematite type pigments.

Mixed metal oxides pigments are synthesised by solid state reaction in the range of temperature between 800 and 1300 °C. The starting materials are usually oxides or salt of the metals (e.g. nitrate or carbonate) which are calcined together at the appropriate temperature. The relative proportions of the different metal oxides together with the calcination temperature are the most critical parameters to take into account during the synthesis processes.

1.2.5 Chromium Oxide Pigments

Chromium oxide pigment, Cr_2O_3, is one of the few green single-component pigments [19]. Similar green pigments are usually a mix of chrome-yellow with iron-blue pigments or chrome-yellow with blue phthalocyanine pigments [18]. They are industrially synthesised by either reduction of an alkali dichromate or of ammonium dichromate. Chromium oxides are used as pigment for toys, ceramics, plastic and paints industries.

1.2.6 Zirconia Pigments

Zirconia based pigments is a well known class of thermally stable pigments. Examples of these materials, in which the zirconium oxide is the host lattice [20], are zirconium praseodymium yellow [21], zirconium vanadium blue [22], zirconium iron pink [23]. Zirconium inclusion pigments in which colouring crystals, are found in particular cadmium sulphide or cadmium sulfoselenides are included in zirconium silicate [24]. Zirconia pigments are usually synthesised by either thermal or chemical processes, and they are mainly used in the ceramic and paint industries.

1.2.7 Bismuth Pigments

Bismuth orthovanadate based pigments belong to the wide range family of greenish yellow inorganic pigments [1]. They represent an interesting alternative for the more toxic greenish yellow lead chromate and cadmium sulphide pigments.

Even though $BiVO_4$ has three different natural mineral, orthorhombic pucherite, monoclinic clinobisvanite, and tetragonal dreyerite, it is mainly synthesised by the pigment industries [25]. Other pigments bismuth oxide based, as for example Bi_2XO_6 with X = Mo or W, are mixed together with $BiVO_4$ in order to obtain new class of greenish yellow pigments. Bismuth vanadate is generally synthesised with two different methods [1]:

- solid–state reactions (from Bi(III) and V(V) oxides)
- precipitation processes (from Bi(III) and V(V) salts)

The whole production of bismuth vanadate pigments is based on monoclinic and tetragonal $BiVO_4$; it has been reported that the meta-stable tetragonal $BiVO_4$ can be stabilised at upon metal doping (e.g. Ca and Mo) [26]. Colour and brilliance properties are strongly dependent, on the precipitation process and on the reaction conditions (e.g. temperature, and pH) [27-30]. Bismuth vanadates have a wide range of applications such as industrial and decorative paints, coatings, lead-free manufacture, and they are also use as base of different yellow / red / green colours.

1.3 The Origin of Colour

When a beam of light hits the surface of a material containing a pigment four different events may occur: *reflection* at the surface (specular or diffuse depending on whether if the surface is very smooth, or has some roughness), complete *scattering* if the surface is extremely rough (as in a fine powder or the foam on a liquid such a beer), *absorption* during the process of reflection at the surface for the part of the light which is not reflected or scattered at the surface, and *transmission* for that part of light which does not interact with both the surface or the bulk of the material [31].

The origin of the colour in pigments is, therefore, directly related to their light-absorption and light scattering properties. In white pigments the scattering process is predominant over the absorption process, vice versa for the black pigments. Coloured pigments display selective scattering and absorption (dependent on the wavelength of the incident light).

Excluding *vibrations and simple excitations*, which describe the colour caused by incandescence, gas excitations, vibrations and rotation, there are four different physical theories with which the colour of materials, caused by intrinsic constituents, impurities, defects, and particular structures, can be explained [32]:

- *Crystal field theory* (colour caused by transition metal compounds, transition metal impurities, and colour centers)

- *Molecular orbital theory* (colour caused by charge transfer electronic transitions and organic materials)

- *Band theory* (colour caused by conductors, semiconductors, and doped semiconductors)

- *Physical optics* (colour caused by dispersion, scattering, interference, and diffraction)

These numerous causes of colour in pigments make clear that, a deep understanding of the colour properties in a particular pigment system is necessary before it can be modified and improved. In the metal oxide and mixed metal oxide pigments in particular, a good knowledge of both their electronic and crystal structures is fundamental in order to correlate them with the colour properties of the pigments. Furthermore, their colour is affected by the presence of elements such as transition metals which have different number of oxidation states, size and electronegativity. Previous papers also reported that cation doping of a structure potentially leads to a fine tune of the colour properties of these materials [33, 34].

1.4 Electronic Transition

The colours of transition metal pigments arise from different types of charge transfer processes. In particular in the mixed metal oxides pigments a ligand to metal electronic transition is frequently involved, in which one electron moves, predominantly, from the ligand (oxygen) to the central atom (transition metal). The motion of the electron is produced by the absorption of light energy, and this result in a temporary change in the valence state of both ions. Other types of similar charge transfer processes that occur in transition metal compounds involve d-d and f-f transition mechanisms.

1.4.1 Charge Transfer Transition

One of the most used examples of the *heteronuclear intervalence charge transfer* transition is the blue sapphire, a variety of corundum (Al_2O_3), which has small concentrations of both Fe and Ti impurities [31]. The iron can be present either as Fe^{3+} or Fe^{2+}, while titanium is usually present as Ti^{4+}. If the Fe^{2+} and Ti^{4+} are both present and they also substitute the Al ion in adjacent sites, an interaction between the two doping metals will occur, and an electron will transfer from the Fe^{2+} to the Ti^{4+} by light absorption and back again.

Since the difference in energies between these two states is of about 2.11 eV, the absorption of energy will result in a deep blue colour. Furthermore, because a second Fe^{2+} - Ti^{4+} arrangement is possible, an extra electronic transition occurs in these materials. This second transition due to the farther distance between the two cations, 2.79 Å versus the 2.65 Å, has quite similar energy but much smaller intensity. The resulting absorption results in a blue-green colour of the materials.

Prussian blue is an example of *homonuclear intervalence charge transfer* transition involving only Fe, but in two different oxidation states such as Fe^{2+} and Fe^{3+}. In this blue pigment the Fe^{2+} and Fe^{3+} are both in octahedral coordination, but with different environments; the Fe^{2+} ions are coordinated to six carbon ligand (CN^- groups) whereas the Fe^{3+} ions are coordinated to six nitrogen (CN^-) and/or oxygen (H_2O) ligands [35, 36].

The yellow pigment crocoite, $PbCrO_4$, is an example of *ligand-to-metal charge transfer* transition [37]. In these electronic transitions highly charged cations, as in this case the Cr^{6+}, receive electrons from the surrounding oxygens resulting in strong absorption in the blue part of the visible spectrum. Similar transition occurs in orange dichromates, $K_2Cr_2O_7$ [38], yellow molybdate, $PbMoO_4$ [39], and permanganate salts such as the deep purple-red $KMnO_4$. In all these pigments the transition metal is in its maximum oxidation state and consequently in a d^0 ground-state configuration.
In many oxides materials these charge transfer transition occurs at so high an energy that the resulting absorption falls in the ultraviolet part of the spectrum, and consequently the oxides will result in no colour or its colour will be due to the presence of iron impurities.

Metal-to-ligand charge transfer transitions occur in materials such the red tris(bipyridyl)-iron(II), $[Fe(bipy)_3]^{2+}$, in which the ligand stabilize the low metal oxidation state. This transfer happens when a metal is in a low oxidation state and the ligand tends to have vacant π* orbitals (π acceptor orbitals) [40].

The deep blue colour of both the ultramarine and the lapis lazuli is an example of *anion-anion charge transfer* transition. The polysulfide units (S_3^-) are responsible for the strong absorption band in the yellow, leading to the deep blue colour [12-15, 31].

1.4.2 d-d Transition

When a transition metal ion, such as V, Cr, Mn, Fe, Co, Ni, and Cu, has partially filled *d* shells, electronic transitions can take place between its *d*-orbitals. An example of mixed metal oxide pigments which display this type of electronic transition is the aluminium oxide alumina (Al_2O_3) doped with 1% of chromium sesquioxide (Cr_2O_3) [31]. The pure aluminium oxide itself is known as white or colourless sapphire, but as soon as it is doped with chromium oxide the material acquires a red colour known as ruby. Since the *d-d* electronic transitions are responsible for the intense colour in such compounds, a good understanding of their electron distribution in the *d* orbitals is required, Figure 1.1. The first set of orbitals, $3d_{xy}$, $3d_{xz}$, and $3d_{yz}$ are known as the t_{2g} or t_2 set whereas the second group, $3d_z^2$, and $3d_{x^2-y^2}$ are known as the e_g or e set depending on whether they are in an octahedral or tetrahedral environment respectively.

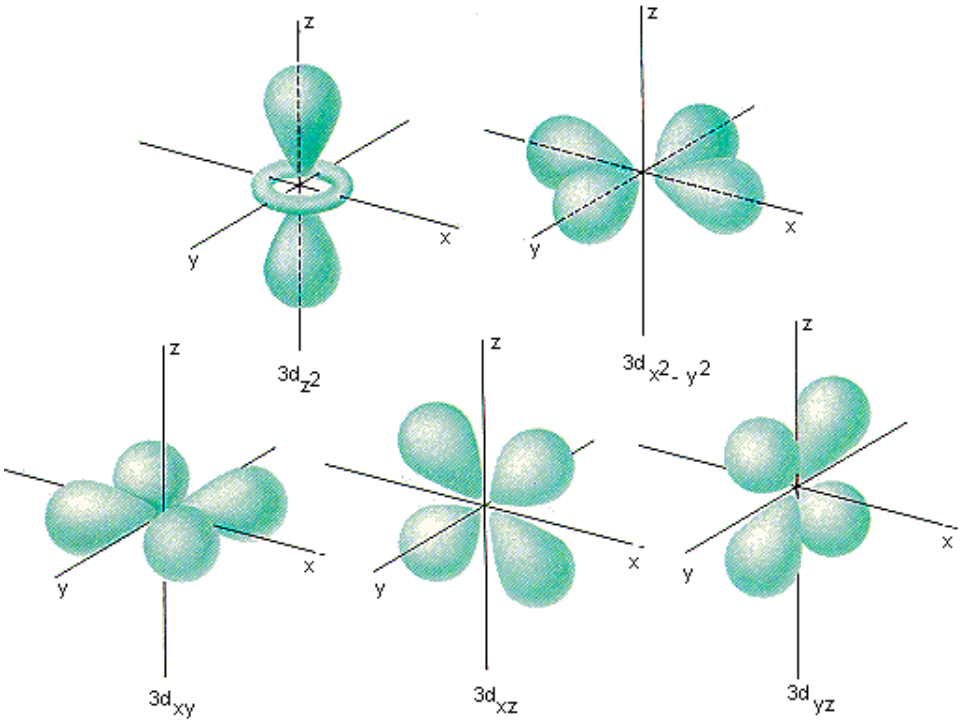

Fig. 1.1 – Schematic representation of the boundary surfaces and shapes of the five Cr^{3+} 3d orbitals [41]

A transition metal ion such as Cr^{3+} in isolation possesses degenerate *d* orbitals. The *d* orbital energies increase when located in a crystal due to increased repulsions exerted on the *d* electrons by the electron clouds of surrounding ligands. As the central metal ion is not spherical but has clearly defined regions of electron density the surrounding electrons are not evenly distributed and some *d*

orbitals are higher in energy than others thus generating an energy gap known as Δ_{oct}. This is known as crystal field splitting. This splitting is small and allows for $e_g \leftarrow t_{2g}$ transitions that usually correspond to absorptions within the visible region of the spectrum [19]. The magnitude of the splitting is seen in Figure 1.2.

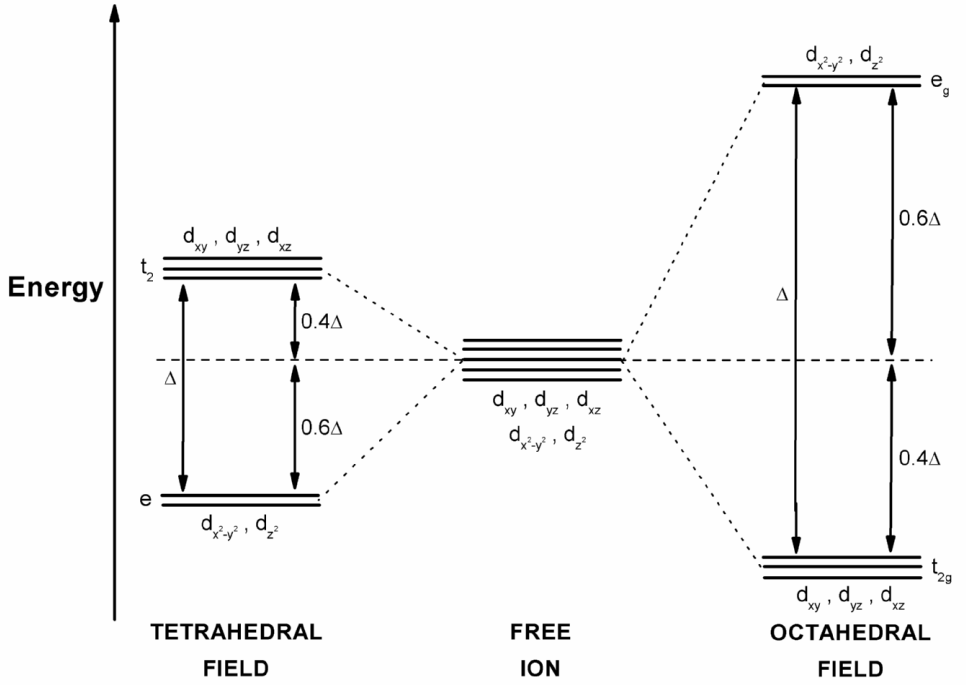

Fig. 1.2 – Splitting of the five 3d orbitals in an octahedral and a tetrahedral ligand field

For complexes in different symmetry environments, for example tetrahedral or square planar, interactions between ligands and *d* orbitals change. Thus the *d* orbitals are split in different ways according to geometry. The splitting in a tetrahedral environment, Δ_{tet}, is much smaller compared to Δ_{oct}. This is because there are only four negative ions as opposed to six and they are further away from the central metal ion.

The calculation of these energy levels is quite complex, and for a given central cation, one need to take into account several parameters that influence the final electronic level energies: cation valence state, symmetry of the ligands around the central cation, eventually distortion from the ideal octahedral or tetrahedral coordination geometry, and nature and strength of the bonding.

These electronic absorptions are not the only transitions responsible for the ruby colour in $Al_2O_3:Cr^{3+}$ doped systems. In fact the absorption process can leave the chromium ion in an excited state where the selection rules do not allow a return

from these states directly back to the ground state (Spin forbidden). As consequence, there will be an almost immediate transition from the excited states to an intermediate level which is permitted, with a production of a little heat within the ruby. Finally, the return from this intermediate level to the ground state, that is a permitted transition, will occur together with a red light emission also know as the R-line fluorescence of ruby [31, 40].

1.4.3 Intensity of Electronic Transition

The intensity of these electronic transitions is governed by a few selection rules [40]:

- *Spin selection rule* (transitions may occur only between energy states with the same spin multiplicity, *i.e*. $\Delta S = 0$)

- *Laporte selection rule* ($\Delta L = \pm 1$ and if the molecule is non-centrosymmetric, and from a *g* to a *u* state)

- *Symmetry selection rule* (product of symmetry of ground and excited states corresponds to *x*, *y* and *z* in the character tables)

The spin selection rule indicates that *d-d* transitions are spin allowed (excluding d^5 high spin) but from Laporte's rule these are formally forbidden in centrosymmetric environments such as octahedral coordination. They can arise either by a vibration or distortion that removes the centre of symmetry.
In the tetrahedral environment these *d-d* transitions are allowed, because there is not centre of symmetry, and therefore are more intense, tending to dominate a spectrum with respect to transitions within the octahedral environment, Table 1.3. The maximum molar absorption coefficient, ε_{max}, measures the strength of the absorption.

Table 1.3 - The intensity of electronic transitions in 3d complexes [40]

Band Type	Absorption Intensity ε_{max} (L mol^{-1} cm^{-1})	Type of Transition
Spin forbidden	< 1	d-d (Mn^{2+}, d^5)
Laporte forbidden	20 – 100	d-d (O_h)
Laporte allowed	*ca.* 250	d-d (T_d)
Fully symmetric allowed	1000 – 5000	charge transfer

1.4.4 Perception of Colour

What we call as visible light is just the narrow portion of the electromagnetic spectrum that our eyes can see, ranging from violet at one end (at about λ = 360 nm) to red at the other (at about λ = 780 nm), and passing through blue, green, yellow, and orange.

The photosensitive part of the eyes, the retina, is made by both rod and cone cells [31]. Rod cells are monochromatic and are therefore sensitive only to light and dark. There are three types of colour receptors, or cone cells, sensitive to a particular portion of the spectrum. The first cone cell is sensitive to *bluish-violet* light (with a maximum response at 440 nm), whereas the other two are most sensitive to greens; one at the *bluish-green* (with a maximum response at 545 nm) and the other at the *yellowish-green* (with a maximum response at 650 nm). Even though the cone cells have sensitive peak at different frequencies, there is a large degree of overlap with regard to the wavelengths of light to which the three types of cone cells respond. As a consequence, our visual systems are designed to detect differences between the responses of the different cones.

In order to do this, the retina have large numbers of comparator cells able to compare the signal generated by a number of different cone cells, and this is the signals coming out of the comparator cells that provide colour information to the brain. The result is that we perceive the colour yellow when our yellowish-green cones are stimulated slightly more than our bluish-green cones, for example; similarly, we perceive the colour red when our yellowish-green cones are stimulated significantly more than our bluish-green cones.

1.5 Scope of Work

The search for low-cost inorganic pigments with high thermal and chemical stability as a replacement for more expensive and less stable organic pigments has become a central theme in the modern pigment industry.

Synthesis and characterisation of mixed metal oxides in a sequential manner (one by one) in search of suitable pigments is very time-consuming, due to both the large number of syntheses required as function of doping, as well as the long calcination steps needed to obtain good quality (pure) crystalline samples. High throughput processing (HTP) methods, described in the third chapter of this thesis, provide a means of synthesising and testing large numbers of compounds rapidly and, when used in combination with traditional laboratory techniques, can provide an economically viable solution to the pursuit of novel materials [42-45]. Therefore, these techniques are particularly promising for the development of novel multi-component mixed metal oxide pigments.

This work describes the high throughput synthesis and characterisation of a range of vanadium mixed metal oxides, BiMeVOX (with Me = Mo, Fe, and Cu) and $(Ca,Me)_2V_2O_7$ (with Me = Cd, Pb, and Sr), which could potentially provide new classes of inorganic pigment. A detailed and systematic characterisation has been performed with a broad range of spectroscopic techniques in order to delineate the structure-function relationship of these pigments: combined X-ray absorption fine structure, X-ray powder diffraction, and Raman spectroscopy have been performed using a recently developed in situ apparatus [46], and also by UV-visible spectroscopy, transmission and scanning electron microscopy. New software for HTP XAS background subtraction (*X-MULT*) and a HTP version of *P* to perform combined EXAFS/XRD analyses for multiple spectra were also developed within these studies [47, 48].

1.6 References

1. G. Buxbaum, *Industrial Inorganic Pigments*. 2nd ed. **1998**, Weinheim, Wiley-VCH.
2. R. Adams, Foc. Pigm., **2007**, 1, 1-2.
3. L.J.R. Marshall, J.R. Williams, M.J. Almond, S.D.M. Atkinson, S.R. Cook*, et al.*, Spectroc. Acta Pt. A-Molec. Biomolec. Spectr., **2005**, 61, 233-241.
4. H. Katsuki and S. Komarneni, J. Am. Ceram. Soc., **2003**, 86, 183-185.
5. T.I. Bhuiyan, M. Nakanishi, Y. Kusano, T. Fujii, J. Takada*, et al.*, Mater. Lett., **2007**, 61, 3774-3777.
6. M. Elias, C. Chartier, G. Prevot, H. Garay, and C. Vignaud, Mater. Sci. Eng. B-Solid State Mater. Adv. Technol., **2006**, 127, 70-80.
7. S. Peulon, Q. Baraize, and A. Chausse, Electrochim. Acta, **2007**, 52, 7681-7688.
8. N. Randrianantoandro, A.M. Mercier, M. Hervieu, and J.M. Greneche, Mater. Lett., **2001**, 47, 150-158.
9. X.Y. Wang, G.Q. Yang, Z.S. Zhang, L.M. Yan, and J.H. Meng, Dyes Pigment., **2007**, 74, 269-272.
10. E. Ozel, G. Unluturk, and S. Turan, J. Eur. Ceram. Soc., **2006**, 26, 735-740.
11. S.E. Tarling, P. Barnes, and J. Klinowski, Acta Crystallogr. Sect. B-Struct. Commun., **1988**, 44, 128-135.
12. D.G. Booth, S.E. Dann, and M.T. Weller, Dyes Pigm., **2003**, 58, 73-82.
13. J. Fabian, N. Komiha, R. Linguerri, and P. Rosmus, Theochem-J. Mol. Struct., **2006**, 801, 63-69.
14. A.A. Landman and D. De Waal, Mater. Res. Bull., **2004**, 39, 655-667.
15. R.J.H. Clark, T.J. Dines, and M. Kurmoo, Inorg. Chem., **1983**, 22, 2766-2772.
16. F. Matteucci, G. Cruciani, M. Dondi, and M. Raimondo, Ceram. Int., **2006**, 32, 385-392.
17. G.Q. Yang, B. Han, Z.T. Sun, L.M. Yan, and X.Y. Wang, Dyes Pigm., **2002**, 55, 9-16.
18. E. Ozel and S. Turan, J. Eur. Ceram. Soc., **2003**, 23, 2097-2104.
19. M. Shirpour, M.A.F. Sani, and A. Mirhabibi, Ceram. Int., **2007**, 33, 1427-1433.
20. M. Dondi, F. Matteucci, and G. Cruciani, J. Sol. St. Chem., **2006**, 179, 233-246.

21. G. Del Nero, G. Cappelletti, S. Ardizzone, P. Fermo, and S. Gilardoni, J. Eur. Ceram. Soc., **2004**, 24, 3603-3611.
22. M. Llusar, J.B. Vicent, J. Badenes, M.A. Tena, and G. Monros, J. European Ceram. Soc., **1999**, 19, 2647-2657.
23. G. Cappelletti, S. Ardizzone, P. Fermo, and S. Gilardoni, J. European Ceram. Soc., **2005**, 25, 911-917.
24. A.L. Costa, F. Matteucci, M. Dondi, I. Zama, S. Albonetti*, et al.*, J. Eur. Ceram. Soc., **2008**, 28, 169-176.
25. P. Wood and F.R. Glasser, Ceram. Int., **2004**, 30, 875-882.
26. A.W. Sleight, H.Y. Chen, A. Ferretti, and D.E. Cox, Mater. Res. Bull., **1979**, 14, 1571-1581.
27. A. Tucks and H.P. Beck, J. Sol. St. Chem., **2005**, 178, 1145-1156.
28. M.A.B. Barata, M.C. Neves, C.P. Neto, and T. Trindade, Dyes Pigm., **2005**, 65, 125-127.
29. M. Gotic, S. Music, M. Ivanda, M. Soufek, and S. Popovic, J. Mol. Struct., **2005**, 744, 535-540.
30. J.B. Liu, H. Wang, S. Wang, and H. Yan, Mater. Sci. Eng. B-Solid State Mater. Adv. Technol., **2003**, 104, 36-39.
31. K. Nassau, *The Physics and Chemistry of Color*. 2nd ed. **2001**, New York, Wiley Interscience.
32. K. Nassau, Amer. Miner., **1978**, 63, 219-229.
33. H.W. Eng, P.W. Barnes, B.M. Auer, and P.M. Woodward, J. Sol. St. Chem., **2003**, 175, 94-109.
34. W.F. Yao and J.H. Ye, J. Phys. Chem. B, **2006**, 110, 11188-11195.
35. F. Herren, P. Fischer, A. Ludi, and W. Halg, Inorg. Chem., **1980**, 19, 956-959.
36. T. Uemura, M. Ohba, and S. Kitagawa, Inorg. Chem., **2004**, 43, 7339-7345.
37. G. Zhou, M. Lu, F. Gu, S. Wang, Z. Xiu*, et al.*, J. Cryst. Growth, **2004**, 270, 283–287.
38. T.J.R. Weakley, E.R. Ylvisaker, R.J. Yager, J.E. Stephens, R.D. Wiegel*, et al.*, Acta Crystallogr. Sect. B-Struct. Commun., **2004**, 60, 705-715.
39. J.Y. Chen, Q.R. Zhang, T.Y. Liu, and Z.X. Shao, Physica B, **2008**, 403, 555-558.
40. D.F. Shriver, P.W. Atkins, and C.H. Langford, *Inorganic Chemistry*. Second ed. **1993**, Oxford, Oxford Science Publications.
41. www.chemed.chem.purdue.edu.

42. D.A. Kukuruznyak, H. Reichert, J. Okasinski, H. Dosch, T. Chikyow*, et al.*, Appl. Phys. Lett., **2007**, 91, 071916(1-3).
43. J. Noh, Y.D. Suh, Y.K. Park, S.M. Jin, S.H. Kim*, et al.*, Rev. Sci. Instrum., **2007**, 78, 072205(1-6).
44. J.R. Hattrick-Simpers, C. Jun, M. Murakami, A. Orozco, L. Knauss*, et al.*, Appl. Surf. Sci., **2007**, 254, 734-737.
45. S.J. Henderson, J.A. Armstrong, A.L. Hector, and M.T. Weller, J. Mater. Chem., **2005**, 15, 1528-1536.
46. M. Tromp, S. Russu, A.J. Dent, J.F.W. Mosselmans, J. Evans*, et al.*, A.I.P., **2007**, CP 882, 858-860.
47. N. Binsted, *X-Mult*. University of Southampton, Southampton, **2006**.
48. N. Binsted, M.J. Pack, M.T. Weller, and J. Evans, J. Am. Chem. Soc., **1996**, 118, 10200-10210.

CHAPTER TWO

EXPERIMENTAL TECHNIQUES

Chapter Two: Experimental Techniques

2.1 Introduction

The synthesis and analysis of the inorganic pigments performed in this study can be divided in two categories: standard *solid state* and *high-throughput* methods. In this second chapter the theory of the techniques used for both methods, together with the instrumentation used for the analysis of the sequential materials, is described. In the third chapter the specific high-throughput methods developed to synthesise and analyse arrays are presented.

Powder X-ray diffraction (PXD), X-ray absorption fine-structure and Raman spectroscopy are the main techniques used in this work. The physical properties of the oxide materials have been investigated by combinations of ultraviolet-visible spectroscopy (UV-Vis.), and electron microscopy.

2.2 Synthetic Techniques

2.2.1 High Temperature Methods

High temperature methods, known as calcination reactions, are one of the most widely method used for the synthesis of inorganic materials. In the preparation of mixed metal oxide materials, for example, the pure single oxides or the nitrate of the metals are used as starting materials [1, 2]. These are usually ground together in a mortar, pressed using a hydraulic press to form a pellet, and finally fired in a range of 500 – 2000 °C for several hours. Both the grinding and pelleting steps are made to ensure a homogeneous distribution of the different starting materials, and to reduce the inter-particle empty space in order to improve the reaction rates. The high temperature used in a solid state reaction will speed up also the process as the rates of diffusion of the various ions increase.

2.2.2 Sol-gel Methods

In the preparation of complex oxides through the calcination method several difficulties need to be taken into account: the control of the size and morphology of the solid particles, the formation of undesirable phases, the final stoichiometry, and a poor chemical homogeneity of the powders [1, 3]. The sol-gel processes, compared to the conventional powder route, allow a better control from the molecular precursor to the final product, offering possibilities in the tailoring of materials which result in high purity, high homogeneity, low temperature preparations, size and morphological control of the particles, and the opportunity for the preparation of new crystalline and non-crystalline solids.

In general the sol-gel procedure, represented in Figure 2.1, consists of the following steps [3]:

- Preparation of a homogeneous solution either by dissolution of metal organic precursors in an organic solvent, or by dissolution of inorganic salts in water or aqueous solution (e.g. HNO_3, and H_2O_2)

- Converting the homogeneous solution to a sol by treatment with a suitable reagent (pure water or water with HCl, NaOH, NH_4OH or acetic acid)

- Ageing: The sol changes into a gel by self-polymerization

- Shaping the gel to the finally desired form (thin films, fibres, spheres…)

- Converting (sintering) the shaped gel to the desired ceramic material generally at temperatures between 500 - 1000°C

The sol-gel processes can be classified into two different routes depending on the nature of the precursors: - the precursor is an aqueous solution of an inorganic salt or - a metal organic compound.

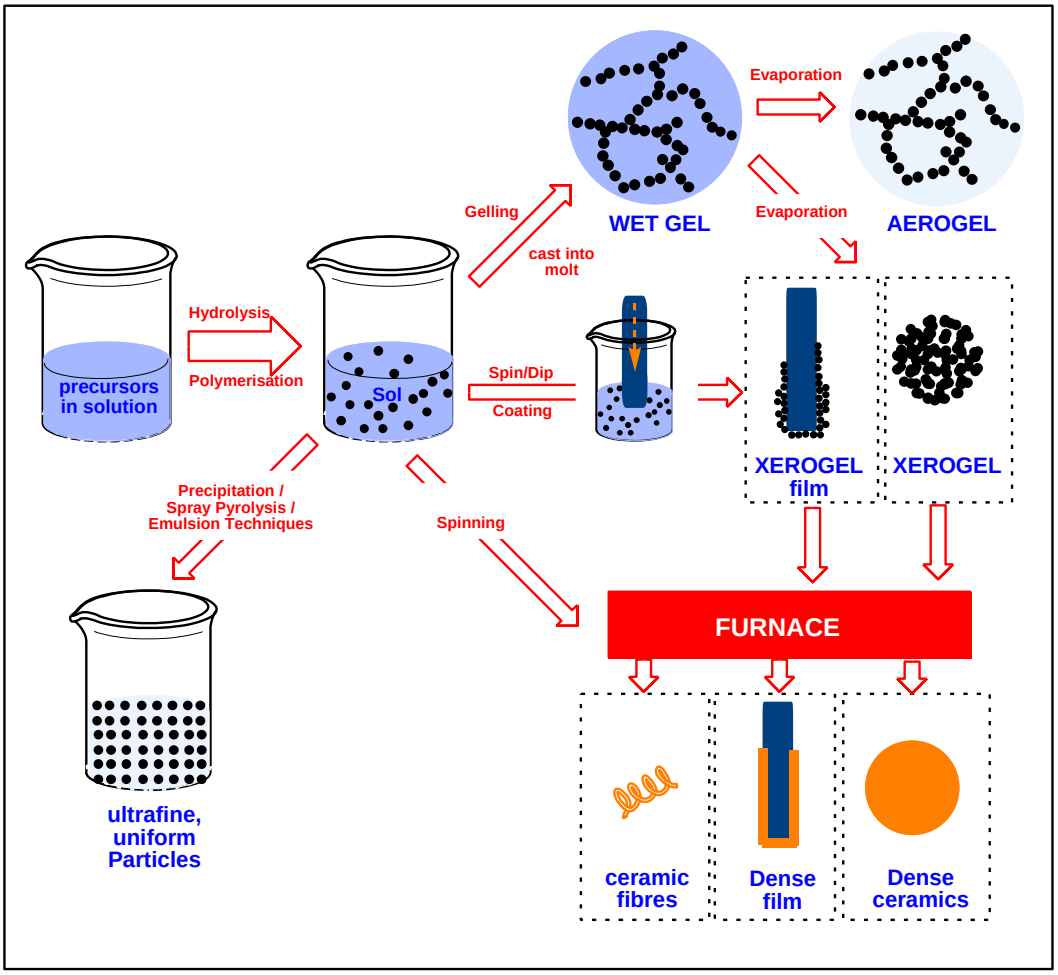

Figure 2.1 – The sol-gel technologies and their products

Vanadium alkoxides are often used to form vanadium gels through hydrolysis reaction followed by condensation [3]. In particular J.S. Paul and co-workers reported the synthesis of homogeneous solutions of vanadium mixed transition metal oxides, in an acid-catalysed sol-gel procedure [4, 5].

A simple and inexpensive inorganic sol-gel route to produce transition metal oxides such as MoO_3, WO_3, TiO_2, and V_2O_5 has been developed by C.J. Fontenot *et al.* [6-8]. Even though the aqueous chemistry of inorganic salts is quite complex, since hydrolysis reactions convert the ions in solution to new species, Livage has reported the most widely accepted mechanism of gelation from an aqueous vanadate solution [3]. In this mechanism the reactive precursor is the neutral $[VO(OH)_3]$ species.

Since the OH groups in the water are more nucleophilic than the OH in the vanadium complex, the $VO(OH)_3$ will expand its coordination through water addition giving a

neutral vanadium six-coordinated species as $[VO(OH)_3(OH_2)_2]$. Condensation will proceed via olation forming a chain-like polymer.

After this step, the solvent can be evaporated obtaining a homogeneous amorphous powder. This peroxo sol-gel method was used as the basis for the synthesis of both the sequential and the array materials in these studies.

2.3 Powder X-ray Diffraction (PXD)

2.3.1 Theory

Since each crystalline solid has its own characteristic x-ray powder diffraction pattern, the PXD method is one of the most used analytical methods in the solid state chemistry.

When an incident beam of x-rays interacts with matter, all the atoms in the path of the beam will scatter simultaneously. In general the scattered waves interfere cancelling each other in a destructive interference phenomenon; the opposite happens in certain specific directions, the x-rays scatter cooperatively to form a new wave in a process of constructive interference called diffraction, Figure 2.2. For a monochromatic radiation, diffraction can be described using the Bragg's Law which allows us to treat the diffraction phenomenon in simple terms [2, 9]:

$$n\lambda = 2d \sin\theta$$

where λ is the x-ray wavelength,
n is an integer (1, 2, 3….),
d is the inter-planar separation in the crystalline material,
θ is the angle of incidence (Bragg angle).

By this equation the angle of the diffraction, usually denoted as 2θ, is related to the inter-planar spacing d, and as consequence at the size and shape of a particular unit cell; whereas the intensities of the diffracted waves, will depend on the type and arrangement of atoms in the crystal structure.

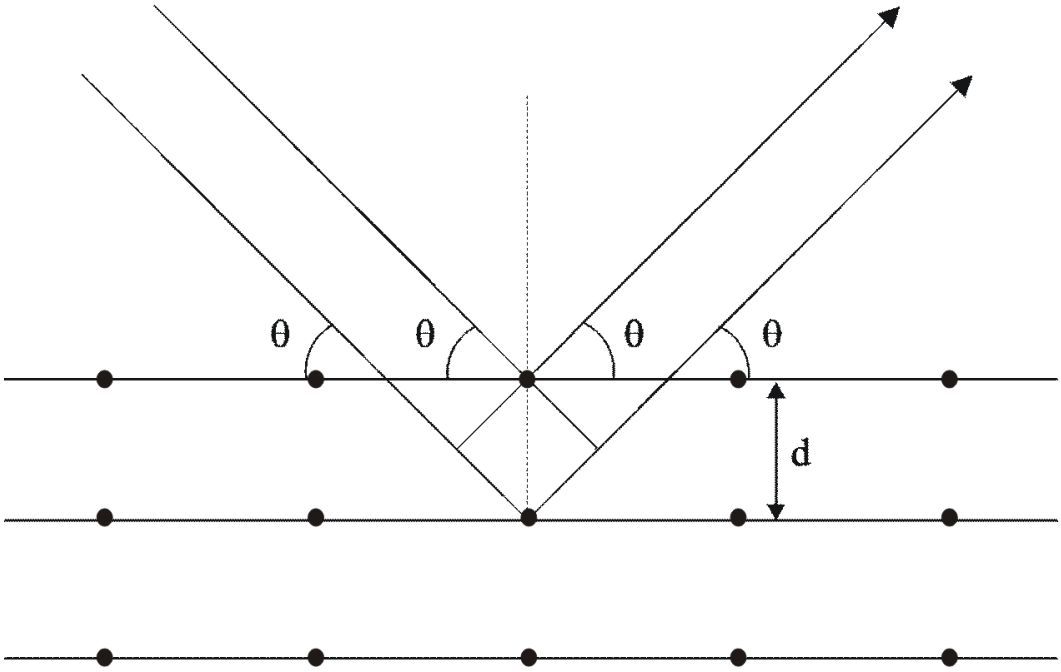

Figure 2.2 – Schematic representation diffraction from individual point scatterers aligned in parallel planes

2.3.2 PXD Instrumentation

The PXD data collection of the sequential both calcinations and sol-gel materials were collected by a Siemens D5000 powder diffractometer. This diffractometer, see Figure 2.3, use the copper $K_{\alpha 1}$ radiation emission as the x-rays source (Cu x-ray tube), λ = 1.5406 Å, with a germanium single crystal monochromator (111 plane). The monochromated beam is then collimated, before the sample, by aperture slits. After that the diffracted beam will pass through a second set of slits before to reach a NaI scintillation detector. The relative position of incident beam, sample, and detector is made according to the Bragg Brentano geometry. In order to keep a fixed relationship between the incident angle θ and the diffraction angle 2θ during the experiments, the sample is rotated a constant angular velocity whereas the detector is rotated a double of this velocity. A computer with specific software for x-ray collection and data storage is connected with the diffractometer.

Phase identification of the data collected was performed using the Diffrac^{plus} evaluation program (E.V.A.) [10].

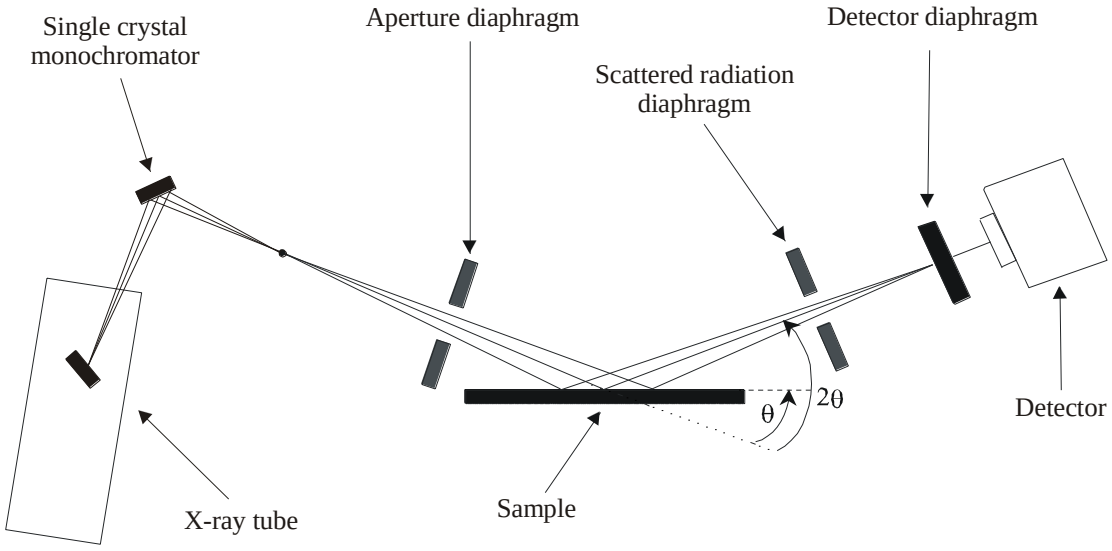

Figure 2.3 – Schematic representation of the D5000 diffractometer

2.3.3 The Rietveld Method

The typical solid state method of synthesis, such as calcination or sol-gel followed a high temperature step, produces powders constituting small crystallites. As consequence the typical single crystal studies approach became inappropriate in their structure determinations. These are often performed using the Rietveld Method [11, 12].

In order to perform a good PXD data refinement by this method, several factors need to be taken into account before data acquisition is performed:

- *Geometry of the diffractometer* (for Bragg-Brentano geometries, the incident beam must be kept on the sample in order to ensure a constant volume condition)
- Instrument *calibration & alignment*, and *wavelength*
- Appropriate *sample preparation* and *thickness* (highly absorbing samples should be diluted with a light-element material)
- *Slit sizes* (smaller slits should be used at lower angles and wider ones at higher angles)
- *Counting time* (more time should be spent on data collection at high angles where intensities are lower)

Several computer packages have been developed in the last twenty years for the powder data refinements; in this thesis the refinements were carried out using the *General Structure Analysis Suite* (GSAS) [13].

The experimental powder diffraction pattern obtained from a crystalline material can be considered as a selection of several individual reflection profiles, each of them with a peak height, peak position, peak width, peak shape and an integrated area which is proportional to the Bragg intensity, I_k, where k represents the Miller indices *h*, *k*, and *l*. This I_k intensity is proportional to the square of the absolute value of the structure factor, $|F_k|^2$.

In the Rietveld method, the profile refinement of a generic powder pattern is performed by the total integrated intensities of the different groups of overlapping peaks. Furthermore, use of this method does not require previous either assignment of an observed intensity to a specific Bragg reflection or resolution of overlapping reflections.

The Rietveld method can be defined as a process which compares a theoretical model with an experimental diffraction pattern. In this refinement process several structural and positional parameters (such as lattice parameters, atomic coordinates, and site occupancies), together with profile parameters (such as temperature factors, peak shape, and asymmetry), and instrumental factors (such as zero point) are varied. In order to obtain the best fit between the experimental pattern and the theoretical model, a least squares refinement is performed simultaneously on both the structural and profile parameters.

2.3.4 Data Refinement

There is many parameters that can be varied while performing a powder data refinement using the Rietveld method, even though their fully refinement is not possible or recommended. The typical procedure for the refinement of a structural model for x-ray powder diffraction data require:

- Determination of an *approximate model* of the structure (e.g. using the ICSD database [14])

- Refinement of the *lattice parameters* and *zero point error* (to accurately locate the Bragg reflections)

- Refinement of the overall *scale factor* and *background parameters*

- Refinement of the *atom positions* in the structure (varying first the position of the heaviest atoms and then try those of the lighter atoms)

- Refinement of the *isotropic temperature factors* (constraining the thermal factors for similar atoms to be equal and starting from the heaviest atoms)

- Full refinement of *peak shape parameters*, in addition to any asymmetry or preferred orientation parameters which might be necessary

The structure should be refined to convergence, and all parameters (profile and structural) should be refined simultaneously to obtain correct estimated standard deviations.
In the Rietveld method the function *M* is minimised, that is the difference between the observed data, y_i^{obs}, and the calculated, y_i^{calc}, using a least squares method:

$$M = \sum_i w_i (y_i^{obs} - y_i^{calc})^2$$

where w_i is a weighting factor given by $1/y_i^{obs}$.
The calculated profile derived, y_i^{calc}, is determined from the structural model adding together the calculated contributions from neighbouring Bragg reflections (k) and the background b_i:

$$y_i^{calc} = s\sum_k L_k |F_k|^2 \phi(2\theta_i - 2\theta_k) P_k A + y_{bi}$$

where s is the scale factor which ensures that magnitudes are the same for all the intensities, L_k contains the Lorentz, polarization and multiplicity factors, F_k is the structure factor for the k^{th} Bragg reflection, ϕ is the peak shape function, P_k is the preferred orientation function, A is an absorption factor, and y_{bi} is the background intensity at the i^{th} step.

A comparison of the intensities is performed at every point, consequently it is essential to accurately describe the *peak shape*, for the construction of the calculated profile.
The Siemens D5000 diffractometer employs the pseudo-Voigt peak shape function, which is made by Lorentzian, and Gaussian contributions.

In order to make a quantitative assessment of the agreement between the observed and calculated profile a number of reliability indices are given:

$$R_{profile} = R_p = 100\left[\frac{\sum_i \left|y_i^{obs} - y_i^{calc}\right|}{\sum_i y_i^{obs}}\right]$$

From a mathematical point, $R_{weighted\ profile}$ (R_{wp}) is the most significant of the R-factors. This is so because the residual that is being minimised is the numerator. For identical reasoning it is the factor which best reflects the progress of a refinement and is given by:

$$R_{wp} = 100\left[\frac{\sum_i w_i \left(y_i^{obs} - y_i^{calc}\right)^2}{\sum_i w_i \left(y_i^{obs}\right)^2}\right]^{\frac{1}{2}}$$

Another criterion that measures the *goodness of fit* is the chi-squared test (χ^2). This criterion ideally should tend to one meaning perfect correlation between the model and the data has been achieved. This is defined as:

$$\chi^2 = \left(\frac{R_{wp}}{R_{exp}}\right)^2$$

For a good fit, the R_{wp} should approach the statistically expected R-factor, R_{exp}. As a visual key, the goodness of fit can be observed by examining a plot of the profile fit. The difference line between calculated and observed patterns should be as flat as possible for a good fit.

2.4 X-Ray Absorption Fine Structure (XAFS)

2.4.1 Theory

XAFS spectroscopy is a spectroscopic technique that, providing information on the chemical state and local atomic structure, is used in a wide range of scientific fields such as environmental science, catalysis, and material science. Furthermore, XAFS spectra are particularly sensitive to the oxidation state, distances, coordination number, and atomic species immediately surrounding a particular element [15].

In particular since the problematic refinement of light atoms positions in mixed metal oxides materials by the XPD technique, XAFS spectroscopy reveals to be a strategic complementary tool in the study of inorganic oxide pigments.

According to the Lambert-Beer Law, when a beam of x-ray photons passes through a material, the incident intensity I will decrease by an amount that is determined by the characteristic absorption of the material irradiated. For a given path length the Lambert-Beer Law is:

$$I = I_0 \, e^{-\mu(E)t}$$

where I_0 is the x-ray intensity incident on the sample, t is the sample thickness, I is the intensity transmitted through the sample, and μ is the absorption coefficient (function of the photon energy) which gives the probability for a x-ray to be absorbed.

When the energy of the incident photon is equal to that of the binding energy of a *core level electron*, this will be promoted to the continuum, Figure 2.4, and a strong increment in the absorption intensity will appear. This is known as the absorption edge, Figure 2.5.

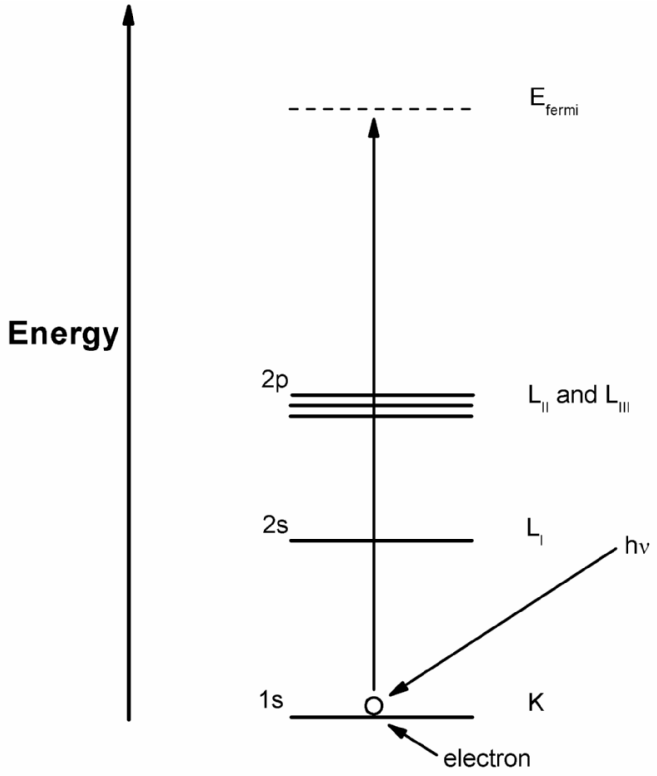

Figure 2.4 – Schematic representation of the photoelectric effect in terms of excitation of the different energy levels

Since every atom has a core level electron with well defined binding energy, the XAFS spectroscopy is element specific. The kinetic energy of the electron for any energy above the absorption edge, E_k, is given by:

$$E_k = h\nu - E_{binding}$$

From a quantum mechanical point of view the outgoing photoelectron can be described as a spherical wave with wavelength λ defined as:

$$\lambda = 2\pi/k$$

where k, the wave-vector, is a function of the electron mass, the photon energy $h\nu$, kinetic energy of the electron at the absorption edge, and the energy edge E_{edge}.

The XAFS spectrum of a generic atom can be divided in two different regions, which contain related but slightly different information about an element's local coordination and chemical state, Figure 2.5. The x-ray Absorption Near-Edge Structure (XANES) is the region of the spectrum within ~ 50 eV of the absorption edge.

Data analysis of this area of the spectrum gives information about formal valence, and coordination environment, since the edge position and shape is sensitive to formal valence state, ligand type, and coordination environment; whereas, the Extended x-ray Absorption Fine-Structure (EXAFS) is the region of the spectrum at ~ 25 eV above the absorption edge. EXAFS data analysis gives information about the type and the number of neighbours, their distance from the central atom, and the disorder in distances.

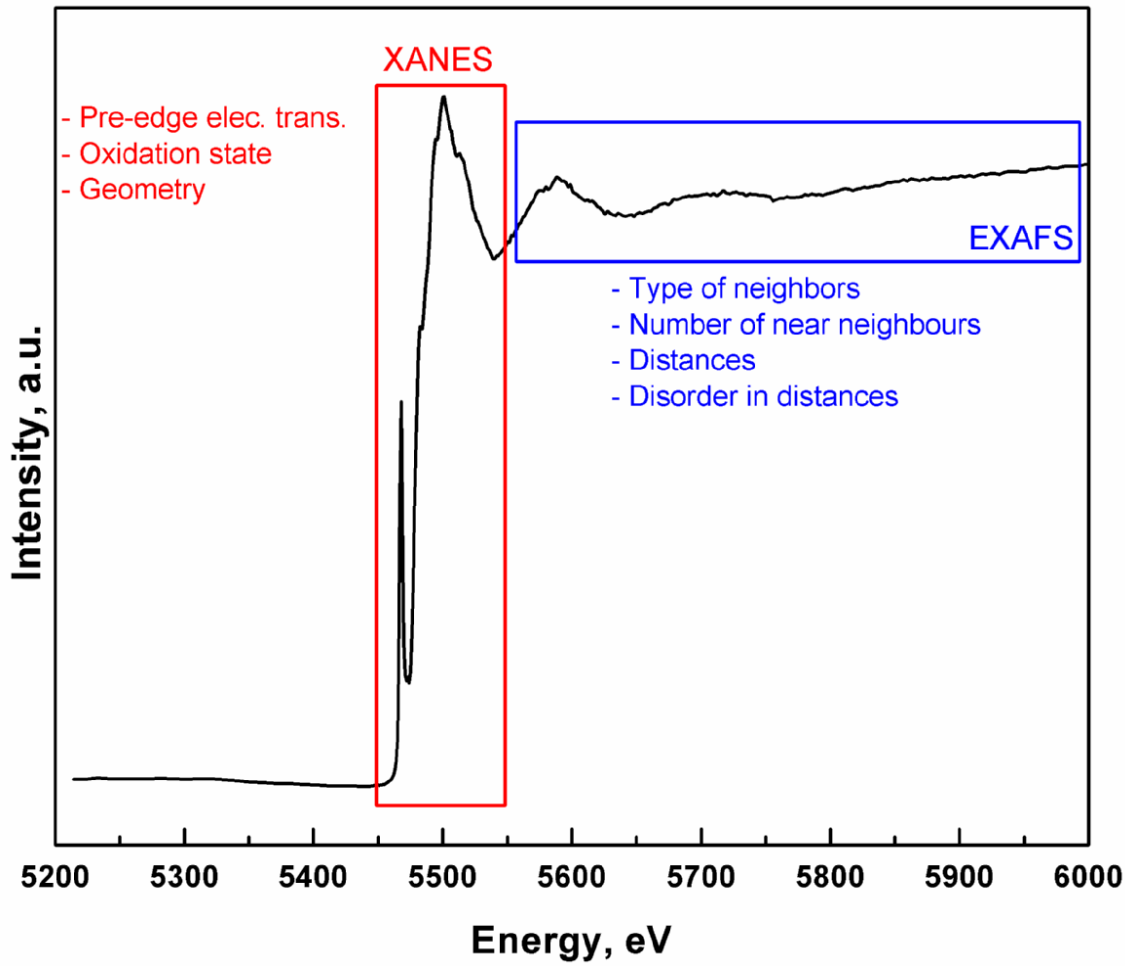

Figure 2.5 – XAFS V K edge of monoclinic $BiVO_4$, showing the pre-edge and XANES region, and the EXAFS region

2.4.2 Data acquisition

In order to obtain valuable structural information from both XANES and EXAFS data analysis, XAFS requires a very good measure of $\mu(E)$. The main experimental challenges are getting an x-ray source that can be tuned in energy, and high-quality detectors of x-ray intensities. Synchrotrons are the typical x-ray sources used, which provide a full range of x-ray wavelengths, and single crystal silicon monochromators that use the Bragg diffraction to select a particular energy [16].

Energy resolution, one the most important characteristics of a monochromator together with the reproducibility and stability, of about 1 eV at 10 keV are achieved with silicon monochromators.

XAFS data collection can be performed in either in transmission or fluorescence modes. During an XAFS experiment the energy dependence of the absorption coefficient $\mu(E)$ is measured:

$$\mu(E) = \log(I_0/I) \quad \text{(Transmission mode)}$$

or

$$\mu(E) \approx I_f / I_0 \quad \text{(Fluorescence mode)}$$

where I_f is the monitored intensity of a fluorescence line related with the absorption process. XAFS spectroscopy studies presented in this work were carried out at the Science and Technology Facility Council's (STFC) Synchrotron Radiation Source (SRS) at the Daresbury Laboratory (Daresbury, U.K.), at the European Synchrotron Radiation Facility (ESRF) (in Grenoble, France), and at the Hamburger Synchrotronstrahlungslabor (HASYLAB) at Deutsches Elektronen-Synchrotron (DESY).

2.4.3 Data Analysis of the EXAFS Spectra

For both transmission and fluorescence modes the data reduction and analysis of $\mu(E)$ is essentially the same.
Data reductions of both the sequential and the array materials have been performed using the software *X-MULT* [17], a high-throughput version of the *PAXAS* program [18].

Steps of data reduction are:

- Convert measured intensities to $\mu(E)$
- Subtract a smooth pre-edge function from $\mu(E)$ to eliminate any instrumental background and absorption from other edges
- Identify the threshold energy $E_{binding}$
- Remove a smooth post-edge background function to approximate the absorption of an isolated atom
- Isolated the XAFS

In order to improve the signal ratio several spectra, no less than three, were collected for each experiment, and then averaged.
The model fitting program *EXCURVE* (9.301) [19] have been used for the sequential (one-by-one) materials. It uses curved wave theory and computationally fast algorithms to theoretically model the oscillations in the EXAFS and to determine structural information. Several structural dependent parameters such as the coordination number, the type of atom in a shell, the Debye-Waller factor for the shell, the E_f Fermi Energy, the range of energy to calculate the theoretical spectrum (E_{min} – E_{max}), and the energy amplitude factor afac were refined starting from theoretical structural models obtained from previous PXD data refinement of the different materials.
The quality of the fit between the experimental and theoretical spectra is given by the R-factor, defined as:

$$R_{EXAFS} = \sum_n 1/\sigma_i(|\chi_i^{exp}(K) - \chi_i^{th}(K)|) \times 100\%$$

and gives a significant indication of the quality of fit to the EXAFS data in k-space. A value of around 20% would normally be considered a reasonable fit.

2.5 Raman Spectroscopy

2.5.1 Theory

Raman spectroscopy is the most effective tool for probing the structure of metal-oxygen groups in crystalline, melts, and glasses materials. Raman is a light scattering technique, and can be thought of in its simplest form as a process where a photon of light interacts with a sample to produce scattered radiation of different wavelengths. Raman spectroscopy is extremely information rich, being able to provide useful information for chemical identification, characterization of molecular structures, effects of bonding, environment and stress on a sample.

When light is scattered from a material, most of the photons are elastically scattered and, therefore, they have the same frequency of the incident photons[20]. However, a small fraction of them is scattered at lower optical frequencies than the incident photons. This inelastic scattering is called the Raman effect, and it can occur with a change in the vibrational, rotational, and electronic energy of molecules within the material. The difference in energy between the scattered and incident photon will be equal to the energy of a vibration of the scattering molecule (Rotational transitions can also be probed for gas phase molecules) [21]. In Raman spectra the intensity of scattered light versus energy difference is plotted.

The Raman Effect arises when an incident photon interacts with the electric dipole of a molecule. This interaction can be seen in classic term as a perturbation of molecule's electric field; whereas the scattering can be described, in quantum mechanics terms, as an excitation to a virtual state (with lower energy than a real electronic transition) with almost coincident de-excitation energy, Figure 2.6.
The energy difference between the initial and final vibrational levels, called Raman shift (cm^{-1}), is given by:

$$Raman\ Shift = (1/\lambda_{incident}) - (1/\lambda_{scattered})$$

where $\lambda_{incident}$ and $\lambda_{scattered}$ are the wavelengths (cm) of the incident and Raman scattered photons, respectively.

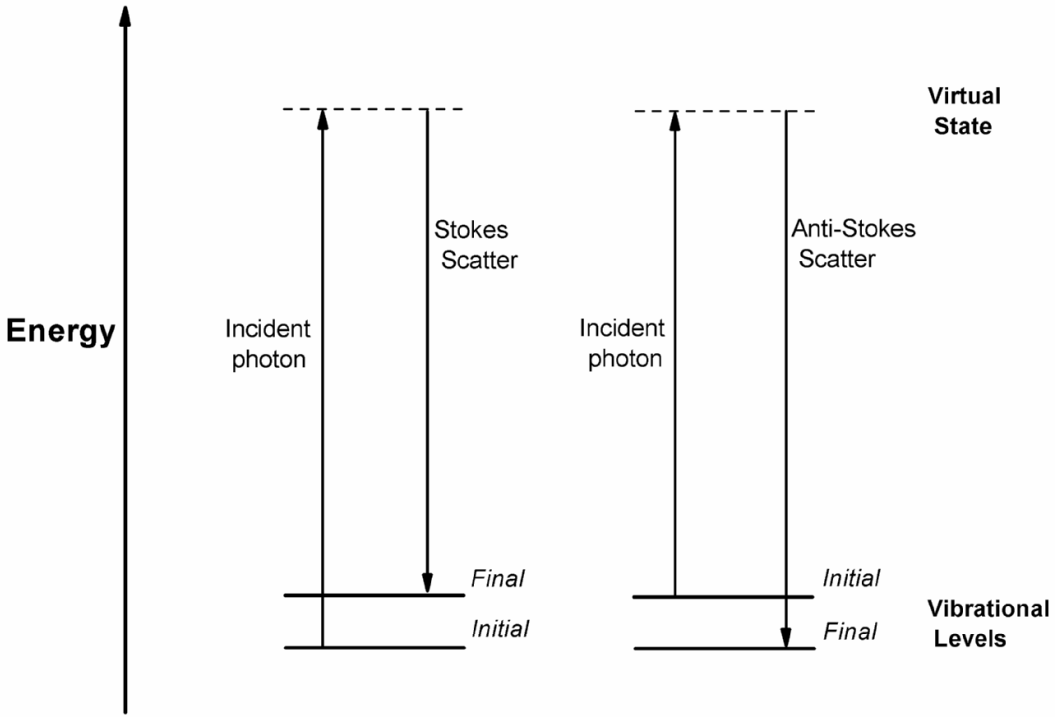

Figure 2.6 – Energy level diagram for Raman scattering, (left) Stokes Raman scattering (right) anti-Stokes scattering

2.5.2 Data Analysis of Raman Spectra

Raman spectra of both bulk and array samples were collected with an optical fibre Renishaw RA100U Spectrometer, using high-power NIR laser (785 nm) with a resolution of 3 cm^{-1} in the range between 100 and 1000 cm^{-1}. Spectra were calibrated using the 520.5 cm^{-1} line of a silicon wafer. Raman data analysis were performed using the *WIRE 2.0* software developed by the Renishaw Company [22].

2.6 Solid state UV-Visible Spectroscopy

Ultraviolet-Visible (UV-Visible) spectroscopy data of sequential materials were collected using a Perkin Elmer UV-Vis. Lambda 35 spectrometer in diffuse reflectance mode. Spectra were recorded in the visible region in the range of 380-780 nm.

In order to perform data collection in the whole UV-Vis region, the instrument contains two different radiation sources. A halogen lamp is used to cover the visible region, whereas a deuterium lamp is used to cover the ultraviolet region;

these two lamps are alternatively blocked. A holographic concave grating with 1053 lines/mm acts as a monochromator. During data collection a series of mirrors within the instrument allow the radiation to be aligned. After interaction with the sample the radiation passes through a convex lens onto a photodiode detector, Figure 2.7.

Samples were mounted in an aluminium holder with quartz window. A barium sulphate block was used as reference to obtain a background correction before collecting data.

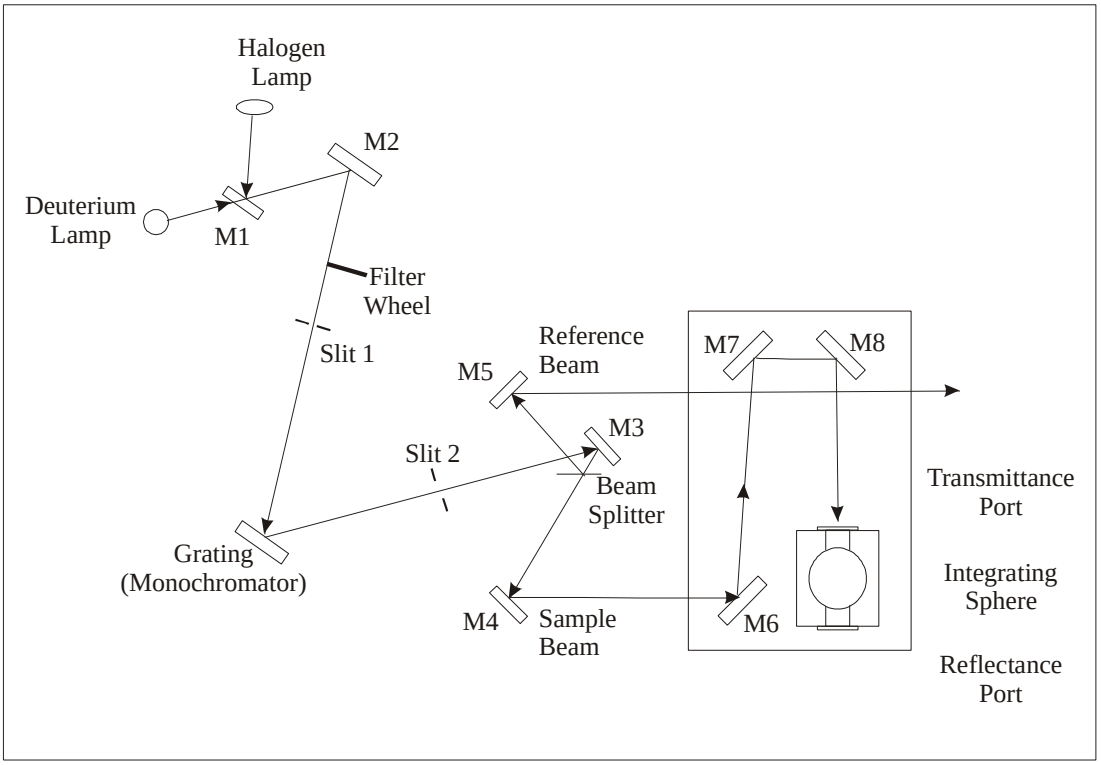

Figure 2.7 – Schematic representation of the Lambda 35 Spectrometer

2.7 Electron Microscopy

The use of Scanning and Transmission Electron Microscopy, SEM and TEM respectively, in the study of mixed metal oxides can be used to provide information regarding the shape and size of the particles including the particle size distribution [23].

Scanning electron microscopy was performed using a Jeol 5910 Scanning Electron microscope, Figure 2.8. The microscope consists of an electron gun that generates an electron beam via thermionic emission from a heated tungsten filament.

The tungsten filament acts as a cathode and is heated to *ca*. 2800 K by the passage of a current while held at a high negative potential with respect to the anode and the rest of the microscope. The electrons are accelerated to energy typically in the region of 1-30 keV. The beam of electrons travels through an evacuated optical path (*approx*. pressure < 10^{-10} Pa) as electrons are strongly scattered by gases.

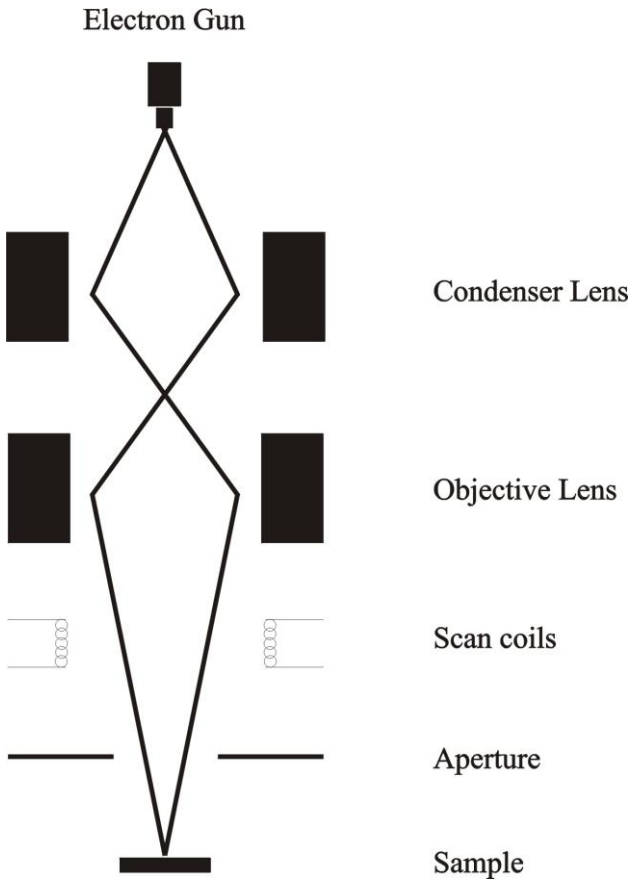

Figure 2.8 – Schematic representation of the Scanning Electron Microscope, where the solid line represents the path iof the electron beam

The electron beam travels down the SEM and before hitting the sample is demagnified by two electromagnetic condenser lenses. This controls the convergence angle and diameter of the beam (2-10 nm). Below the condenser lenses lie four or five electromagnetic objective lenses. These lenses form the first intermediate image and diffraction pattern, which can be enlarged by the subsequent projector lenses and then displayed on screen. These projection lenses determine the overall magnification of the final image. Scan coils are used to scan the beam across the sample and a photomultiplier system is employed as a detector to count

the number of low energy secondary electrons or other radiation emitted from each region of the sample.

Transmission electron microscopy was performed using a Jeol 3010 Transmission Electron microscope. A typical TEM system is a microscope column type arrangement where the illumination is provided by an electron gun at the top which is focussed onto the specimen by a series of electromagnetic lenses. The specimen has to be a very thin sample, with a thickness less than 2000 Å. The image of the sample can be viewed physically by looking at a viewing screen, usually a simple layer of X-ray fluorescent material, through a lead glass window. The microscope is also fitted with a camera which must work in the vacuum within the microscope, typically 1×10^{-5} mbar.

Bombardment of a specimen with high energy electrons results in a characteristic emission of X-rays. The wavelengths of the X-rays are dependent upon the atoms that are present in the sample. Each element has characteristic X-ray lines relating to the excitation of a core electron to a higher energy level. Analysis of these characteristic emission lines allows for the relative proportion of each constituent to be determined. The detector normally consists of a small semi-conductor such as Si, held in a position so that the X-ray emission from the sample falls upon it. In the case of a TEM system, the detector is normally placed within the objective lens. The detector works by exciting electrons into the conduction band of the silicon, leaving an identical number of positively charged holes in the outer-electron shells. The number of electron-hole pairs generated is proportional to the energy of the X-ray photon being detected.

2.8 References

1. M.T. Weller, *Inorganic Materials Chemistry*. Oxford Chemistry primers, ed. O.S. Publications. **1994**, Oxford, Oxford University.
2. A.R. West, ed. *Solid State chemistry and its Applicaiton*. 1987, Wiley. 449-450.
3. J. Livage, M. Henry, and C. Sanchez, Progr. Sol. St. Chem., **1988**, 18, 259-341.
4. J.S. Paul, J. Urschey, P.A. Jacobs, W.F. Maier, and F. Verpoort, J. Catal., **2003**, 220, 136-145.
5. J.S. Paul, P.A. Jacobs, P.A.W. Weiss, and W.F. Maier, Appl. Catal. A-Gen., **2004**, 265, 185-193.
6. C.J. Fontenot, J.W. Wiench, M. Pruski, and G.L. Schrader, J. Phys. Chem. B, **2000**, 104, 11622-11631.
7. W.D. Schroeder, C.J. Fontenot, and G.L. Schrader, J. Catal., **2001**, 203, 382-392.
8. C.J. Fontenot, J.W. Wiench, G.L. Schrader, and M. Pruski, J. Am. Chem. Soc., **2002**, 124, 8435-8444.
9. M.F. Perutz, Acta Crystallogr. Sect. A, **1990**, 46, 633-643.
10. B.A. GMBH, *E.V.A.*, Bruker Advanced X-Ray Solutions, Karlsruhe, **2004**.
11. L.B. McCusker, R.B. Von Dreele, D.E. Cox, D. Louer, and P. Scardi, J. Appl. Crystallogr., **1999**, 32, 36-50.
12. H.M. Rietveld, J. Appl. Crystallogr., **1969**, 2, 65-71.
13. A.C. Larson and R.B. Von Dreele, *Generalised Structure Analysis System*, Los Alamos National Laboratory, Los Alamos, **2004**.
14. *Inorganic Crystal Structure Database, ICSD*, Karlsruhe.
15. D.C. Koningsberger, B.L. Mojet, G.E. van Dorssen, and D.E. Ramaker, Top. Catal., **2000**, 10, 143-155.
16. M. Newville, *Fundamentals of XAFS*. 2004, Consortium for Advanced Radiation Sources: Chicago. p. 1-41.
17. N. Binsted, *X-Mult*. University of Southampton, Southampton, **2006**.
18. N. Binsted, *PAXAS, Program for the Analysis of X-ray Absorption Spectra*, University of Southampton, **1992**.
19. N. Binsted, *EXCURV(9.301)*. CCLRC Daresbury Laboratory Computer program, **1998**.
20. K. Nakamoto, *Infrared and Raman Spectra of inorganic and Coordination Compounds*. Vol. A. **1997**, New York, Wiley Interscience. 387.

21. P. Atkins and J. De Paula, *Atkins` Physical Chemistry*. Seventh ed. **2002**, Oxford, Oxford University Press.
22. Renishaw, *WIRE 2.0*, Wotton-under-Edge, **2006**.
23. P.J. Goodhew, J. Humphreys, and R. Beanland, *Electron Microscopy and Analysis*. 3rd ed. **2001**, London, Taylor & Francis.

CHAPTER THREE

HIGH-THROUGHPUT TECHNIQUES

Chapter Three: High-Throughput Techniques

3.1 Introduction

Combinatorial and high throughput processing methods (HTP) are widely recognised as an important and rapidly expanding area of research. The ability to quickly perform both the synthesis and structural characterization of large numbers of materials, using relative small amount of starting reagents, makes these techniques attractive for the industrial research [1-5].

HTP XAFS and Raman spectroscopy are virtually unexplored techniques compared to the HTP X-ray diffraction methods, which are now well-established for HTP characterization of crystalline bulk phases [5, 6]. An environmental chamber for HTP studies has been developed in this study, allowing combined XRD/XAFS, and Raman analysis which can be performed *in situ* and with time-resolution [7]. New software for sequential and HTP combined XRD/EXAFS data analysis had been developed [8].

This chapter describes the development of high-throughput methods for the synthesis and characterization of arrays of metal mixed oxide pigments.

3.2 HTP Array Synthesis

In order to carry out numerous reactions in parallel a HTP re-usable *masking system* to contain the liquid reagents, previously developed in this research group, have been used [9]. The system comprises a Teflon mask, with a 6x9 grid of 5mm holes, pressed on to an alumina tile by stainless steel plates, Figure 3.1. Below a layer of rubber allows even pressure across the tile and a PTFE sheet to prevent the tile sticking to the rubber during heating. Firing of the alumina tile is carried out in a large tube furnace (internal diameter 75mm) with a maximum temperature of 1200°C. Starting solutions have been dispensed across the mask system by a *Liquid Handling System* (Packard Multiprobe II Robot), Figure 3.2, controlled by a computer through the WinPREP software.

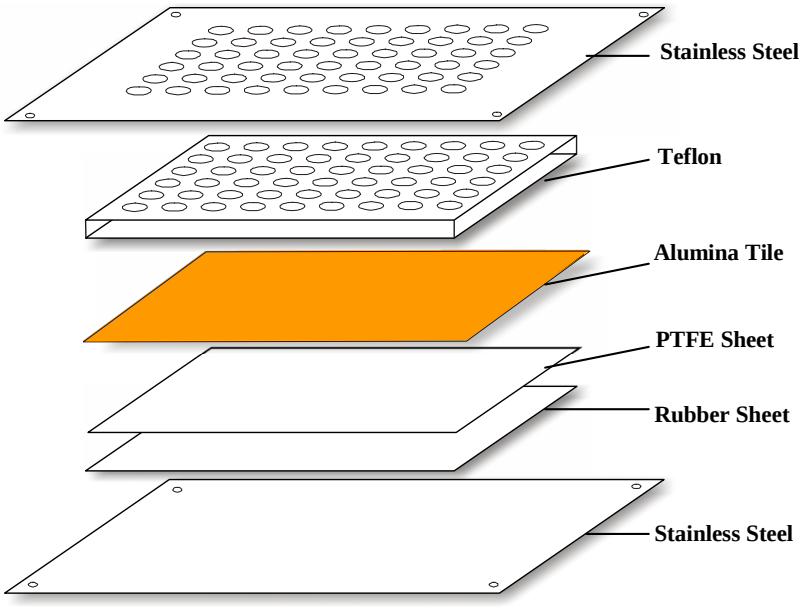

Figure 3.1 - Components of the masking system based around an alumina substrate

Figure 3.2 – HTP Liquid Handling System; (Red) Grid for locating well plates, (Blue) Dispensing pipettes

In a typical HTP array synthesis a peroxo sol-gel method was used. Stock solutions of the reagents, prepared by dissolving metal nitrates and ammoniates (about 0.5 M) in diluted nitric acid and hydrogen peroxide water solution (1:1), were dispensed in the appropriate ratios across the array. After that, the solvent was evaporated at 60 °C overnight in an oven in air atmosphere before the alumina tile was fired up to 700 °C in a furnace in oxygen atmosphere for 24 hours.

During the development of the synthesis methods different issues has been considered. Because the pressure provided by the steel plates was not sufficient to form a tight seal between the Teflon and the alumina tile, apiezon grease which reproducibility provided a good seal and could be completely burnt off during the firing processes was used.

The second issue came up form the evaporation of solvent during the ageing step in the oven. The surface tension of the liquid causes a meniscus to form, which results in material being deposited at the edge of the well as the solvent is removed. In previous studies within this group, several methods have been tested to eliminate this “ring effect”, Figure 3.3. The ageing and drying conditions were investigated, varying the ageing time (from 4 to 48 hours) and temperature (from 25 to 100°C), and drying the samples in a desiccator. Nevertheless, rings of material were still deposited.

Additives may be introduced to reduce surface tension and hence discourage formation of a meniscus at the liquid surface. Surface tension results from an imbalance in intermolecular forces at the surfaces of the liquid. Surfactants tend to segregate to the air-water interface, reducing this imbalance and therefore the surface tension [10]. In this study surfactants, either containing metal cations (such as sodium lauryl sulphate) or the non –ionic surfactants (such as Brij 58 and 76), were not used since they proved unsuccessful in reducing ring formation [10].

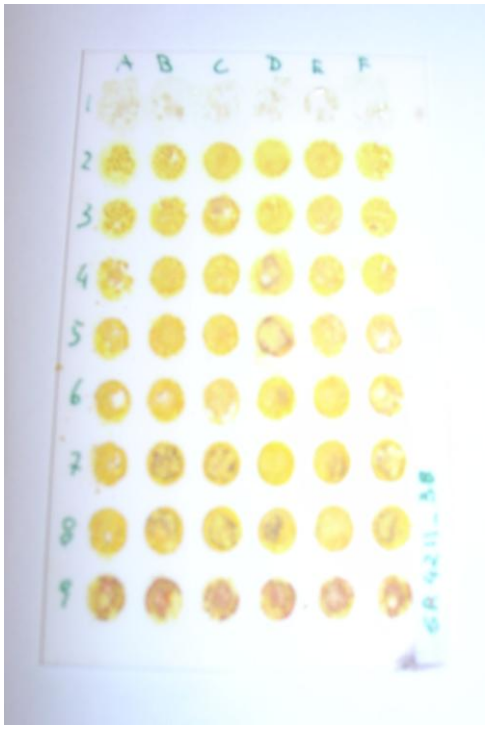

Figure 3.3 – BiMoVOX array, fired at 700°C in oxygen atmosphere, displaying the ring effect

By using a mask with different sized holes (from 1 to 4 mm) above each samples, together with simply remove the Teflon mask while a small amount of solvent remained, revealed to be the most effective way to produce uniform samples, Figure 3.4.

Figure 3.4 – BiFeVOX array, fired at 700°C in oxygen atmosphere, displaying uniform samples

3.3 HTP Environmental Chamber set-up

The experimental chamber developed to perform combined XRD/XAFS, and Raman analysis is shown in Figure 3.5. The chamber, constructed with complete mirror image, allows x-rays from both sides and at the same time allows all other techniques from different sides to make the chamber suitable for a wide range of beamlines and synchrotrons. All flanges bearing the characterisation techniques are positioned such that they all direct to the same focal point, thus allowing simultaneous experiments on small samples and/or the same spot on a sample. XAFS can be performed in either transmission or fluorescence detection mode. The XAFS (Be) transmission windows are of a long rectangular shape to allow simultaneous XRD.

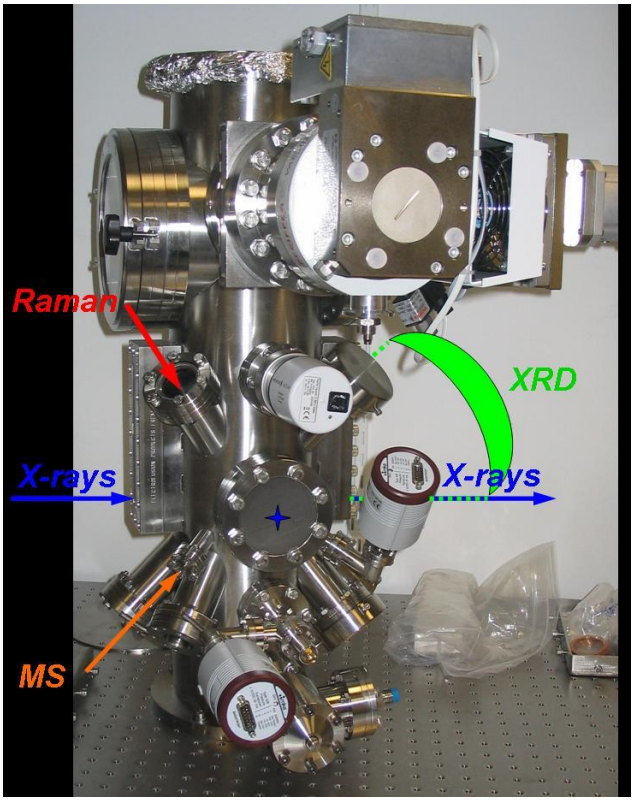

Figure 3.5 – High-throughput Experimental Chamber

A Raman probe is introduced via a re-entrance flange with sapphire window to achieve the proper working distance. The Raman probe is mounted on a tripod, an (x, y, z) -positioning system, to allow accurate focusing of the laser onto the sample. The sample array is mounted onto the manipulator, ensuring a high positional and orientational accuracy. In Figure 3.6 is shown the experimental chamber set-up for combined XAFS/XRD and Raman analysis used at the beam line BM26A at the ESRF, Grenoble.

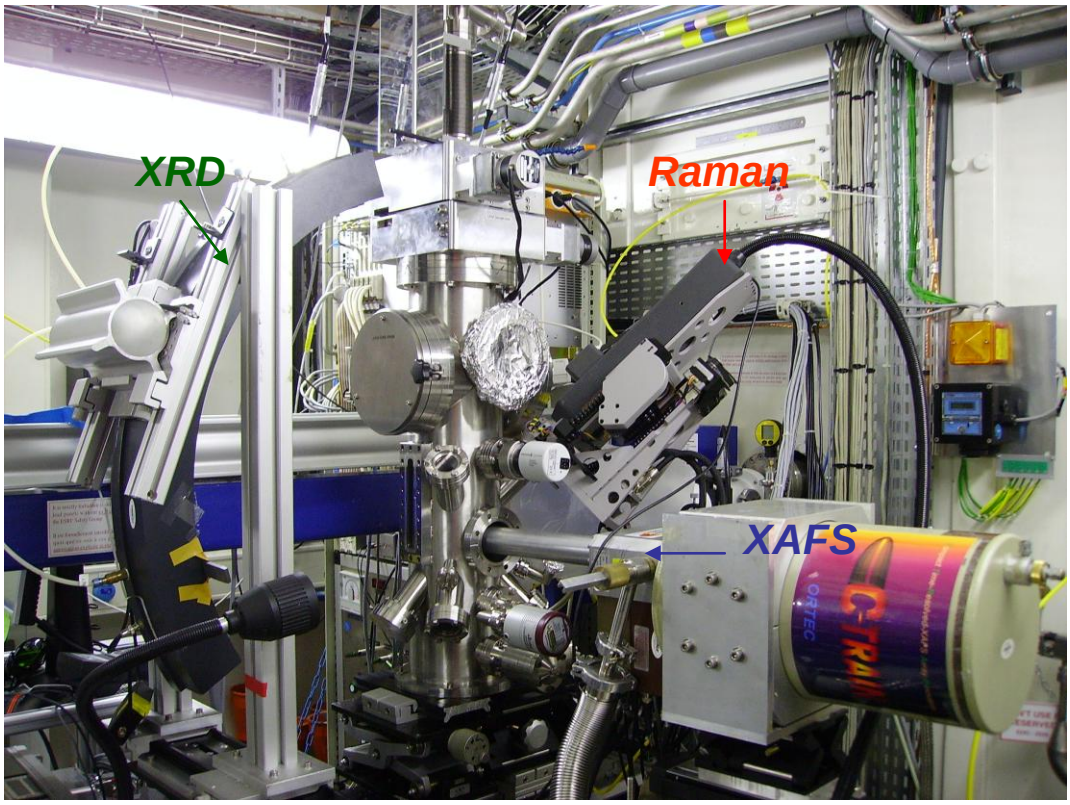

Figure 3.6 – Experimental Chamber set-up at the BM26 station (ESRF, Grenoble)

In Figure 3.7 a scheme for a typical combined XRD/XAFS and Raman experiment, performed at the Daresbury Laboratories SRS (Synchrotron Radiation Source) on Station 9.3, is shown. Station 9.3 is based on a similar principle with x-ray photons passing through a double crystal monochromator producing a tuneable monochromatic beam of the desired energy. For each samples across the array the XRD data were collected first, and then the XAFS data analysis before to move to the next sample. Then, once all the XRD and XAFS analysis were completed, Raman data analysis was performed through the whole array.

The XRD data were collected in transmission mode, using the HOTWAXS detector a position sensitive detector [11]. The XRD patterns were acquired, in the BiMoVOX materials case, at 13300 eV corresponding to a λ= 0.9347 Å. After that, the XAFS analysis of the Mo K edge was performed. Samples were diluted up to 1 wt% metal in SiO_2. Conversion of the position scale to d or 2θ space was performed using reference materials (SiO_2, $BiVO_4$) and an exponential formula in which a, b and c were refined:

$$X(i) = a + b \cdot [x(i) - x(0)] + c \cdot [x(i) - x(0)] \cdot \exp 2$$

with X(i) being the new position (d or 2θ and x(i) the corresponding pixel and x(0) the pixel at d or 2θ = 0. The parameters a, b and c were refined as a = 10, b = 0.175 and c = 0.000096. The HOTWAX detector is shown to give a resolution of 0.20° in the 2θ scale, compared to a resolution of 0.02° with Siemens D5000 diffractometer. The absorbance for the XAFS experiment was calculated using one inert gas filled ion chambers, I_o before the sample and a 9 element Ge solid state fluorescence detector, I_f. The relative absorbance was calculated from the ratio between the two readings (I_f/I_o).

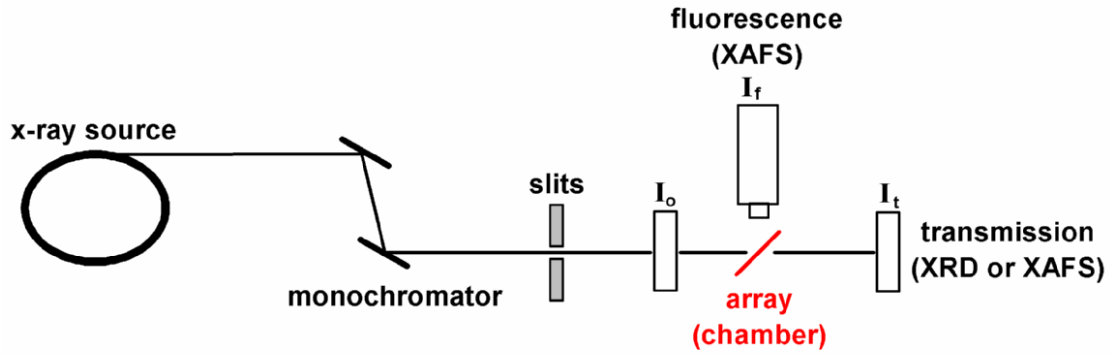

Figure 3.7 – Simple experimental scheme for combined XAFS (Fluorescence), and XRD (Transmission) analysis in Daresbury Laboratory's SRS

XRD data analysis of the BiMoVOX array materials has been also performed using a Bruker D8 Discover with General Area Detector Diffraction System (GADDS) for Combinatorial Screening, also known as the C2 [12]. The instrument uses Cu K_α radiation (λ = 1.5418 Å) with other emission wavelengths being excluded by use of cross-coupled Göbel mirrors.

These are parabolic shaped multilayer mirrors which reflect X-rays in the same way as Bragg diffraction from crystals, allowing a highly parallel beam, with high intensity, to be produced. This intensity is useful for high throughput experiments as it allows rapid scans using a small spot size. The low divergence of the beam incident on the sample also decreases the width of crystalline peaks which improves resolution.

The C2 is also fitted with an XYZ stage and laser video sample alignment system allowing multiple samples to be accurately positioned in the beam. Hence arrays of crystalline samples can be analysed sequentially according to pre-set target lists. The HI-STAR area detector facilitates rapid collection of data which for most applications is 100 times faster than a linear PSD (one-dimensional position-sensitive

detector). These factors make the C2 highly suited for high throughput X-ray diffraction. Figure 3.8 illustrates the configuration of the diffractometer [13].

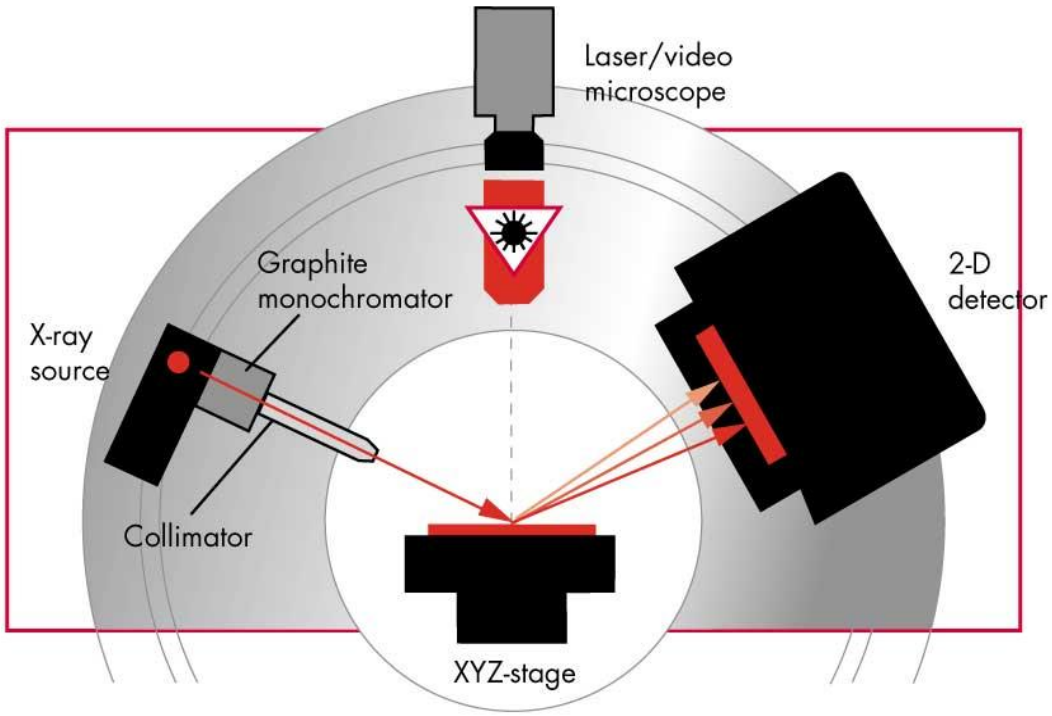

Figure 3.8 - Configuration of the C2 instrument (Graphite monochromator is replaced by Göbel mirrors)

Integration of the diffraction data yields intensity versus 2θ plot analogous to a standard diffraction plot. For phase identification the pattern can be matched against known compounds from the Joint Committee on Powder Diffraction Standards (JCPDS), Powder Diffraction File (PDF) database [14].

3.4 Combined XRD/EXAFS data refinement

EXAFS and XRD techniques, due to their complementarity, have been often combined in the study of materials [15]. EXAFS in provides information in a short-range order, whereas long-range order information is provided by the XRD. Furthermore, since EXAFS is an element specific technique, this allows the determination of coordination number, and bondlengths of elements which occupy the same sites within the crystal structure. Consequently, combined XRD/EXAFS data analysis provides a useful tool able to join the power of the two different

techniques in defining the structure of mixed metal oxide materials [15, 16]. The software P has been used to perform the combined data refinement [8].

The structural model is first defined in terms of a space group, positional coordinates and occupancies, as in a normal Rietveld data refinement [17, 18]. Then the program calculates the radial distribution, within a pre-defined limit, for each atom for which EXAFS spectra are available. After that, for each structurally unique site occupied by these atoms several cluster will be generated, and the program determines the point group.

Because some of the cation positions were randomly occupied in the doped systems, a reverse Monte-Carlo (RMC) approach was used for the data refinement [19]. In this RMC calculation, a structural model is modified by random processes in order to improve the agreement between a set of experimental data, usually a structure factor, and the corresponding quantity calculated from the model. The function used in the RMC to represent the difference between the experimental and calculated data is quite complex and it is given by:

$$\chi^2 = \sum_i [A_i^c(Q_i) - A_i^e(Q_i)]^2 / \sigma_i^2(Q_i)$$

where A_i^e is the experimental structure factor, measured at the points Q_i, A_i^c is the calculated structure factor and σ is a measure of the experimental error.

3.5 References

1. Noh, J., et al., Rev. Sci. Instrum., **2007**, 78, 072205(1-6).
2. Siemons, M., T.J. Koplin, and U. Simon, Appl. Surf. Sci., **2007**, 254**,** 669-676.
3. Hattrick-Simpers, J.R., et al., Appl. Surf. Sci., **2007**, 254, 734-737.
4. Lewis, G.J., et al., J. Alloy. Compd., **2007**, 446, 355-359.
5. Kukuruznyak, D.A., et al., Appl. Phys. Lett., 2007, 91, 071916(1-3).
6. Hasegawa, K., et al., Appl. Surf. Sci., 2004, 223, 229-232.
7. Tromp, M., et al., A.I.P., **2007**, CP 882, 858-860.
8. Binsted, N., et al., J. Am. Chem. Soc., **1996**, 118, 10200-10210.
9. Henderson, S.J., et al., J. Mat. Chem., 2005, 15, 1528-1536.
10. Henderson, S.J., *High Throughput and Traditional Routes Towards Functional Oxide and Oxide-Nitride Materials*, in *School of Chemistry*. **2006**, Southampton University: Southampton.
11. Bateman, J.E., et al., Nucl. Instr. Methods Res. A-Accel. Spectr. Detec. Ass. Equip., **2007**, 580, 1526-1535.
12. Ning, G.R. and R.L. Flemming, J. of Appl. Crystallogr., **2005**, 38, 757-759.
13. www.bruker-axs.de,
14. Smith, D.K. and R. Jenkins, J. Res. Nat. Inst. Stand. Tech., **1996**, 101, 259-271.
15. Binsted, N., M.T. Weller, and J. Evans, Phys. B-Cond. Matter, **1995**, 209, 129-134.
16. Binsted, N., et al., J. Synchr. Rad., **2001**, 8, 305-307.
17. Rietveld, H.M., J. of Appl. Crystallogr., **1969**, 2, 65-71.
18. McCusker, L.B., et al., J. Appl. Crystallogr., **1999**, 32, 36-50.
19. McGreevy, R.L., Nucl. Instr. and Meth. in Phys. Res. A, **1995**, 354, 1-16.

CHAPTER FOUR

BIMOVOX

Chapter Four: BiMoVOX

4.1 Crystal structure of BiMoVOX

The synthesis of $BiVO_4$ at temperatures above 500°C has been reported to produce a monoclinic distorted scheelite type crystal structure with space group I112/b, whereas molybdenum doping of the $BiVO_4$ material leads to a tetragonal scheelite type crystal structure with space group $I4_1/a$ [1]. In the $Bi_{1-x/3}Mo_xV_{1-x}O_4$ solid phase structure the Mo^{6+} seems to directly replace V^{5+} in the scheelite structure. This structure consists of isolated MeO_4 (with Me = V or Mo) tetrahedra, with V-O bond lengths of about 1.73 Å in both monoclinic and tetragonal phase and Mo-O bond lengths of about 1.77 Å, the two being interconnected by BiO_8 triangulated dodecahedron, Figure 1. Six different VO_4^{3-} tetrahedra are involved in the Bi^{3+} coordination: in the tetragonal phase Bi^{3+} is surrounded by 8 oxygen atoms with nearly equivalent bond lengths (4 x 2.45 Å, 4 x 2.49 Å), whereas in the monoclinic form the Bi^{3+} has a more distorted environment with a wider range of Bi-O distances (2 x 2.35 Å, 2 x 2.37 Å, 2 x 2.52 Å, 2 x 2.63 Å) [2-5].

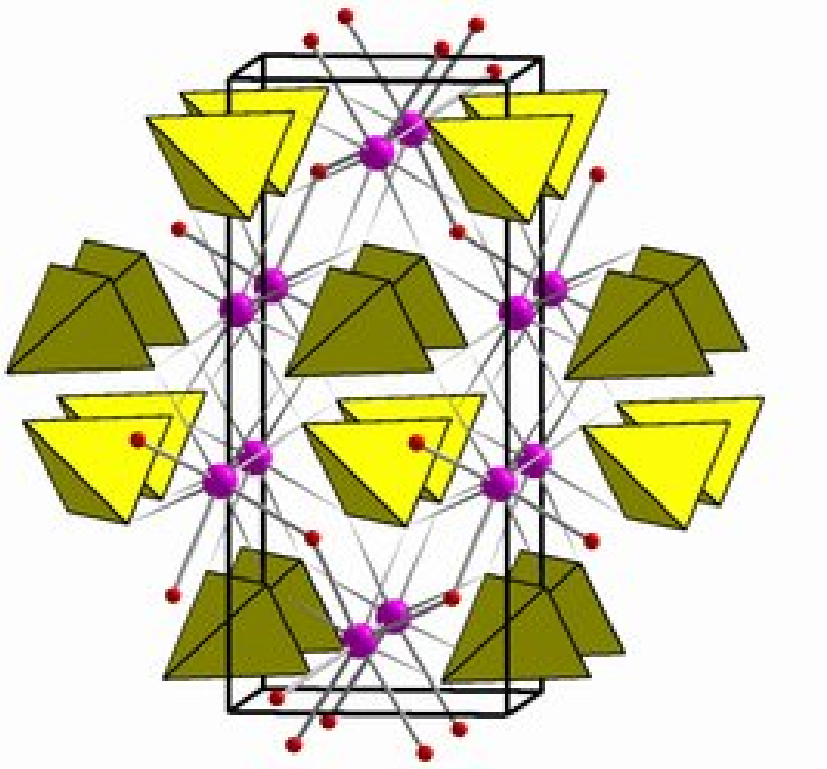

Figure 1 – The Scheelite crystal structure of $Bi_{1-x/3}Mo_xV_{1-x}O_4$ ($0.00 \leq x \leq 0.45$). Vanadium and molybdenum tetrahedra yellow, bismuth atoms violet spheres, and oxygen atoms red spheres

In this chapter synthesis and characterisation of sequential (one-by-one) and array BiMoVOX materials will be described.

4.2 XRD Powder Diffraction of BiMoVOX

The X-ray powder diffraction patterns of sequential $Bi_{1-x/3}Mo_xV_{1-x}O_4$ solid solutions synthesised by the calcination and sol-gel routes, in the range of 0.00 Òx Ò0.45, are shown in Figures 2 and 3. Figure 4 displays XRD data of the sequential sol-gel samples collected at the Synchrotron Radiation Source (SRS) with the HTP set-up using a HOTWAXS detector, while Figure 5 shows the XRD data of a BiMoVOX array collected with a Bruker D8 Diffractometer for HTP combinatorial screening.

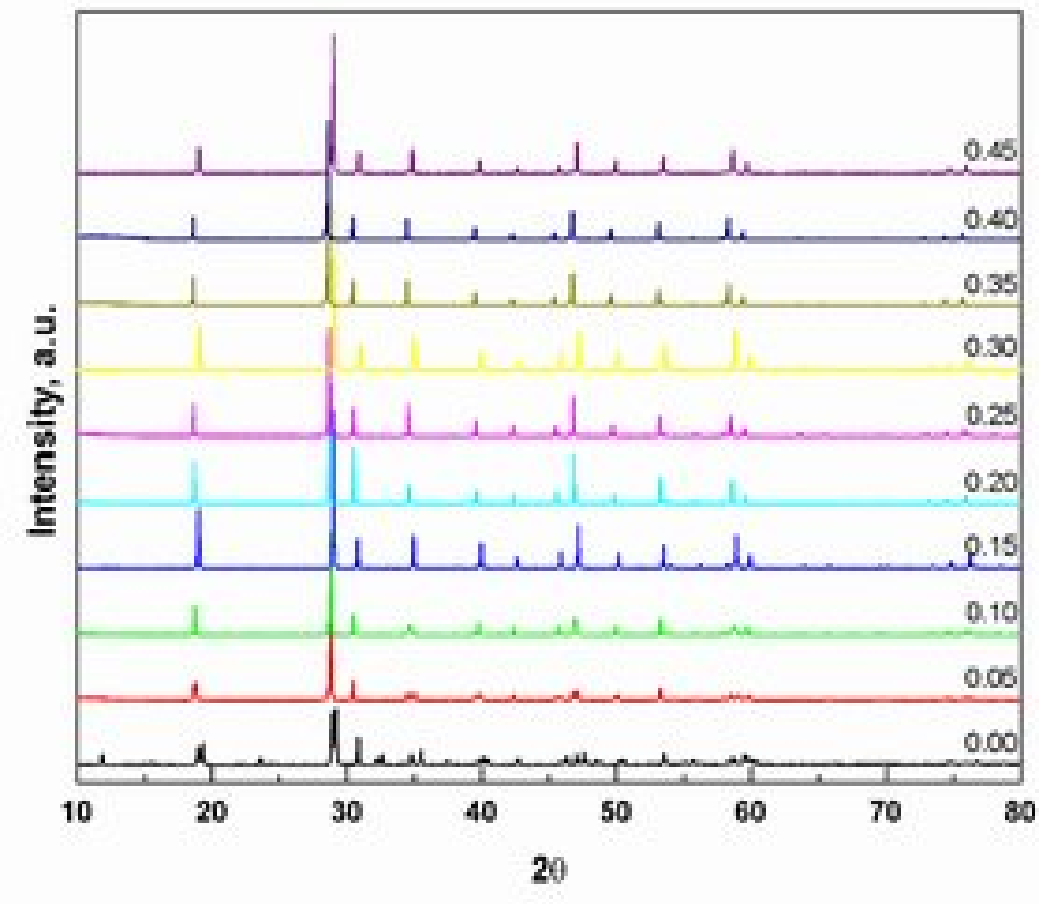

Figure 2 – The XRD powder diffraction data of $Bi_{1-x/3}Mo_xV_{1-x}O_4$ ($0.00 \leq x \leq 0.45$) sequential materials synthesised by the calcination method, collected with the Siemens D5000 diffractometer

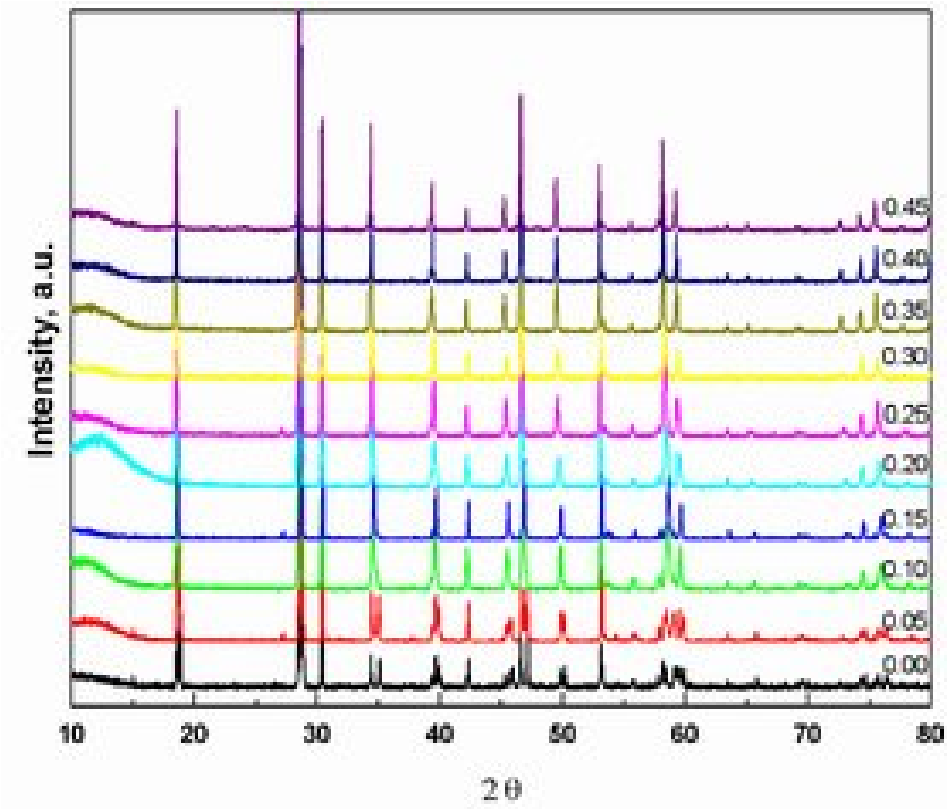

Figure 3 – The XRD powder diffraction data of $Bi_{1-x/3}Mo_xV_{1-x}O_4$ ($0.00 \leq x \leq 0.45$) sequential materials synthesised by the peroxo sol-gel method, collected with the Siemens D5000 diffractometer

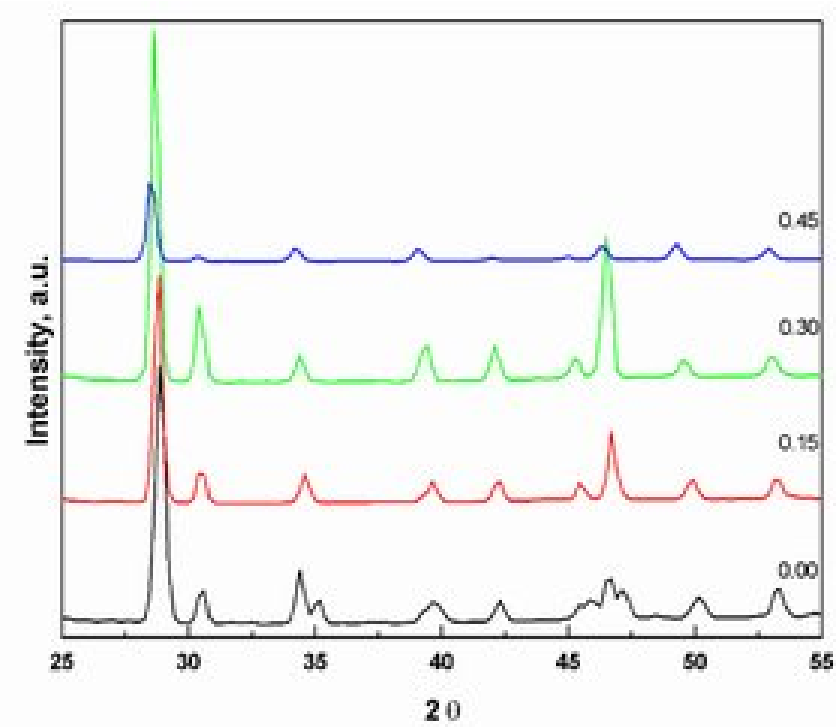

Figure 4 – The XRD powder diffraction data of $Bi_{1-x/3}Mo_xV_{1-x}O_4$ ($0.00 \leq x \leq 0.45$) sequential materials synthesised by the peroxo sol-gel method, collected at the synchrotron radiation source using a HOTWAXS detector

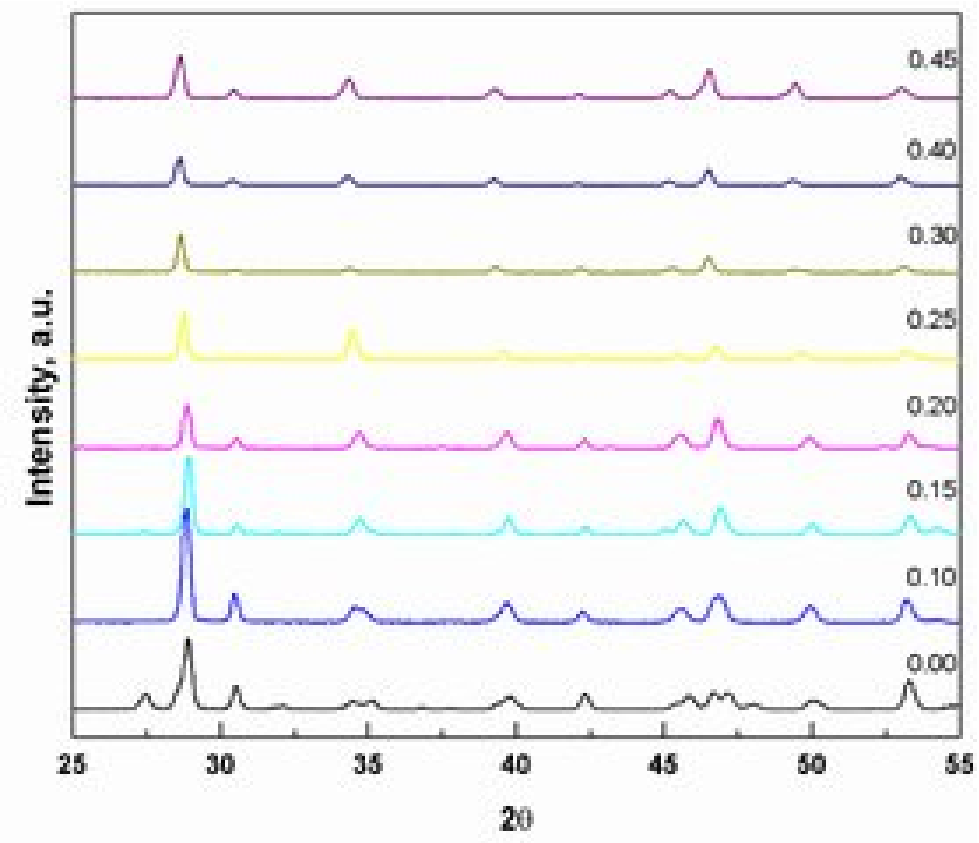

Figure 5 – The XRD powder diffraction data of the $Bi_{1-x/3}Mo_xV_{1-x}O_4$ ($0.00 \leq x \leq 0.45$) array synthesised by the peroxo sol-gel method, collected with a Bruker D8 HTP diffractometer

Lattice parameters of the sequential $Bi_{1-x/3}Mo_xV_{1-x}O_4$ solid solutions, both sol-gel and calcination, Figures 2 and 3, were refined by the least-squares method using the program GSAS [6]. Data refinement of BiMoVOX with 0.00 Òx Ò0.10 resulted in the space group I112/b, displaying the monoclinic distortion. As presented in Table 1, the lattice parameters and cell volume increase with increasing amount of molybdenum once the phase transition is completed (i.e. for $x > 0.15$). Both the XRD data obtained for the BiMoVOX array as well as for the sequential sol-gel series, using a Bruker D8 HTP diffractometer and HOTWAXS detector (at the SRS) respectively, were good enough to display the changes in the crystal structures, i.e. phase transition and cell volume growth of the doped system although, no full refinement of the data was possible.

The transition from the monoclinic to the tetragonal phase is driven by a reduction of space available to the $6s^2$ lone pair of Bi^{3+} [4]. This distortion is minimized when the V^{5+} ions are substituted with Mo^{6+} ions in the doped system [3], and appears complete for $x = 0.15$.

In particular the difference in the XRD patterns between the two vanadate polymorphs can be judged by the existence in the monoclinic $BiVO_4$ XRD pattern, of a peak at 15° and splitting of peaks at 18.5°, 35°, and 46° of 2ɗ. Furthermore with increasing of Mo^{6+} concentration the XRD peak positions shift towards lower 2θ, reflecting the changes in d-spacing and consequent volume cell growth by incorporation of the molybdenum ions into the $BiVO_4$ structure (Mo^{6+} = 0.41 Å, V^{5+} = 0.36 Å radii) [7]. Looking at the most intense peak at about 2ɗ = 28° in the diffraction patterns, this shift appears monotonic for both sol-gel sequential and array materials, Figures 3 and 4, but not for the sequential calcinations samples, Figure 2.

Different sol-gel methods of syntheses have been used to synthesize both the sequential and array BiMoVOX materials; a modified acid catalyzed sol-gel procedure as previously described suggested starting from metal alkoxide precursor solutions of vanadium (V), molybdenum (V) and Bi(III) [8, 9]. Several complexing reagents have been used (e.g. 4-hydroxy-4-methyl-2-pentanone, acetylacetone, dipivaloyl-methane, 2,2-dimethyl-1-propanol), but due to solubility problems of the molybdenum alkoxide precursor, the final solid solutions consisted of two different phases: bismuth vanadate and molybdenum oxide. However, the peroxo sol-gel method appears to be a suitable technique for the high throughput synthesis of homogeneous samples on arrays, and is used for the sol-gel samples as synthesized and studied here [10].

Table 1 - Lattice parameters of sequential $Bi_{1-x/3}Mo_xV_{1-x}O_4$ ($0.00 \leq x \leq 0.45$) sol-gel

Comp.	Crystal Struct.	Space group	a (Å)	b (Å)	c (Å)	γ (°)	Cell Volume $(Å)^3$
x = 0.00	Monoc.	I 112/b	5.1909(2)	5.0899(2)	11.6963(4)	90.374(2)	309.03(2)
x = 0.05	Monoc.	I 112/b	5.1795(2)	5.1028(2)	11.6853(4)	90.254(3)	308.84(3)
x = 0.10	Monoc.	I 112/b	5.1606(3)	5.1349(3)	11.6723(5)	90.074(1)	309.30(3)
x = 0.15	Tetr.	$I\,4_1/a$	5.1541(2)	5.1541(2)	11.6780(4)	90	310.23(2)
x = 0.20	Tetr.	$I\,4_1/a$	5.1592(2)	5.1592(2)	11.6744(5)	90	310.74(2)
x = 0.25	Tetr.	$I\,4_1/a$	5.1709(2)	5.1708(2)	11.6818(5)	90	312.35(2)
x = 0.30	Tetr.	$I\,4_1/a$	5.1802(2)	5.1800(2)	11.6883(5)	90	313.65(2)
x = 0.35	Tetr.	$I\,4_1/a$	5.1835(2)	5.1833(2)	11.6865(4)	90	314.00(2)
x = 0.40	Tetr.	$I\,4_1/a$	5.1928(1)	5.1928(1)	11.6981(3)	90	315.44(1)
x = 0.45	Tetr.	$I\,4_1/a$	5.1981(1)	5.1980(1)	11.7063(4)	90	316.31(2)

4.3 XAFS Spectroscopy of BiMoVOX

XAFS spectra of the V K edge, and Mo K edge (Figure 6), display an intense pre-edge feature at 5468 and 20012 eV in the XANES region arising from 1s to 3d and 1s to 4d dipole forbidden transitions respectively. The presence of this pre-edge feature is indicative of p-d hybridization typical of a tetrahedral environment for the x-ray-absorbing transition metal [11-13]. The increasing height of the edge step in the XAFS Mo K edge, as can be observed in Figure 6, is proportional to the amount of molybdenum in the BiMoVOX samples.

The multiple edge EXAFS analysis using the program *Excurve* [14], results for the sequential sol-gel and array series are summarized in Table 2 and Table 3. The V K edge EXAFS data have been analysed with a single shell consisting of four oxygens bonded to the vanadium, with V-O bond lengths between 1.72 and 1.73 Å for both calcination and sol-gel sequential materials, and values between 1.71 and 1.72 Å for the array. The Mo-O bond lengths as obtained from the Mo K-edge EXAFS data (Figure 7) were slightly longer, with values between 1.74 and 1.76 Å for the sequential and ~1.77 Å for the array samples, as expected. The Bi L_3 edge EXAFS data analyses, Figures 8 and 9, display two different shells consisting of four Bi-O distances each with bond lengths of ~2.35 and ~2.61 Å, another shell consisting of four Bi-O with distances of ~3.82 Å, and two shells consisting of four and two Bi-V distances of ~3.66 and ~4.00 Å , respectively. These bond lengths, relative to the first two shells, are more similar to Bi-O bond lengths in a monoclinic structure than in a tetragonal structure, suggesting a distorted environment around Bi metal.

The Bi-O first shell bond length decreases with increasing amount of Mo for x Ó0.15, once the phase transition from monoclinic to tetragonal is completed. The subsequent Bi-O and Bi-V coordination shells exhibit distances which are consistent with the monoclinic $BiVO_4$ and tetragonal $Bi(Mo,V)O_4$ crystal phases reported in the Inorganic Crystal Structure Database (ICSD) [15]. It is noteworthy that the molybdenum back-scattering amplitude is larger and out-of-phase with the vanadium back-scatterings amplitude, as such resulting in a destructive interference thereby decreasing the intensity of the second peak in the EXAFS Fourier transform, see Figure 9 vs. Figure 8, as well the number of shells in the EXAFS data analysis.

The Bi L_3 edge EXAFS data refinements of the BiMoVOX samples of the array, display only one shell of four oxygens around the Bi with a bond length of about 2.36 Å. This is due to the lower quality data obtained on the inhomogeneously deposited materials on the array in fluorescence detection mode. In general the V-O and Bi-O (first shell) bond lengths values calculated from the EXAFS BiMoVOX data array, were similar to the EXAFS data of both the sol-gel and calcination sequential materials whereas the Mo-O bond lengths are slightly higher.

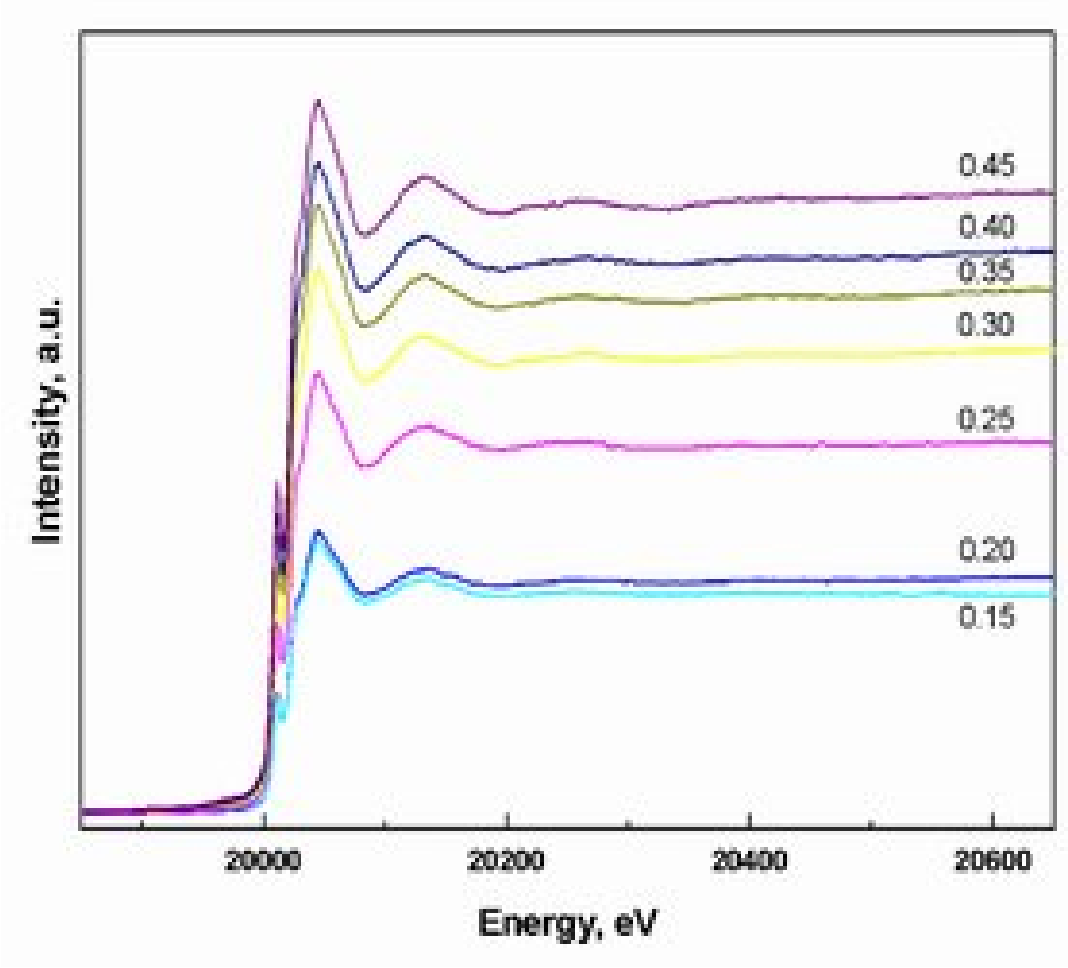

Figure 6 – The experimental raw Mo K XAFS data for the $Bi_{1-x/3}Mo_xV_{1-x}O_4$ ($0.15 \leq x \leq 0.45$) sequential sol-gel materials

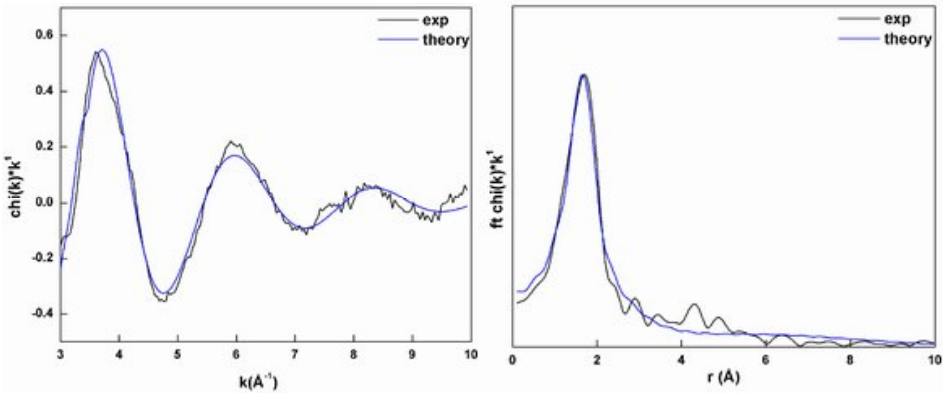

Figure 7 – The experimental raw and fitted k^1-weighted Mo K edge EXAFS (left) and Fourier transform (right) of the BiMoVOX sequential sol-gel material with x = 0.45

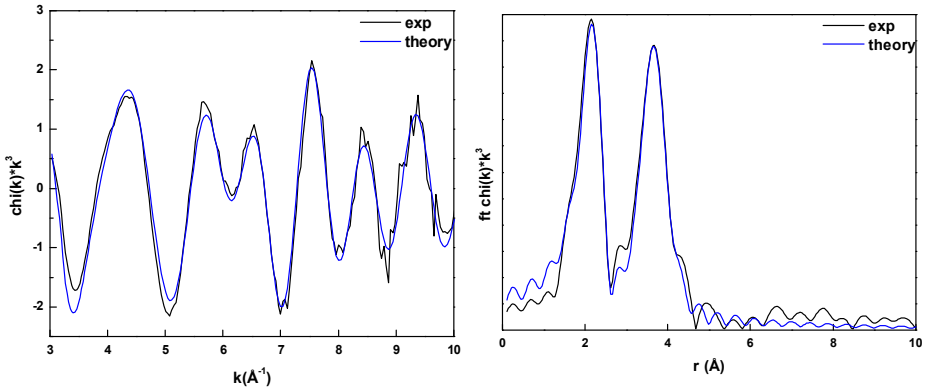

Figure 8 – The experimental raw and fitted k^3-weighted Bi L_3 edge EXAFS (left) and Fourier transform (right) of monoclinic $BiVO_4$ sequential sol-gel material

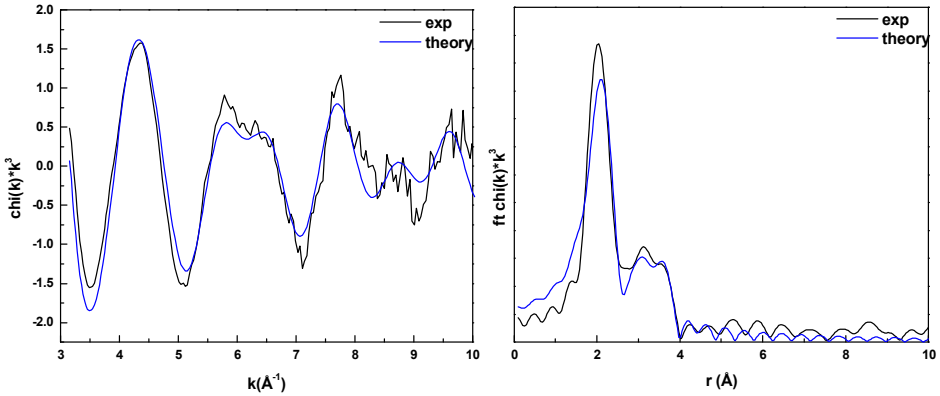

Figure 9 – The experimental raw and fitted k^3-weighted Bi L_3 edge XAFS (left) and Fourier transform (right) of the tetragonal BiMoVOX sequential sol-gel material with x = 0.45

Table 2 - Bond length (Å) of sequential (sol-gel and calcination) $Bi_{1-x/3}Mo_xV_{1-x}O_4$ ($0.00 \leq x \leq 0.45$), calculated from the EXAFS both V and Mo K edge and Bi L_3 edge data analysis

Sample	V-O (s.g.)	Mo-O (s.g.)	Bi-O (s.g.)	Bi-O (s.g.)	Bi-V (s.g.)	Bi-O (s.g.)	Bi-V (s.g.)	V-O (cal.)	Mo-O (cal.)
	C.N.=4	4	4	4	4	4	2	4	4
0.00	1.72(1)	-	2.34(1)	2.63(2)	3.69(1)	3.78(2)	4.04(3)	1.72(1)	-
0.05	1.72(1)	-	2.35(1)	2.63(2)	3.68(1)	3.84(5)	3.99(5)	1.72(1)	-
0.10	1.73(1)	-	2.36(1)	2.61(1)	3.66(2)	3.80(2)	-	1.72(1)	-
0.15	1.72(1)	1.74(1)	2.37(2)	2.61(4)	3.66(2)	3.82(2)	-	1.72(1)	-
0.20	1.72(1)	1.75(1)	2.36(1)	2.60(3)	3.66(1)	3.81(2)	-	1.72(1)	1.75(1)
0.25	1.72(1)	1.76(1)	2.35(1)	2.61(3)	3.61(1)	3.83(2)	-	1.72(1)	1.75(1)
0.30	1.72(1)	1.74(1)	2.37(1)	2.67(3)	3.71(2)	3.89(2)	-	1.72(1)	1.74(1)
0.35	1.72(1)	1.74(1)	2.34(1)	2.63(2)	3.68(2)	3.84(2)	-	1.73(1)	1.75(1)
0.40	1.72(1)	1.74(1)	2.33(1)	2.61(2)	3.66(1)	3.83(2)	-	1.72(1)	1.75(1)
0.45	1.73(1)	1.75(1)	2.31(2)	2.60(2)	3.66(2)	3.82(2)	-	1.72(1)	1.75(1)

(C.N. = coordination number)

Table 3 - Bond length (Å) of $Bi_{1-x/3}Mo_xV_{1-x}O_4$ ($0.00 \leq x \leq 0.45$) array, calculated from the EXAFS both V and Mo K edge and Bi L_3 edge data analysis

Sample	V-O (array)	Mo-O (array)	Bi-O (array)
	C.N.=4	4	4
0.00	1.71(1)	-	2.36(3)
0.05	-	-	-
0.10	-	-	-
0.15	-	-	-
0.20	1.71(1)	1.77(1)	2.36(2)
0.25	1.71(1)	1.77(1)	2.36(2)
0.30	-	-	-
0.35	1.71(1)	1.77(1)	2.35(2)
0.40	1.72(1)	1.77(1)	2.33(3)
0.45	1.72(2)	1.77(1)	2.34(2)

(C.N. = coordination number)

4.4 Combined XRD/EXAFS data refinement of BiMoVOX

The multi-edge XAFS and PD data were initially analysed by combined refinement using the program P [16]. This allowed both a simultaneous (high throughput) and sequential refinement of the seven sets of tetragonal-phase sol-gel data, the former assuming a polynomial representation of the structural and thermal parameters. There was a clear improvement in the fits for the sequential refinements, especially for the diffraction data. The structural and thermal parameters show few differences except that the clear trend seen in the x-ray thermal parameters and in oxygen x-coordinate obtained from the simultaneous refinement was not observed for the sequential refinements. The simultaneous refinement therefore has the clear advantage in revealing overall structural trends more readily, as well as being faster.

The changes across the compositional range of sequential $Bi_{1-x/3}Mo_xV_{1-x}O_4$ (with 0.15 Òx Ò0.45) that were revealed are:

- An increase in cell volume with Mo content, showing a very small positive departure from Vegardôs law.

- Movement of the oxygen towards and then away from the y-axis, in approximately the direction of a cell diagonal, as revealed by parallel curves for Ox, Oy and Oz versus composition.

- An increase in average (V, Mo)-O distance from 1.74 to 1.77 Å.

- The monoclinic $BiVO_4$ sol-gel data were analysed using a single combined refinement.

It should be noted that none of the fits are very good. The diffraction fits are best at x = 0.3, and deteriorate away from this composition, suggesting that lattice distortions are at a minimum for this composition. The Fourier transforms of the EXAFS of the tetrahedral phases show the distances obtained are too long for the vanadium and too short for the molybdenum, indicating that local lattice distortions must be present, allowing for optimum cation site sizes. Bond valence calculations confirm that V^{5+} is significantly under-bonded in the average site.

The Bi L3-edge XAFS is very badly described by the dodecahedron model, and indicates a very different local structure for Bi either due to static or anomalous thermal disorder. Indeed, it can be much better fitted in I112/b suggesting that the local environment observed in the monoclinic phase is preserved in the tetragonal phase.

In order to provide a better model for local structure, the sequential refinements were used as a basis for reverse Monte-Carlo (RMC) calculations for $BiVO_4$, Figure 10-12, $Bi_{.95}Mo_{.15}V_{.85}O_4$, and $Bi_{.85}Mo_{.45}V_{.55}O_4$ in which a simulation box, comprising multiples of the unit cell, is progressively distorted by means of small random displacements of atoms, retaining only those displacements which give rise to an overall improved fit to the XAFS and diffraction data. The method used, which allows for multiple-scattering of the photoelectron and imposes an overall crystallographic symmetry on the system has been previously reported [17].

The RMC fit gave rise to the expected size-difference between V and Mo sites, and showed that Bi has a highly distorted environment characterized by a maximum in the Bi-O atomic distribution at short distances followed by a long tail. Although the quality of the diffraction data was insufficient to reliably demonstrate net movement of atoms from their average crystallographic positions, the results indicate that distortion of the oxygen lattice; together with a difference in the positional coordinates for V and Mo appear to be the primary cause of the structure observed. We have particularly focussed our attention on the vanadium site, which is strongly influenced by the bismuth lone pair distortion.

As discussed in the previous section, individual $BiVO_4$ refinement of the V K edge EXAFS and XRD data results in one shell consisting of four oxygens bonded to the vanadium in a tetrahedral coordination with an average bond length of 1.72(2) Å. With the combined RMC calculation it has been possible to separate the four oxygen atoms into two distinct shells with bond lengths, represented by the first cumulant of the V-O atomic distribution function [18], of 1.70 and 1.75 Å respectively, displaying the bismuth lone pair distortion effect on the VO_4 tetrahedra, Table 4. For the BiMoVOX materials with x = 0.15 and x = 0.45, there is only one crystallographic site which gives average V-O and Mo-O bond lengths of 1.73 Å and 1.75 Å respectively, however we note that both the tetrahedra are still distorted for all composition. These results reflect a reduction of the bismuth lone pair distortion on the vanadium site due to the Mo^{6+} doping.

Table 4 - Bond length (Å) of sequential sol-gel $BiVO_4$ and $Bi_{1-x/3}Mo_xV_{1-x}O_4$ (x = 0.45) calculated by EXAFS and XRD/EXAFS combined data refinement

Sample	C.N. (EXAFS)	V-O (EXAFS)	Mo-O (EXAFS)	C.N. (XRD/EXAFS)	V-O (XRD/EXAFS)	Mo-O (XRD/EXAFS)
0.00	4	1.72(1)	-	2 2	1.70(1) 1.75(1)	-
0.45	4	1.73(1)	1.75(1)	4	1.73(1)	1.75(1)

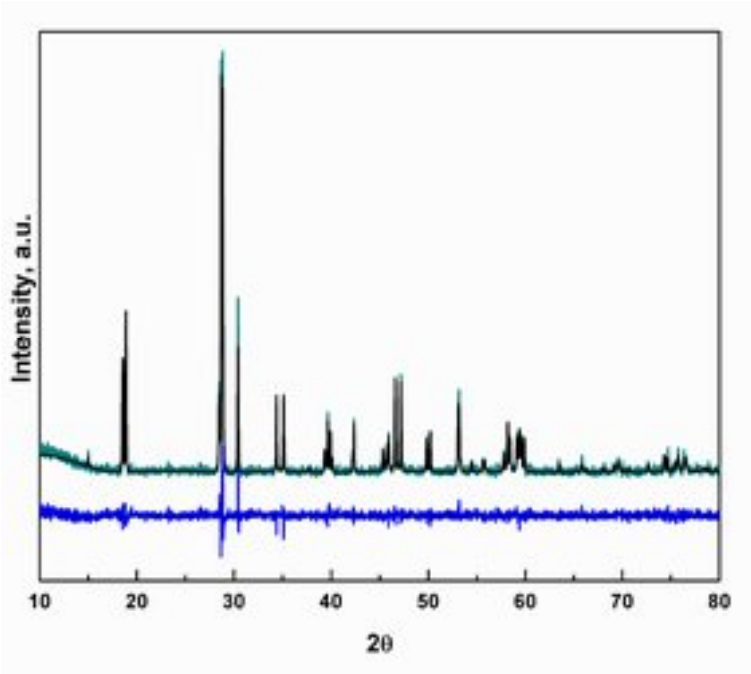

Figure 10 – Combined Rietveld refinement fit for the sequential sol-gel monoclinic $BiVO_4$; obtained from PXD data collected on a Siemens D5000. The lower trace (black) is the observed intensities, the upper trace (dark-cyan) the calculated profile, and the lower line (blue) the difference.

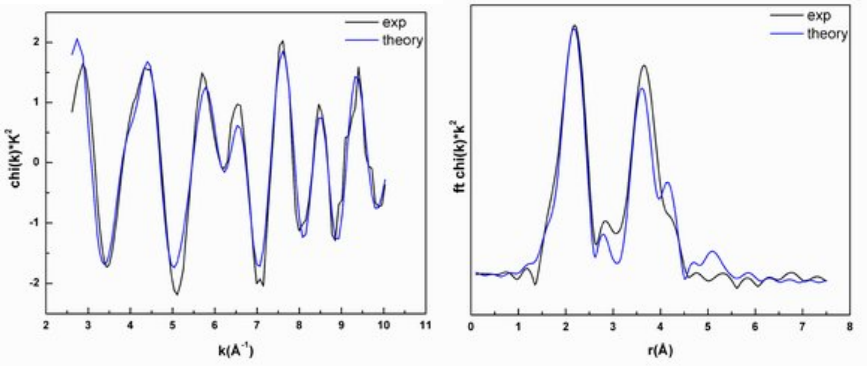

Figure 11 – The combined experimental raw and fitted k^2-weighted Bi L_3 edge EXAFS (left) and Fourier transform (right) of sequential monoclinic $BiVO_4$

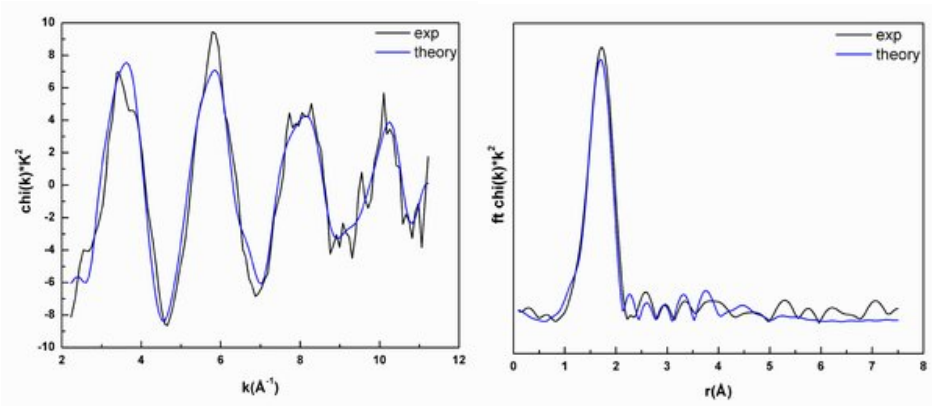

Figure 12 – The combined experimental raw and fitted k^2-weighted V K edge EXAFS and Fourier transform of sequential monoclinic $BiVO_4$

4.5 Raman Spectra of BiMoVOX

The four oxygen atoms in tetrahedral coordination around both V^{5+} and Mo^{6+} form strongly bound molecular anions MeO_4, which are bonded to Bi^{3+} cations in the lattice via relatively weak long-range ionic forces. Consequently modes within the MeO_4 anions, internal modes, are stronger than those of external modes, corresponding to vibrations between lattice ions. The Raman spectra thus mainly reflect the structure of the MeO_4 tetrahedrons in the scheelite structure, as can be seen in the Figures 13 and 14 displaying the sequential and array sol-gel series respectively. According to the site symmetry approach [19], the Raman band at 900 cm^{-1} can be attributed to the ν_1 symmetric stretching mode of the Mo-O bonds, while the Raman bands at 832 and 730 cm^{-1} are attributed to the ν_1 symmetric and ν_3 antisymmetric stretching modes of V-O bonds. The Raman band at 660 cm^{-1} is assigned to the asymmetric stretching vibration of the longer V-O bonds, suggesting a tetrahedral coordination for V^{5+} with two different V-O bond lengths in the monoclinic samples of the series [20, 21]. The intensity of the Mo-O symmetric mode increases with increasing amount of Mo doping: while the intensity of the V-O symmetric mode decreases.
The peaks at lower wavenumbers, i.e. at ~380 and ~340 cm^{-1}, are the bending motions or so-called ν_4 and ν_2 frequencies. External modes (frustrated rotation / translation) occur at 290, 227, 187, 160 and 145 cm^{-1} [22]. The positions of both the stretching and bending motions shift with the increasing amount of Mo ions in the solid solution, suggesting the crystal structure changes with increasing amount of Mo. This is consistent with the XRD and UV-visible results.

The influence of the changes in the V-O bond lengths within the VO_4 tetrahedra is evident from both the ν_4 and ν_2 modes as can be seen in Table 5:
The ν_4 vibration shifts towards to lower energy while at the same time the ν_2 mode shifts towards higher energy, during the monoclinic to tetragonal phase transition for 0.00 Òx Ò0.15 converging to similar values. This phenomenon can be explained by the fact that during the phase transition from monoclinic $BiVO_4$ phase to the tetragonal $Bi_{1-x/3}Mo_xV_{1-x}O_4$ (completed for x = 0.15); two of V-O bonds become longer (from 1.70 to 1.72 Å) decreasing the ν_4 asymmetric bending mode energy, while at the same time the other two V-O bonds become shorter (from 1.75 to 1.72 Å) increasing the ν_2 symmetric bending mode energy. This result confirms the reduction of the bismuth lone pair distortion on the vanadium site shown by the combined XRD/EXAFS data refinement. Slight changes can be also seen in both the V-O and Mo-O ν_1 stretching mode.
The V-O ν_1 frequency shifts towards lower energy for x Ò0.15, whereas, for x Ó0.20 the reverse is observed for both V-O and Mo-O ν_1, indicating a decreasing of the covalence of the V-O bonds for 0.00 Òx Ò0.15 and vice versa an increasing of the covalence of both the V-O and Mo-O bonds for samples with for x Ó0.20. In addition to a change in energy position, the full-width-at-half-maximum (FWHM) value of the V-O ν_1 stretching mode band increases monotonically with Mo doping, displaying an increase of defects and a lower crystallinity for the more doped samples.

Franklin and Wachs provided an empirical expression to correlate both the V-O and Mo-O bond lengths with the Raman stretching frequencies, using the Diatomic Approximation (no site symmetry) [23, 24]. In this approximation, the Raman band at about 900 cm^{-1} arises from stretches of a Mo-O bond with a bond length of 1.74 Å, through the whole series, whereas the Raman bands at about 832 and 730 cm^{-1} are due to stretches of distinct V-O bonds with bond lengths of 1.69 Å and 1.76 to 1.73 Å, going through the series. These Raman bond distances are similar to the combined XRD/EXAFS determined bond distances (Table 2 and Table 3) for the first samples of the series, and suggest the reduction of the effect of the bismuth lone pair distortion on the vanadium site. The external modes refer to the relative motions, i.e. translation and rotation, of the Bi and $V(Mo)O_4$ ions, since the $Bi_{1-x/3}Mo_xV_{1-x}O_4$ lattice in essence consists of two sub-lattices formed by Bi and $V(Mo)O_4$ units. Although it is difficult to assign the specific single frequencies to specific external vibration modes, these BiMoVOX external modes frequencies have similar values to values reported in investigations on orthovanadate scheelite materials.

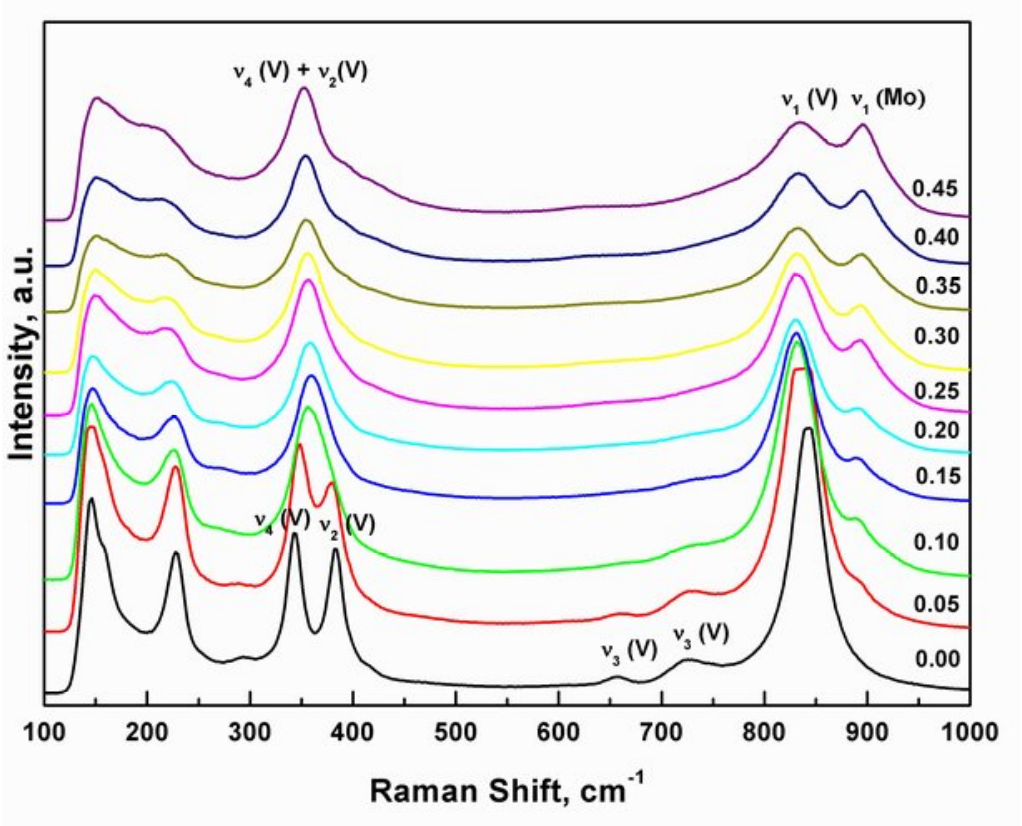

Figure 13 – Raman spectra of $Bi_{1-x/3}Mo_xV_{1-x}O_4$ ($0.00 \leq x \leq 0.45$) sequential series made by the peroxo sol-gel method

Raman data analysis of BiMoVOX array materials, Figure 14, shows similar results compared to the sequential BiMoVOX sol-gel, Figure 13. Bond lengths calculated from the Mo-O and V-O stretching modes were about 1.75 Å and 1.70 and 1.76 Å for the V-O bonds [23, 24]. The FWHM value of the V-O ν_1 stretching mode band did not increases monotonically with Mo doping as in the sequential sol-gel samples even though it had similar values (between 40 and 70 cm^{-1}). Furthermore, in the ν_4 bending mode as a function of unit cell parameters follows the same trend. The intensities of the Raman spectra of the samples in the array are lower compared with those obtained for the sequential sol-gel samples. They also do not change monotonically with the relative amount of vanadium and molybdenum ions. These differences can be related to the different thickness and flatness of the samples made on the array, together with their not being completely homogeneous. Also the Raman spectra of sequential BiMoVOX calcination materials, Figure 15, display lower peak intensity compared with the sequential sol-gel materials due to their lower crystallinity and more defective structure.

Both V-O ν_1 and Mo-O ν_1 frequency shifts statistically towards higher values; the calculated Mo-O and V-O bond length values were, respectively, about 1.74 Å and 1.69 Å. The V-O distances refine to be shorter by ~0.3 Å as compared with the same bond lengths calculated from the EXAFS data refinement, Table 2, [23]. The FWHM value of the V-O ν_1 stretching mode band did not increases monotonically with Mo doping, with values between 60 and 80 cm^{-1}. Furthermore we observed one broad peak assigned to the $\nu_2 + \nu_4$ bending modes.

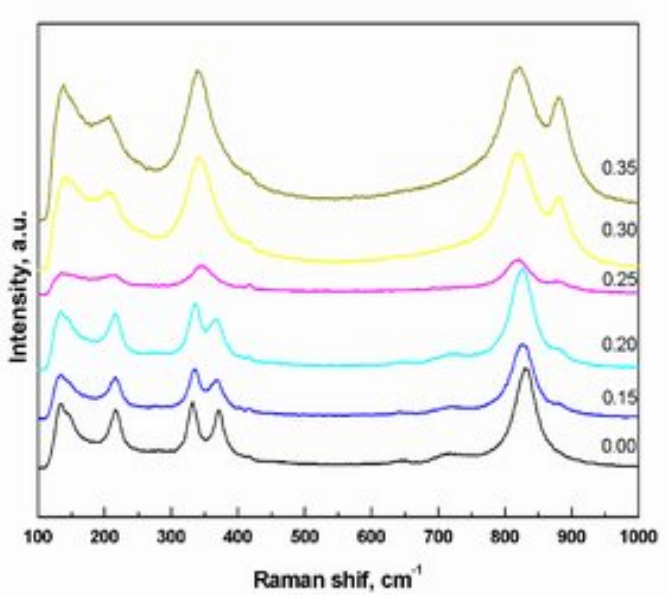

Figure 14 – Raman spectra of $Bi_{1-x/3}Mo_xV_{1-x}O_4$ ($0.00 \leq x \leq 0.45$) array made by the peroxo sol-gel method

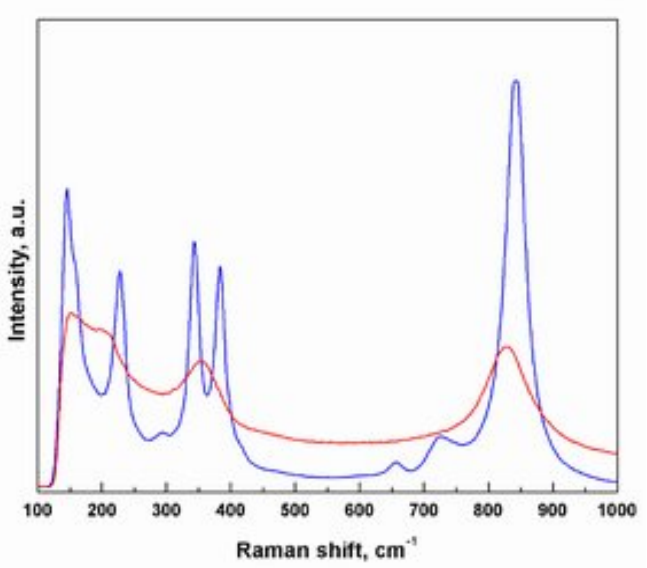

Figure 15 – Raman spectra of sequential monoclinic $BiVO_4$ made by calcination (red) and the peroxo sol-gel (blue) method

Table 5 - Results of the Raman spectral analysis (cm^{-1}) of sequential $Bi_{1-x/3}Mo_xV_{1-x}O_4$ ($0.00 \leq x \leq 0.45$) sol-gel

Vibr. mode	0.00	0.05	0.10	0.15	0.20	0.25	0.30	0.35	0.40	0.45
ν_s (Mo-O)	0	895	894	895	895	896	896	897	897	897
ν_s (V-O) FWHM	842 38	836 49	831 48	831 46	830 48	832 57	832 58	832 62	833 63	834 72
ν_{as} (V-O)	726	728	733	734	737	746	754	755	762	771
ν_{as} (V-O)	656	659	-	-	-	-	-	-	-	-
δ_s $(VO_4)^{3-}$	383	379	373	371	369	365	364	362	363	360
δ_{as} $(VO_4)^{3-}$	343	348	352	354	353	354	354	353	352	351

Where: ν_s = symmetric stretching mode, ν_{as} = asymmetric stretching mode, δ_s = bending mode and δ_{as} = antisymmetric bending mode (out-of-plane)

4.6 UV-visible Diffuse Reflectance Spectra and SEM of BiMoVOX

UV-visible spectra of the $Bi_{1-x/3}Mo_xV_{1-x}O_4$ materials made by the sol-gel method were monotonically red-shifted for values of x Ò0.10, while they were blue-shifted for values of x Ó0.15, Figure 16 (left). These results, displaying only a single optical edge for each sample, indicate that the powders obtained were homogeneous solid-solutions, rather than a mixture of vanadium and molybdenum oxides. The optical trend is clearly visible in Figures 16 (right) and 18 in which the band gaps of both BiMoVOX materials made by the sol-gel and by the calcination methods are shown.

Two effects need to be taken into account to explain the colour properties observed (1): the bismuth lone pair distortion, and (2) the contribution of the Mo^{6+} to the overall electronic conduction bands of the BiMoVOX materials. The valence bands of both pure $BiVO_4$ and $Bi_{1-x/3}Mo_xV_{1-x}O_4$ are composed by hybridisation of the Bi 6s and O 2p orbitals, while the V 3d in $BiVO_4$ and the mixed V 3d and Mo 4d orbitals in the BiMoVOX contribute to form the bottom of the conduction band, Figure 17. Previous papers report that as a result of the reduction of the bismuth lone pair distortion, the electron band gap value decreases by about 0.2 eV, when the phase transition from the monoclinic to tetragonal $BiVO_4$ phase takes place [4]. At the same time, as the effective electronegativity of the V^{5+} (2.49) ion is higher than the Mo^{6+} (2.33) ion, molybdenum doping results in an increase in the band gap value of the electronic transition [3, 25-29]. This effect becomes clear once the phase transition is completed, for x Ó0.15.

Samples made by the calcination method show similar UV-visible properties to the sol-gel ones, Figure 18, even though they have overall smaller band gap energies values. It is known that both colour intensities and photophysical properties of $BiVO_4$, and consequently of $Bi_{1-x/3}Mo_xV_{1-x}O_4$, are strongly influenced by the method of preparation [30].

Heating of metal oxides at high temperature (above 500 °C) creates oxygen ion vacancies inside the crystal lattice, which are positively charged structural defects able to capture one or two electrons. The oxygen vacancies occupied by electrons act as donor centres whose level lies close to valence band. These donor centres are in the forbidden gap and form a narrow donor band at about 0.3 eV below the conduction band and, as a consequence, with a band-gap narrowing effect [31, 32]. In our case, materials made by the sol-gel route were fired at 700 °C in an oxygen atmosphere, whereas the calcination materials were fired at the same temperature but in an air atmosphere, giving rise to the smaller overall band gap. In order to reduce the concentration of these oxygen vacancies, the BiMoVOX sample for x = 0.35 made by calcination method was fired, subsequently, in an oxygen atmosphere at 700 °C. As displayed in Figure 18 and Figure 19, there is a clear blue shift of the optical band edge due to the increase in the band gap value, close to that of the same BiMoVOX material made by sol-gel method. The intensity of the reflectance curves is higher for the sol-gel samples (50 ÒR% Ò70) than for the calcination samples (30 ÒR% Ò50). Both the BiMoVOX materials have particles with an irregular shape and size in a range of 0.2 Òμm Ò1.0, as can be seen in the SEM and TEM pictures in Figure 20 and Figure 21, respectively. The sol-gel materials have a smoother shape, while the calcination materials have a more irregular shape, i.e. resultant more absorption compared with the sol-gel materials.

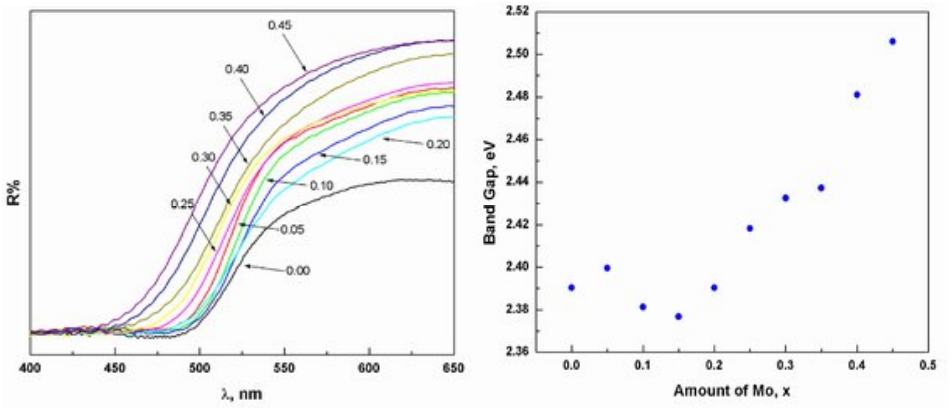

Figure 16 – UV-visible reflectance spectra (left) and band gap energies (right) of sequential $Bi_{1-x/3}Mo_xV_{1-x}O_4$ ($0.00 \leq x \leq 0.45$) materials made by the peroxo sol-gel method

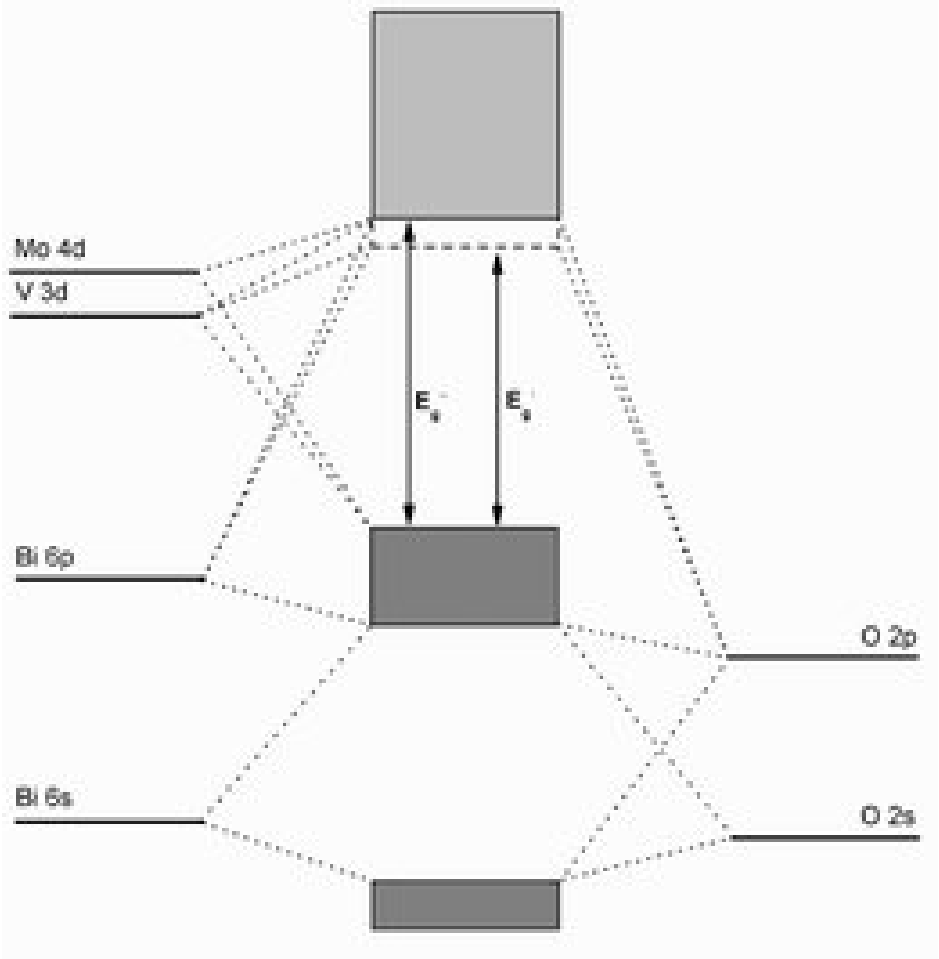

Figure 17 – Schematic molecular orbital diagram of the sequential BiMoVOX materials; E_g' = band gap of monoclinic $BiVO_4$ and E_g'' = band gap of tetragonal $Bi_{1-x/3}Mo_xV_{1-x}O_4$

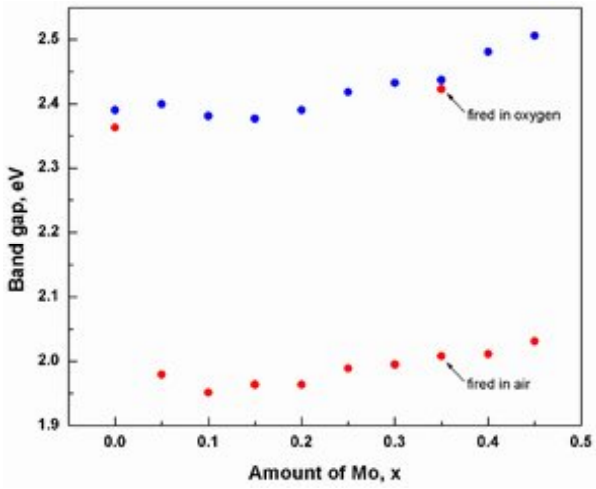

Figure 18 – Band gap energies of sequential $Bi_{1-x/3}Mo_xV_{1-x}O_4$ ($0.00 \leq x \leq 0.45$) materials made by the peroxo sol-gel method (blue) and calcination (red) method

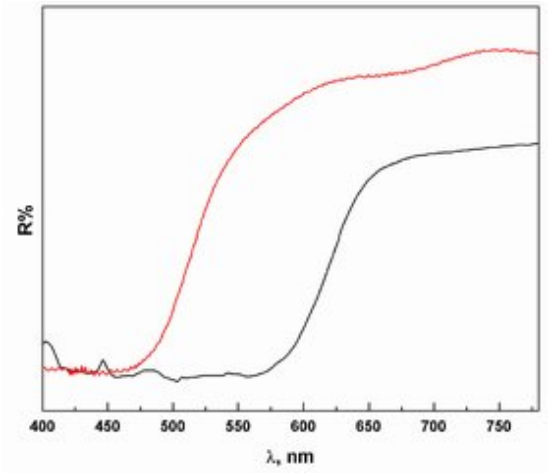

Figure 19 – UV-visible reflectance spectra of sequential BiMoVOX (x = 0.35) material made by calcination method and fired in air (black) and then in oxygen (red) atmosphere (700°C)

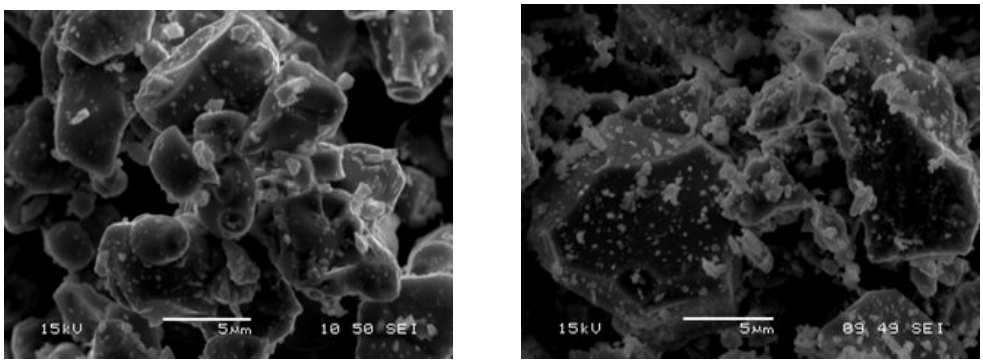

Figure 20 – SEM photographs of sequential BiMoVOX materials made by the peroxo sol-gel method (left) and calcination (right) method

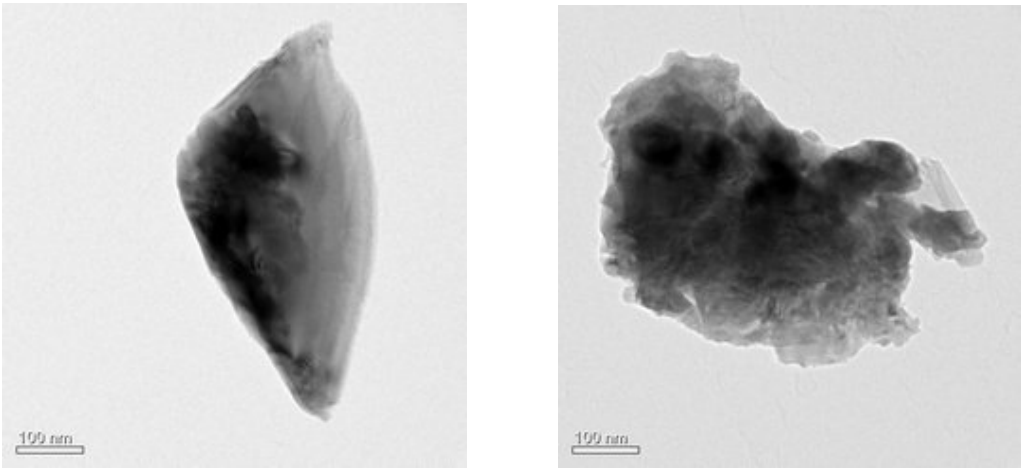

Figure 21 – TEM photographs of sequential $BiVO_4$ materials made by the peroxo sol-gel method (left) and calcination (right) method

4.7 Conclusions

The synthesis of $BiVO_4$ at temperatures around 700°C produced monoclinic distorted scheelite crystal structure. A combined characterization approach of complementary techniques, i.e. XRD powder diffraction, Raman and XAFS spectroscopy reveals that molybdenum doping of monoclinic $BiVO_4$ leads to tetragonal $Bi_{1-x/3}Mo_xV_{1-x}O_4$, in which the Mo^{6+} directly replaces the V^{5+} in the scheelite structure. The multi-edge XAFS and PD combined data refinement of the BiMoVOX materials, performed using the program P shows a clear improvement in the fits for the sequential material, especially for the diffraction data. Doping produces materials ranging in colour from yellow-red to yellow-green depending on the Mo^{6+} content.

Arrays of vanadium molybdenum mixed metal oxide compounds are prepared in a high-throughput manner, with the peroxo sol-gel route, using robotic methodologies. These arrays can successfully be analysed for their structural and compositional properties in a rapid manner providing an increase in efficiency compared to one-at-a-time experiments.

4.8 Experimental Section

4.8.1 Preparation of BiMoVOX Sequential Materials

Two different methods of synthesis have been utilised to obtain BiMoVOX ($Bi_{1-x/3}V_{1-x}Mo_xO_4$, with 0.00 Òx Ò0.45) materials: (1) a solid state calcination procedure and (2) a peroxo sol-gel route.

Solid state calcination procedure:

Calcination specimens were prepared from monoclinic Bi_2O_3 (99%, Alfa Aesar), orthorhombic V_2O_5 (99.2%, Alfa Aesar) and orthorhombic MoO_3 (99.5%, Alfa Aesar), with different cation ratios. In a typical calcination synthesis the mixed oxides, 0.99 g of Bi_2O_3, 0.25 g of V_2O_5 and 0.32 g of MoO_3, were ground with acetone (1-2 ml) in an agate mortar with a pestle for a few minutes and subsequently placed in a gold boat and heated in an air atmosphere up to 700 °C for 24 h, followed by quenching to room temperature.

Peroxo sol-gel synthesis:

Sol-gel specimens were prepared by a peroxo sol-gel route. In a typical sequential peroxo sol-gel synthesis, bismuth nitrate solutions were prepared dissolving 1.59 g of $Bi(NO_3)_3 \cdot 5H_2O$ (98%, Alfa Aesar) in an excess of nitric acid (2M). Precursor vanadium and molybdenum solutions were prepared separately, from 0.19 g of V_2O_5 (99.2%, Alfa Aesar) and 0.31 g of $(NH_4)_6Mo_7O_{24} \cdot 4H_2O$ (99%, Alfa Aesar) both dissolved in H_2O_2 (30% w/v)/H_2O (1:1). The two peroxide solutions were then added together and stirred for 30 min. Finally the bismuth solutions were added drop-wise to the vanadium-molybdenum solutions for half an hour, while stirring was continued for a further 2 h. The mixed solutions were heated up to 120 °C in air until evaporation of the solvent was completed, after which the red-brown precipitate was heated to 700 °C for 24 h in an O_2 atmosphere, with a temperature gradient of 0.5 °C/min.

4.8.2 Preparation of BiMoVOX Arrays

Arrays of BiMoVOX materials were prepared by the peroxo sol-gel route. In a typical peroxo sol-gel array synthesis, bismuth nitrate solutions were prepared dissolving 1.73 g of $Bi(NO_3)_3 \cdot 5H_2O$ (98%, Alfa Aesar) in 7 ml of nitric acid (2M). Precursor vanadium and molybdenum solutions were prepared separately, from 0.30 g of NH_4VO_3 (99%, Alfa Aesar) dissolved in 3 ml of H_2O and 2 ml of H_2O_2 (30% w/v), and from 0.45 g of $(NH_4)_6Mo_7O_{24} \cdot 4H_2O$ (99%, Alfa Aesar) dissolved in 5 ml of H_2O and 1 ml of H_2O_2 (30% w/v).

These were dispensed into a standard 54 well plate (reusable Teflon mask system, with a 6 x 9 grid of 5 mm sized holes, pressed on an alumina tile by stainless steel plates) in the appropriate ratios and mixed using a Packard Multiprobe II robot [33]. Then the array was left for 12 hours at ambient temperature in air atmosphere, and after that, the solvent was evaporated at 60 °C overnight in an oven in air atmosphere before the alumina tile was fired up to 700 °C in a furnace in oxygen atmosphere for 24 h.

4.8.3 XRD Powder diffraction

Diffraction patterns were obtained using a Siemens D5000 (Cu $K_{\alpha 1}$ radiation, λ = 1.5406 Å) for sequential series, and a Bruker D8 Discover (Cu $K_{\alpha 1}$ radiation, λ = 1.5406 Å) with General Area Detector Diffraction System (GADDS) for HTP combinatorial screening of the arrays [34].
The HTP XRD scan time was 2 min., allowing data collection of the full array in less than 2 h. The phases were identified by comparison with the PDF2 database [35]. Data refinement of the sequential materials was performed using the GSAS program [6]. X-ray diffraction data of BiMoVOX sequential sol-gel series were also obtained at the synchrotron source (SRS, beamline 9.3, *vide infra*) using the specially designed HTP set-up. The data were collected in transmission mode, using the HOTWAXS detector, a position sensitive detector [36]. The XRD patterns were acquired at 13300 eV, λ = 0.9347 Å. Samples were diluted up to 1 wt% metal in SiO_2 in order to decrease x-ray absorption by the samples. Conversion of the position scale to d or 2θ space was performed as described in chapter three.

4.8.4 XAS spectroscopy

XAS spectroscopy studies were carried out at the Science and Technology Facility Councilôs (STFC) Synchrotron Radiation Source (SRS) at the Daresbury Laboratory (Daresbury, U.K.) and at the European Synchrotron Radiation Facility (ESRF) (in Grenoble, France). The Bi L_3 (13419 eV) and Mo K (20000 eV) edge XAS studies were performed at station 9.3 of the SRS using a Si(111) and Si(220) double crystal monochromator, respectively. Data were collected using a 13 element Ge solid state detector. The Bi L_3 edge of the sequential samples (diluted up to 1 wt% in metal) was collected in transmission mode.

V K edge (5465 eV) spectra of the sequential samples were collected at Station 7.1, while for the array they were collected at the ESRF beamline BM26A (DUBBLE). In both cases the data were obtained with a Si(111) double crystal monochromator with a 13 element Ge solid state detector. Pt foil (L_2 edge = 13273 eV) was used for the calibration of the Bi L_3 edge, with V and Mo foils for the calibration of V and Mo K edges. Data were acquired with a σk of 0.04 $Å^{-1}$ and a data acquisition time of 20 min. per scan.

The sequential samples were mounted in a self supporting sample holder. All samples were characterized in the HTP chamber, allowing combined XAS, XRD and Raman [37].
EXAFS data analysis of both sequential and array materials were performed using the *X-Mult* [38]and *Excurve(9.301)* programs [14].

4.8.5 UV/Vis and Raman diffuse reflectance

Absorption measurements of the sequential samples were performed using a Perkin Elmer Lambda 35 UV/vis spectrometer in diffuse reflectance mode. Spectra were collected in the visible range of 380 ï 780 nm. The band gaps energy values are calculated from the maximum of the first derivative of the absorption edges. Raman spectra of both bulk and array samples were collected with an optical fibre Renishaw RA100U Spectrometer, using high-power NIR laser (785 nm) with a resolution of 3 cm^{-1} in the range between 100 and 1000 cm^{-1}. Spectra were calibrated using the 520.5 cm^{-1} line of a silicon wafer.

4.8.6 Electron Microscopy

Transmission Electron Microscopy data were collected using a JEM 3010 transmission electron microscope.

Scanning Electron Microscopy data were collected using a JSM 5910 scanning electron microscope. Images of each spot were taken at 2000x magnification with a spot size of 21, accelerating voltage of 15 kV.

4.9 References

1. A.W. Sleight, H.Y. Chen, A. Ferretti, and D.E. Cox, Mater. Res. Bull., **1979**, 14, 1571-1581.
2. T. Duraisamy and A. Ramanan, Sol. St. Ion., **1999**, 120, 233-237.
3. W.F. Yao and J.H. Ye, J. Phys. Chem. B, **2006**, 110, 11188-11195.
4. M.W. Stoltzfus, P.M. Woodward, R. Seshadri, J.H. Klepeis, and B. Bursten, Inorg. Chem., **2007**, 46, 3839-3850.
5. Y.B. Abraham, N.A.W. Holzwarth, R.T. Williams, G.E. Matthews, and A.R. Tackett, Phys. Rev. B, **2001**, 64, 245109(1-10).
6. A.C. Larson and R.B. Von Dreele, *Generalised Structure Analysis System*, Los Alamos National Laboratory, Los Alamos, **2004**.
7. R.D. Shannon, Acta Crystallogr. Sect. A, **1976**, 32, 751-767.
8. J.S. Paul, J. Urschey, P.A. Jacobs, W.F. Maier, and F. Verpoort, J. Catal., **2003**, 220, 136-145.
9. J.S. Paul, P.A. Jacobs, P.A.W. Weiss, and W.F. Maier, Appl. Catal. A-Gen., **2004**, 265, 185-193.
10. W.D. Schroeder, C.J. Fontenot, and G.L. Schrader, J. Catal., **2001**, 203, 382-392.
11. J. Wong, F.W. Lytle, R.P. Messmer, and D.H. Maylotte, Phys. Rev. B, **1984**, 30, 5596-5610.
12. S.E. Shadle, B. Hedman, K.O. Hodgson, and E.I. Solomon, Inorg. Chem., **1994**, 33, 4235-4244.
13. K.D. Chen, S.B. Xie, A.T. Bell, and E. Iglesia, J. Catal., **2000**, 195, 244-252.
14. N. Binsted, *EXCURV(9.301)*. CCLRC Daresbury Laboratory Computer program, **1998**.
15. *Inorganic Crystal Structure Database, ICSD*, Karlsruhe.
16. N. Binsted, M.J. Pack, M.T. Weller, and J. Evans, J. Am. Chem. Soc., **1996**, 118, 10200-10210.
17. N. Binsted, C. Owens, and M.T. Weller, A.I.P., **2006**, CP 882, 64-68.
18. A.B. Edwards, D.J. Tildesley, and N. Binsted, Mol. Phys., **1997**, 91, 357-369.
19. K. Nakamoto, *Infrared and Raman Spectra of inorganic and Coordination Compounds*. Vol. A. **1997**, New York, Wiley Interscience. 387.
20. R.L. Frost, D.A. Henry, M.L. Weier, and W. Martens, J. Raman Spectrosc., **2006**, 37, 722-732.

21. J.Q. Yu and A. Kudo, Adv. Funct. Mater., **2006**, 16, 2163-2169.
22. C.C. Santos, E.N. Silva, A.P. Ayala, I. Guedes, P.S. Pizani*, et al*., J. Appl. Phys., **2007**, 101, 053511(1-5).
23. F.D. Hardcastle and I.E. Wachs, J. Raman Spectrosc., **1990**, 21, 683-691.
24. F.D. Hardcastle and I.E. Wachs, J. Phys. Chem., **1991**, 95, 5031-5041.
25. H.W. Eng, P.W. Barnes, B.M. Auer, and P.M. Woodward, J. Sol. St. Chem., **2003**, 175, 94-109.
26. R.T. Sanderson, Inorg. Chem., **1986**, 25, 3518-3522.
27. R.T. Sanderson, J. Chem. Educ., **1988**, 65, 112-118.
28. R.T. Sanderson, J. Chem. Educ., **1988**, 65, 227-231.
29. K. Sayama, A. Nomura, T. Arai, T. Sugita, R. Abe*, et al.*, J. Phys. Chem. B, **2006**, 110, 11352-11360.
30. M. Gotic, S. Music, M. Ivanda, M. Soufek, and S. Popovic, J. Mol. Struct., **2005**, 744, 535-540.
31. M.M. Islam, T. Bredow, and A. Gerson, Phys. Rev. B, **2007**, 76.
32. R. Sivakumar, R. Gopalakrishnan, M. Jayachandran, and C. Sanjeeviraja, Curr. Appl. Phys., **2007**, 7, 51-59.
33. S.J. Henderson, J.A. Armstrong, A.L. Hector, and M.T. Weller, J. Mater. Chem., **2005**, 15, 1528-1536.
34. G.R. Ning and R.L. Flemming, J. Appl. Crystallogr., **2005**, 38, 757-759.
35. *PCPDFWIN database*. JCPDS-International Centre for Diffraction data, **1997**.
36. J.E. Bateman, G.E. Derbyshire, G. Diakun, D.M. Duxbury, J.P.A. Fairclough*, et al.*, Nucl. Instrum. Methods Phys. Res. Sect. A-Accel. Spectrom. Dect. Assoc. Equip., **2007**, 580, 1526-1535.
37. M. Tromp, S. Russu, A.J. Dent, J.F.W. Mosselmans, J. Evans*, et al.*, A.I.P., **2007**, CP 882, 858-860.
38. N. Binsted, *X-Mult*. University of Southampton, Southampton, **2006**.

CHAPTER FIVE

BIMEVOX

Chapter Five: BiMeVOX

5.1 Crystal structure of BiMeVOX

The synthesis of α-$Bi_2VO_{5.5-\delta}$ at about 700 ºC has been reported to produce monoclinic Aurivillius-type crystal structure with space group A112, whereas the doping of the α-$Bi_2VO_{5.5-\delta}$ material by different metals (as Cu and Fe in these case) leads to the tetragonal Aurivillius type crystal structure with space group I4/mmm [1, 2]. In both γ-$Bi_2V_{1-x}Cu_xO_{5.5-(3x/2)-\delta}$ and γ-$Bi_2V_{1-x}Fe_xO_{5.5-x-\delta}$ solid phase structure the Cu^{2+} and the Fe^{3+} seems to directly replace V^{5+} in the Aurivillius structure [3, 4]. This structure consists of alternating layers of $[Bi_2O_2]^{2+}$ and $[VO_{3.5}Ĭ_{0.5}]^{2-}$, where Ĭ represents oxide ion vacancies. The $[Bi_2O_2]^{2+}$ layers have basal edge-shared BiO_4 square pyramidal groups with the oxygen atoms forming the basal plane and the bismuth in the apical position, with Bi-O bond lengths between 2.20 and 2.50 Å. Additional Bi-O interactions exist between the Bi^{3+} cations and the O atoms of the $VO_{3.5}$ sheets, which are characterized by two Bi-O distances of 2.70 Å and other two of 3.00 Å respectively. The vanadate layer in the idealized structure is made up of VO_6 octahedra which corner share in the equatorial plane, with four V-O bond lengths of 1.72 Å and two of 2.08 Å, Figure 1. This layer is distorted in the real structure of α-$Bi_2VO_{5.5-\delta}$ [5].

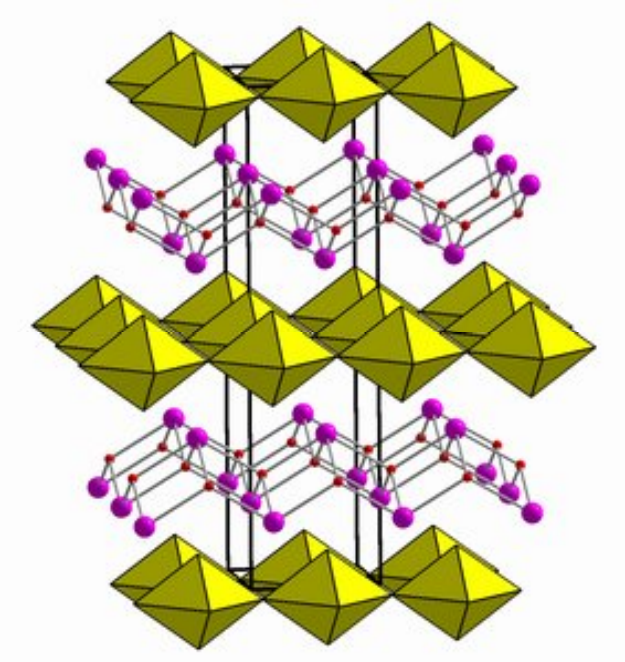

Figure 1 – The ideal crystal structure of tetragonal γ-BiMeVOX. Vanadium, copper, and iron octahedra yellow, bismuth atoms violet spheres, oxygen atoms red spheres

In this chapter synthesis and characterisation of sequential (one-by-one) and array BiMeVOX (with Me = Cu and Fe) materials will be described.

5.2 XRD Powder Diffraction of BiMeVOX

The X-ray powder diffraction patterns of sequential and array of both $Bi_2V_{1-x}Cu_xO_{5.5-(3x/2)-\delta}$ and $Bi_2V_{1-x}Fe_xO_{5.5-x-\delta}$ solid solutions synthesised by the sol-gel routes in the range of 0.00 ≤ x ≤ 0.25 and 0.00 ≤ x ≤ 0.35, respectively, are shown in Figures 2, 3, and 4.

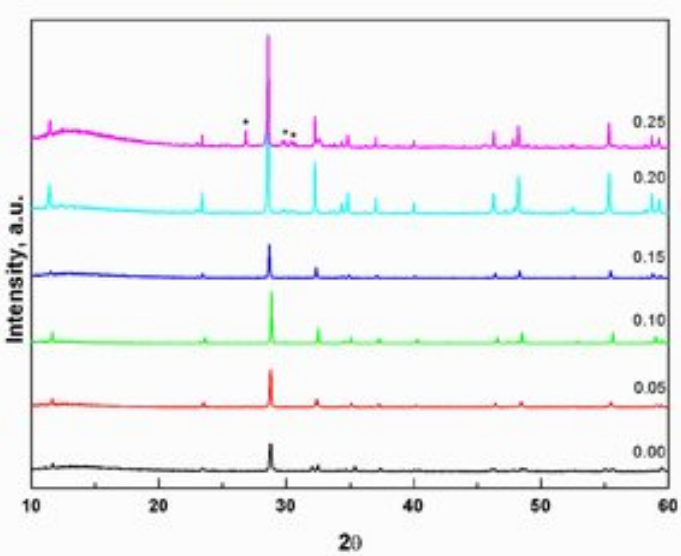

Figure 2 – The XRD powder diffraction data of $Bi_2V_{1-x}Cu_xO_{5.5-(3x/2)-\delta}$ ($0.00 \le x \le 0.25$) sequential materials synthesised by the sol-gel method, collected with the Siemens D5000 diffractometer (*=secondary phase)

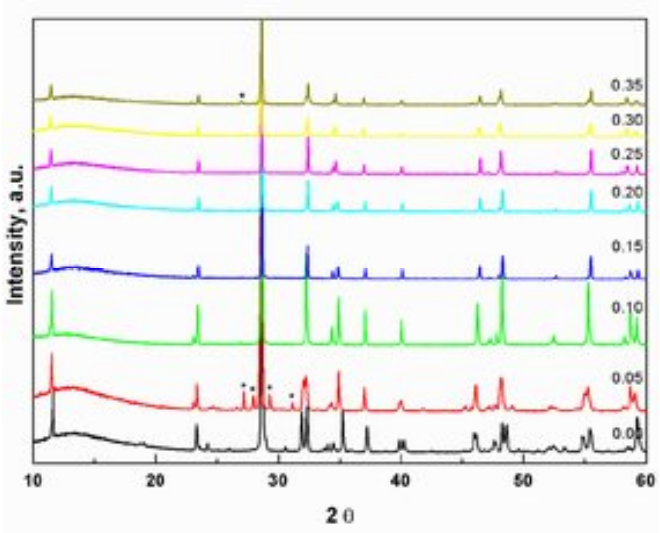

Figure 3 – The XRD powder diffraction data of $Bi_2V_{1-x}Fe_xO_{5.5-x-\delta}$ ($0.00 \le x \le 0.35$) sequential materials synthesised by the sol-gel method, collected with the Siemens D5000 diffractometer (*=secondary phase)

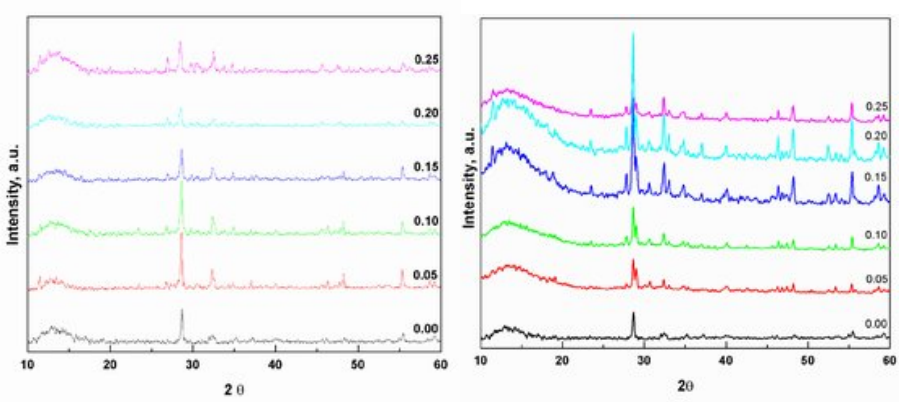

Figure 4 – The XRD powder diffraction data of $Bi_2V_{1-x}Cu_xO_{5.5-(3x/2)-\delta}$ ($0.00 \le x \le 0.25$, left) and γ-$Bi_2V_{1-x}Fe_xO_{5.5-x-\delta}$ □ ($0.00 \le x \le 0.25$, right) array materials synthesised by the peroxo sol-gel method, collected with the Siemens D5000 diffractometer

Lattice parameters of both the sol-gel sequential $Bi_2V_{1-x}Cu_xO_{5.5-(3x/2)-\delta}$ and $Bi_2V_{1-x}Fe_xO_{5.5-x-\delta}$□□ solid solutions were refined by the least-squares method using the program GSAS [6]. Data refinement of α-$Bi_2VO_{5.5-\delta}$, □and $Bi_2V_{1-x}Fe_xO_{5.5-x-\delta}$ □□with x = 0.05□□, $Bi_2V_{1-x}Cu_xO_{5.5-(3x/2)-\delta}$ with 0.05 Òx Ò0.25 and $Bi_2V_{1-x}Fe_xO_{5.5-x-\delta}$□□ with 0.10 Òx Ò0.35 obtained, respectively, the A112 and I4/*mmm* space group, displaying the α-phase monoclinic distortion. The upper limit of Cu solubility in the γ-phase is reached for Cu = 0.25 at which point a small amount of the secondary phases of Bi_2O_4 and $Cu_3Bi_4V_2O_{14}$ were identified; while the upper limit of Fe solubility in the γ-phase is reached for Fe = 0.35 at which point a small amount of $Bi_{3.5}V_{1.2}O_{8.25}$ was identified. As presented in Table 1 and Table 2, the lattice parameters and cell volume increase, even if not linearly, with increasing amount of copper and iron once the tetragonal phase is obtained. XRD data obtained for the BiCuVOX and BiFeVOX arrays, were good enough to display the tetragonal BiMeVOX crystal structure, although, not to display the changes in the crystal structures, i.e. phase transition and cell volume growth of the doped system.

The limit of Cu/Fe substitution into the V sites together with the thermodynamic stability of the tetragonal γ-phase over the monoclinic α-phase can be explained in terms of dopant-vacancy concentrations [7]. Krok *et al.* identified two principal coordination environments for V in these systems: tetrahedral and octahedral. In the α-phase, where the system shows only intrinsic vacancies, a 1:1 ratio of tetrahedra to octahedra is predicted. Once extrinsic vacancies are introduced through solid solution formation, the additional vacancies necessitate a lowering of vanadium coordination and hence an increase in the tetrahedral to octahedral ratio.

In the divalent substituted BiMeVOX for example, the theoretical limit of substitution occurs when all the V/M sites are tetrahedrally coordinated corresponding to x = 0.33 in the solid solution formula $Bi_2V_{1-x}Cu_xO_{5.5-(3x/2)-\delta}$. The theoretical limit can be lowered by the presence of a small amount of reduced vanadium (δ), as in the BiCuVOX system, down to x = 0.25. Previous neutron diffraction studies showed that vacancies are associated exclusively with the formation of tetrahedra in the vanadate layer; consequently the fraction of V/Me polyhedra in the vanadate layer which are tetrahedral is equal to the vacancy concentration per V/Me atom. The dopant-vacancy interaction appears to be critical in the order-disorder transition, and its concentrations contribute to the entropic term of the Gibbs free energy of the α and γ phases [8]. The entropic term can be expressed as:

$$\Delta S = R \ln(n_2/n_1)$$

Where R is the gas constant, and n_2 and n_1 the concentration of tetrahedral and octahedral site respectively. It is clear that upon Cu/Fe doping of the α-phase, the concentration of tetrahedral site will be higher then the octahedra site, stabilizing the γ-phase.

In particular the difference in the XRD patterns between the two vanadate polymorphs can be judged by the existence in the monoclinic α-$Bi_2VO_{5.5-\delta}$ XRD pattern, of a splitting of peaks at 32°, and 59° 2d. Furthermore, in the BiCuVOX materials, with increasing of Cu^{2+} concentration the XRD peak positions shift towards lower 2θ, reflecting the changes in d-spacing and consequent volume cell growth by incorporation of the copper ions into the BiCuVOX structure (Cu^{2+} = 0.57 Å, V^{5+} = 0.36 tetrahedral, and 0.54 octahedral Å radii) [9] , Figure 2. In the BiFeVOX materials both the XRD peak positions shift towards lower 2θ and the volume cell growth, with increasing of Fe^{3+} concentration, appear once the monoclinic to tetragonal phase transition is complete; these changes in d-spacing and cell volume may suggest the present of the Fe^{2+} species, being the Fe^{3+} smaller then V^{5+} (Fe^{2+} = 0.63 Å, Fe^{3+} = 0.49 Å, V^{5+} = 0.36 tetrahedral, and 0.54 octahedral Å radii) [9], Figure 3.

Table 1 - Lattice parameters of sequential $Bi_2V_{1-x}Cu_xO_{5.5-(3x/2)-\square}$ ($0.00 \leq x \leq 0.25$) sol-gel

Comp.	Crystal Struc.	Space Group	a (Å)	b (Å)	c (Å)	γ (°)	Cell Volume (Å)^3
x = 0.00	Monoc.	A 1 1 2	16.5611(2)	5.5946(6)	15.2325(8)	90.233(2)	352.8(2)
x = 0.05	Tetr.	I 4 /*mmm*	3.9199(3)	3.9199(3)	15.3766(15)	90	236.27(4)
x = 0.10	Tetr.	I 4 /*mmm*	3.9109(1)	3.9109(1)	15.4285(9)	90	235.71(2)
x = 0.15	Tetr.	I 4 /*mmm*	3.9141(2)	3.9141(2)	15.4282(9)	90	236.37(2)
x = 0.20	Tetr.	I 4 /*mmm*	3.9149(2)	3.9149(2)	15.4257(4)	90	236.42(1)
x = 0.25	Tetr.	I 4 /*mmm*	3.9179(2)	3.9179(2)	15.4399(8)	90	237.00(2)

Table 2 - Lattice parameters of sequential $Bi_2V_{1-x}Fe_xO_{5.5-x-\square}$ ($0.00 \leq x \leq 0.30$) sol-gel

Comp.	Crystal Struc.	Space Group	a (Å)	b (Å)	c (Å)	γ (°)	Cell Volume (Å)^3
x = 0.00	Monoc.	A 1 1 2	16.5611(2)	5.5946(6)	15.2325(8)	90.233(2)	352.8(2)
x = 0.05	Monoc.	A 1 1 2	16.6144(11)	5.5746(4)	15.3914(10)	90.124(8)	356.4(2)
x = 0.10	Tetr.	I 4 /*mmm*	3.9182(1)	3.9182(1)	15.4085(5)	90	236.51(1)
x = 0.15	Tetr.	I 4 /*mmm*	3.9119(1)	3.9119(1)	15.4442(5)	90	236.35(1)
x = 0.20	Tetr.	I 4 /*mmm*	3.9100(1)	3.9100(1)	15.4744(5)	90	236.57(1)
x = 0.25	Tetr.	I 4 /*mmm*	3.9085(1)	3.9085(1)	15.5316(5)	90	237.27(1)
x = 0.30	Tetr.	I 4 /*mmm*	3.9116(2)	3.9116(2)	15.5489(8)	90	237.91(2)

5.3 XAFS Spectroscopy of BiMeVOX

XAFS spectra of the V K edge, Figure 5, display an intense pre-edge feature at 5467 eV in the XANES region arising from a 1s to 3d dipole forbidden transition. The presence of this pre-edge feature is indicative of a tetrahedral environment of the x-ray-absorbing transition metal [10]. The multiple edge EXAFS analysis results for the BiMeVOX sequential sol-gel and array series are summarized in Table 3, 4 and 5. The V K edge EXAFS data of the BiCuVOX sequential materials have been analysed with two shells consisting of four and two oxygen bonded to the V, with V-O bond lengths between 1.71 and 1.72 Å for the first shell and between 2.08 and 2.13 Å for the second shell, Figure 6. The Cu-O bond lengths as obtained from the Cu K-edge EXAFS data, Figure 7, consist of a single shell of four Cu-O bonds, with values between 1.88 and 1.92 Å for the sequential and between 1.92 and 1.93 Å for the array samples, as expected, Table 3.

The Fe-O bond lengths as obtained from the Fe K-edge EXAFS data consist, as in the Cu case, of a single shell of four Fe-O bonds, with values between 1.97 and 2.00 Å for the sequential samples, as expected (Table 5).The Bi L_3 edge EXAFS data analyses, Figures 8 and 9, of both BiMeVOX materials, display four different shells consisting of two Bi-O each with bond lengths of ~2.23, ~2.48, ~2.77 and ~3.05 Å,

and another two shells consisting of four Bi-Bi and Bi-V with distances of ~3.72 Å and ~4.21 Å , respectively. These bond lengths, relative to the first four shells, become higher with the Cu/Fe doping, suggesting a distorted environment around Bi metal. The ideal V coordination is octahedral with corner sharing of the equatorial oxygens. Previous work showed that there was considerable disorder in the apical and equatorial oxygens with oxygens vacancies concentrated in the equatorial positions leading to two types of V coordination; the majority in distorted tetrahedra and remainder in distorted octahedra [11]. The EXAFS data analysis indicates that a structural model of the BiMeVOX structure must involve a vanadate layer built up from distorted V tetrahedra, distorted octahedra and a distorted four coordinated Cu/Fe site.

The Bi L_3 edge EXAFS data refinements of the BiCuVOX samples of the array, Table 4, display only one shell of oxygen bonded to the Bi with a bond length of about 2.19 Å. This is due to the lower quality data obtained on the inhomogeneously deposited materials on the array in fluorescence detection mode. In general the Cu-O bond lengths values calculated from the EXAFS BiCuVOX data array were similar to the EXAFS data of the sol-gel sequential materials, whereas the Bi-O bond lengths are slightly shorter.

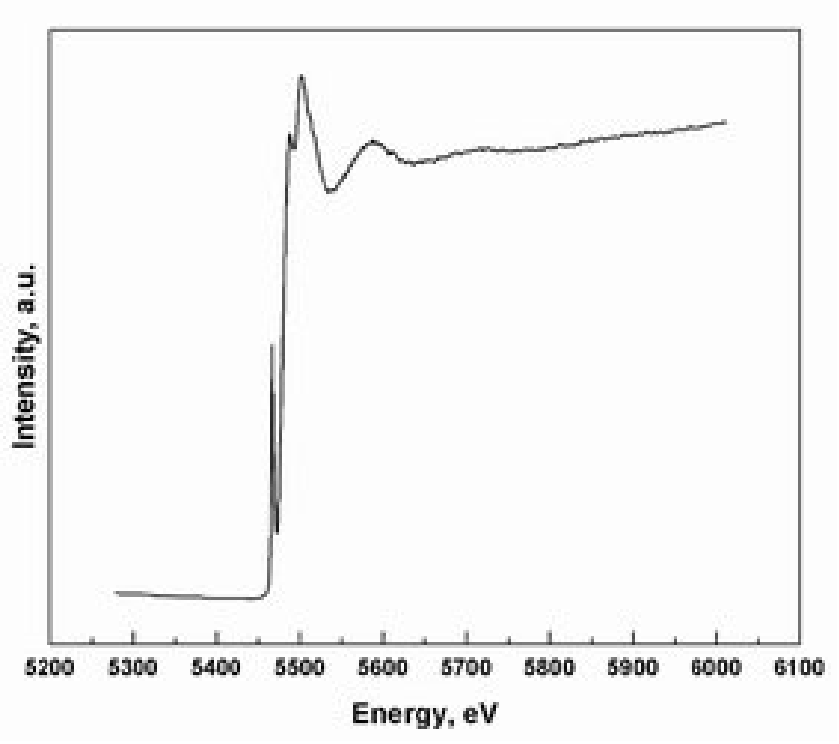

Figure 5 – The experimental raw V K XAFS data for the α-$Bi_2VO_{5.5-\delta}$ sequential sol-gel material

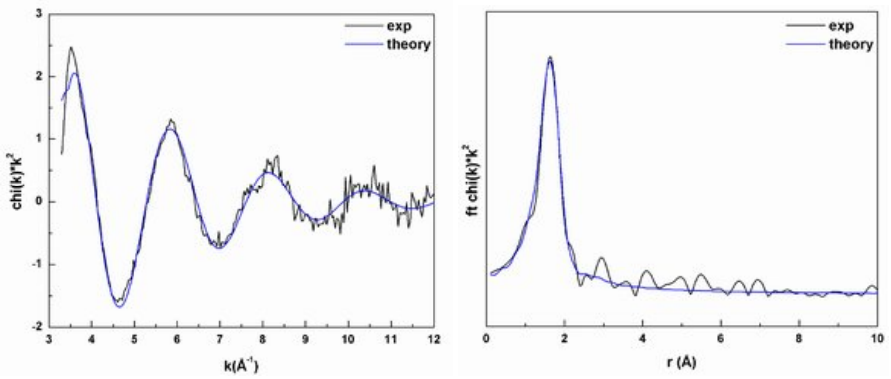

Figure 6 – The experimental raw and fitted k^2-weighted V K edge EXAFS (left) and Fourier transform (right) of the α-$Bi_2VO_{5.5-\delta}$ sequential sol-gel material

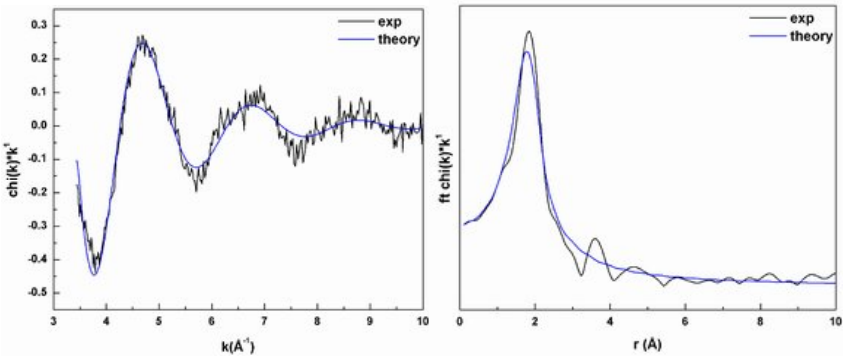

Figure 7 – The experimental raw and fitted k^1-weighted Cu K edge EXAFS (left) and Fourier transform (right) of the $Bi_2V_{1-x}Cu_xO_{5.5-(3x/2)-\delta}$ sequential sol-gel material (x = 0.15)

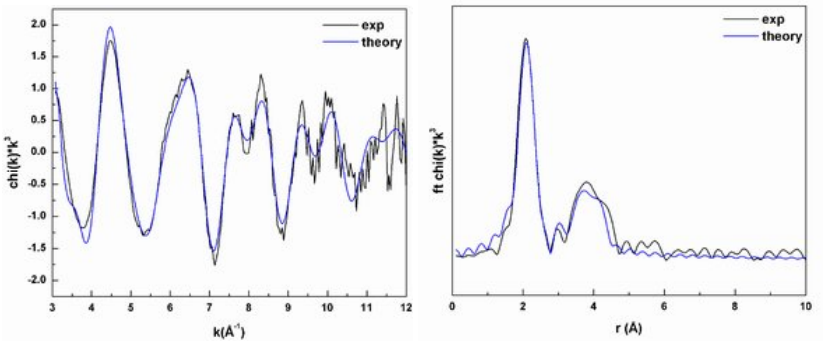

Figure 8 – The experimental raw and fitted k^3-weighted Bi L_3 edge EXAFS (left) and Fourier transform (right) of sequential sol gel monoclinic α-$Bi_2VO_{5.5-\delta}$

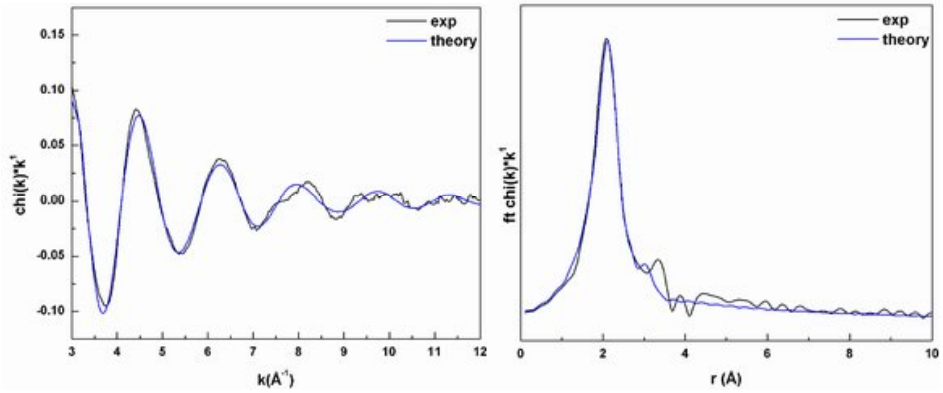

Figure 9 – The experimental raw and fitted k^1-weighted Bi L_3 edge XAFS (left) and Fourier transform (right) of the tetragonal $Bi_2V_{1-x}Cu_xO_{5.5-(3x/2)-\delta}$ sequential sol-gel material with x = 0.20

Table 3 - Bond length (Å) of sol-gel sequential $Bi_2V_{1-x}Cu_xO_{5.5-(3x/2)-\square\square}$ (0.00 ≤ x ≤ 0.20), calculated from the EXAFS both V and Cu K edge and Bi L_3 edge data analysis

Sample	V-O (s.g.)	V-O (s.g.)	Cu-O (s.g.)	Bi-O (s.g.)	Bi-O (s.g.)	Bi-O (s.g.)	Bi-O (s.g.)	Bi-Bi (s.g.)	Bi-V (s.g.)
	C.N.=4	2	4	2	2	2	2	4	4
0.00	1.71(1)	2.13(4)	-	2.22(1)	2.43(2)	2.71(2)	3.00(3)	3.72(1)	4.21(3)
0.05	1.72(1)	2.09(2)	1.89(1)	2.24(1)	2.52(2)	2.80(1)	3.09(5)	-	-
0.10	1.72(1)	2.08(2)	1.88(1)	2.24(1)	2.48(2)	2.76(1)	3.05(2)	-	-
0.15	1.72(1)	2.08(2)	1.90(1)	2.24(1)	2.49(1)	2.77(2)	3.06(2)	-	-
0.20	-	-	1.92(1)	2.23(1)	2.49(2)	2.78(2)	3.07(2)	-	-

(C.N. = coordination number)

Table 4 - Bond length (Å) of sol-gel array $Bi_2V_{1-x}Cu_xO_{5.5-(3x/2)-\square\square\square}$(0.00 ≤ x ≤ 0.20), calculated from the EXAFS both V and Cu K edge and Bi L_3 edge data analysis

Sample	Bi-O (array)	Cu-O (array)
	C.N.=1	4
0.00	2.19(2)	1.92(1)
0.05	2.19(2)	1.92(1)
0.10	2.19(2)	1.92(1)
0.15	2.20(2)	1.93(1)
0.20	2.19(2)	1.92(1)

(C.N. = coordination number)

Table 5 - Bond length (Å) of sol-gel sequential $Bi_2V_{1-x}Fe_xO_{5.5-x-\square}$ ($0.00 \leq x \leq 0.30$), calculated from the EXAFS Fe K edge and Bi L_3 edge data analysis

Sample	Fe-O (s.g.)	Bi-O (s.g.)	Bi-O (s.g.)	Bi-O (s.g.)	Bi-O (s.g.)	Bi-Bi (s.g.)	Bi-V (s.g.)
	C.N.=4	2	2	2	2	4	4
0.00	-	2.22(1)	2.43(2)	2.71(2)	3.00(3)	3.72(1)	4.21(3)
0.05	-	2.24(1)	2.48(1)	2.74(2)	3.04(2)	-	-
0.10	-	2.24(1)	2.48(1)	2.74(2)	3.05(2)	-	-
0.15	-	2.24(1)	2.50(2)	2.75(2)	3.06(2)	-	-
0.20	2.00(2)	2.24(1)	2.51(1)	2.77(2)	3.09(2)	-	-
0.25	1.97(2)	2.25(1)	2.47(2)	2.73(3)	3.03(3)	-	-
0.30	-	2.23(1)	2.47(1)	2.74(2)	3.03(3)	-	-

(C.N. = coordination number)

5.4 Raman Spectra of BiMeVOX

The oxygen atoms in both distorted octahedral and tetrahedral coordination around V form strongly bound molecular anions VO_6 and VO_4, which are bonded to Bi^{3+} cations in the lattice via relatively weak long-range ionic forces. Consequently modes within the VO_6 and VO_4 anions, internal modes, are stronger than those of external modes, corresponding to vibrations between lattice ions. The Raman spectra thus should mainly reflect the structure of the VO_6 and VO_4 octahedra and tetrahedra in the Aurivillius-type structure; however Hardcastle et al. showed that the so called site symmetry approach does not discriminate between tetrahedral and octahedral coordination of vanadium in vanadium oxides [12]. As consequence, as can be seen in the Figures 10, 11 and 12 displaying the sequential BiCuVOX and BiFeVOX sol-gel series and the $BiVO_4$ versus $Bi_2VO_{5.5}$ Raman spectra respectively, the BiMeVOX Raman spectra can be interpreted in terms of vanadate tetrahedra.

According to the site symmetry approach then, the Raman band at 922 cm^{-1} can be attributed to the stretching vibration mode of the V-O bond in a like-chain structure such as $(VO_3)_n^{n-}$ [13], while the Raman bands at 842 and 733 cm^{-1} are attributed to the ν_1 symmetric and ν_3 antisymmetric stretching modes of V-O bonds. The Raman features due to symmetric and asymmetric vibrations of V-O-V bridge are at 497 and 797 cm^{-1} respectively. The Raman band at 645 cm^{-1} is assigned to the asymmetric stretching vibration of the longer V-O bonds, suggesting a tetrahedral coordination for

V with two different V-O bond lengths [14, 15]. The intensity of the V-O symmetric mode decreases with decreasing amount of V in the structure.
The peaks at wavenumbers between 450 and 350 cm^{-1} are the bending motions or so-called ν_4 and ν_2 frequencies; while the peaks at wavenumbers lower then 350 cm^{-1} are due to the external modes (frustrated rotation/translation) [16]. The positions of both the stretching and bending motions shift with the increasing amount of Cu/Fe ions in the solid solution, suggesting the crystal structure changes with increasing amount of metal doping. This is consistent with the XRD and UV-visible results. The influence of the changes in the V-O bond lengths within the VO_4 tetrahedra is evident from the ν_1 modes as can be seen in Table 6 and 7: The ν_1 vibration shifts towards to higher energy, once the monoclinic to tetragonal phase transition occur. This phenomenon can be explained by the fact that after the phase transition from monoclinic α-$Bi_2VO_{5.5-\delta}$ phase to the tetragonal γ-BiMeVOX, the average V-O bond lengths become shorter once, upon Cu/Fe doping, the amount of tetrahedral group increase (with ideal average V-O value of 1.72 Å) respect the octahedral group (with ideal average V-O value of 1.86 Å) [17], increasing the ν_1 symmetric stretching mode energy.

As in the BiMoVOX materials case, an empirical expression to correlate the V-O bond lengths with the Raman stretching frequencies, using the Diatomic Approximation (no site symmetry) was utilised [12, 18]. In this approximation, in the α-$Bi_2VO_{5.5-\delta}$ phase the Raman band at about 922 cm^{-1} arises from stretches of a V-O bond with a bond length of 1.64 Å, whereas the Raman bands at about 842, 797, 733 and 645 cm^{-1} are due to stretches of distinct V-O bonds with bond lengths of 1.69, 1.71, 1.76 and 1.82 Å. These Raman bond distances become slightly shorter going through the series, indicating a reduction of the V-O bond lengths in the BiMeVOX doped system. The external modes refer to the relative motions, i.e. translation and rotation, of the $Bi_2O_2^{2+}$ and $VO_{3.5}^{2-}$ ions, since the BiMeVOX □lattice can be viewed as an intergrowth of alternating $VO_{3.5}$ perovskite-like sheets and Bi_2O_2 layers; in these frequency zone modes due to internal motion vibrations-chain bending can be also considered. Although it is difficult to assign the specific single frequencies to specific external vibration modes, both BiCuVOX and BiFeVOX external modes frequencies have similar values to values reported in investigations on BiMeVOX materials [13].

Due to the deep red colour of these BiMeVOX materials, Raman spectroscopy of the sequential samples has been performed using a Raman spectrometer with a higher energy excitation laser (633 nm), if compared with the excitation energies employed in the analysis of the BiMoVOX and Pyrovanadate materials (785 nm). Unfortunately, this high energy Raman spectrometer could not be used for high-throughput characterisation; therefore it has been not possible to collect Raman spectra of the BiMeVOX arrays materials.

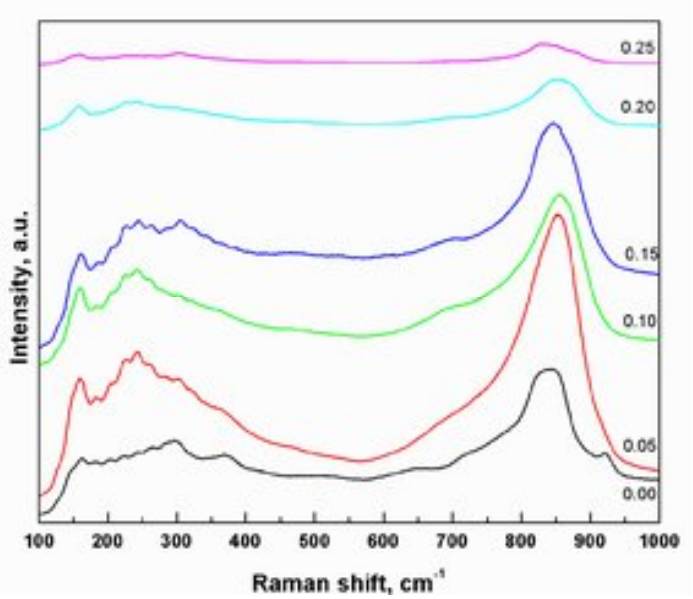

Figure 10 – Raman spectra of $Bi_2V_{1-x}Cu_xO_{5.5-(3x/2)-\delta}$ ($0.00 \leq x \leq 0.25$) sequential series made by the peroxo sol-gel method

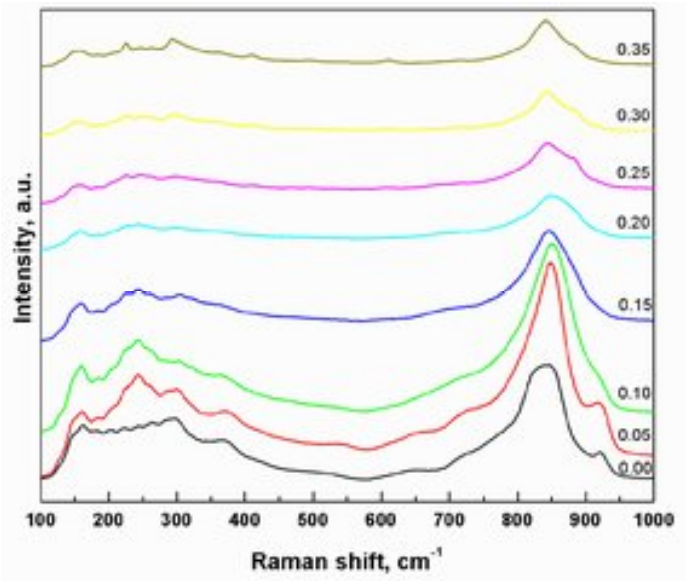

Figure 11 – Raman spectra of $Bi_2V_{1-x}Fe_xO_{5.5-x-\delta}$ ($0.00 \leq x \leq 0.35$) sequentially made series by the peroxo sol-gel method

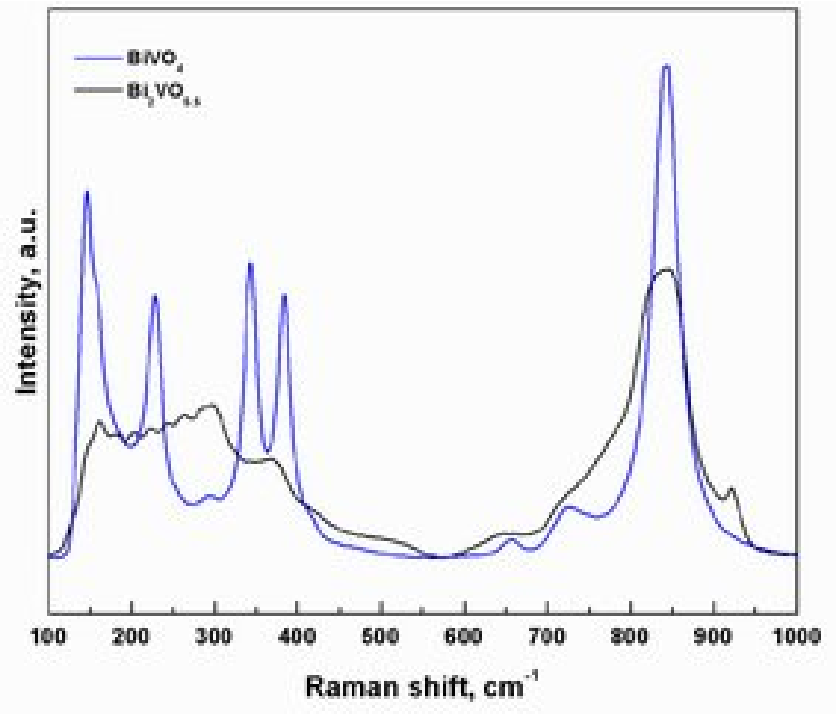

Figure 12 – Raman spectra of both monoclinic $BiVO_4$ (blue) and α-$Bi_2VO_{5.5-\delta\square}$ (black) made by the peroxo sol-gel method

Table 6 - Results of the Raman spectral analysis (cm^{-1}) of sequential $Bi_2V_{1-x}Cu_xO_{5.5-(3x/2)-\delta\square}$ ($0.00 \leq x \leq 0.25$) sol-gel

Vibr. mode	0.00	0.05	0.10	0.15	0.20	0.25
ν_s $(VO_3)_n^{n-}$	922	-	-	-	-	-
ν_s (V-O) FWHM	842 61	854 62	865 50	860 57	867 53	853 65
ν_{as} (V-O-V)	797	807	830	830	836	825
ν_s (V-O)	733	744	780	789	793	789
ν_{as} (V-O)	645	688	700	702	704	721

Where: ν_s = symmetric stretching mode, ν_{as} = asymmetric stretching mode, δ_s = bending mode and δ_{as} = antisymmetric bending mode (out-of-plane)

Table 7 - Results of the Raman spectral analysis (cm^{-1}) of sequential $Bi_2V_{1-x}Fe_xO_{5.5-x-\delta\square}$ ($0.00 \leq x \leq 0.25$) sol-gel

Vibr. mode	0.00	0.05	0.10	0.15	0.20	0.25	0.30
ν_s $(VO_3)_n^{n-}$	922	920	910	-	-	-	-
ν_s (V-O) FWHM	842 61	847 55	851 66	851 66	855 65	852 64	846 62
ν_{as} (V-O-V)	797	800	801	806	810	818	-
ν_s (V-O)	733	737	733	713	715	709	714
ν_{as} (V-O)	645	654	676	604	-	605	610

Where: ν_s = symmetric stretching mode, ν_{as} = asymmetric stretching mode, δ_s = bending mode and δ_{as} = antisymmetric bending mode (out-of-plane)

5.5 UV-visible Diffuse Reflectance Spectra and SEM of BiMeVOX

UV-visible spectra of the BiMeVOX materials made by the sol-gel method are shown in Figure 13 and 14. The $Bi_2V_{1-x}Cu_xO_{5.5-(3x/2)-\delta}$ □materials were monotonically blue-shifted together with the amount of Cu doping, Figure 13 (left), whereas the $Bi_2V_{1-x}Fe_xO_{5.5-x-\delta}$ □□materilas were generally blue-shifted respect the pure α-$Bi_2VO_{5.5-\delta}$□□ but not monotonically with the amount of Fe doping, Figure 14 (left). These results, displaying only a single optical edge for each sample, indicate that the powders obtained were homogeneous solid-solutions, rather then a mixture of vanadium and copper or iron oxides. The optical trends are clearly visible in Figures 13 (right) and Figure 14 (right) in which the band gaps of both BiCuVOX and BiFeVOX materials made by the sol-gel method are shown.

Two effects need to be taken into account to explain the colour properties observed: (1) The contribution of both the Cu^{2+} and the Fe^{3+} ions to the overall electronic conduction bands of the BiMeVOX materials, and (2) the oxygen stoichiometry.

The valence bands of both pure α-$Bi_2VO_{5.5-\delta}$ and γ-BiMeVOX are mainly composed by hybridisation of the Bi 6s and O 2p orbitals, while the V 3d in α-$Bi_2VO_{5.5-\delta}$ and the mixed V 3d and Cu 3d orbitals in the BiCuVOX, and the mixed V 3d and Fe 3d orbitals in the BiFeVOX mainly contribute to form the bottom of the conduction band [19], Figure 15. Since, the effective electronegativity of the V^{5+} (2.49) ion is higher than both the Cu^{2+} (2.21) and Fe^{3+} (2.33) ion, copper and iron doping resulted in an increase of the band gap value of the electronic transition [20, 21].

Abrahams et al. showed that both colour intensities and properties of α-$Bi_2VO_{5.5-\delta}$, and consequently of γ-BiMeVOX□, are strongly influenced by the method of preparation [5, 22]. Synthesis of α-$Bi_2VO_{5.5-\delta}$□ by slow cooling in oxygen or air atmosphere yields to products which are visually different in colour. These colour changes are likely to be due to differences in the electronic structure caused by differing amounts of V^{4+}; the effect of reduction of V is to increase the total number of

oxide vacancies and hence, as in the BiMoVOX materials made by calcinations in air atmosphere case, narrowing the band gap value.

Since the smaller difference in electronegativity between the V^{5+} and the Fe^{3+}, compared to that between the V^{5+} and the Cu^{2+}, this effect can be responsible of the small and at the same time non-linear increase of the band gap values in the BiFeVOX materials.

SEM pictures of BiMeVOX materials show, as in the BiMoVOX materials synthesised by the sol-gel method, that they have particles with an irregular-smooth shape and size in a range of 1 ï 10 μm, Figure 16.

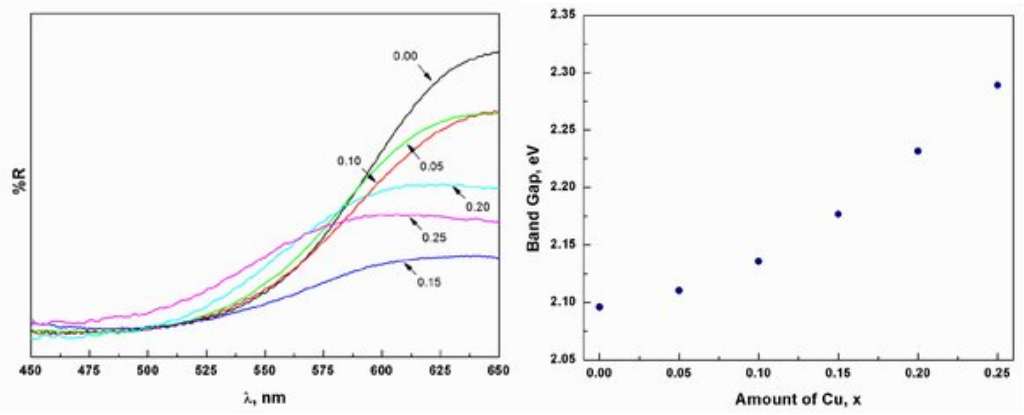

Figure 13 – UV-visible reflectance spectra (left) and band gap energies (right) of $Bi_2V_{1-x}Cu_xO_{5.5-(3x/2)-\delta}$ ($0.00 \leq x \leq 0.25$) materials made by the peroxo sol-gel method

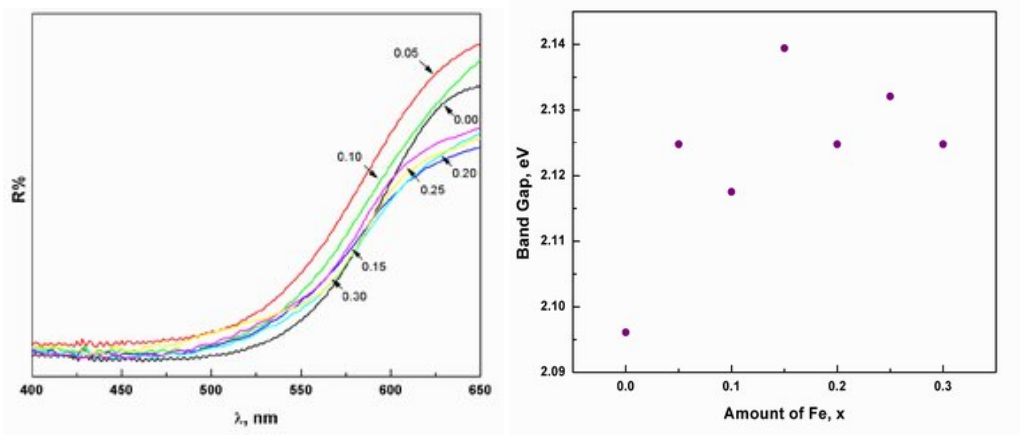

Figure 14 – UV-visible reflectance spectra (left) and band gap energies (right) of $Bi_2V_{1-x}Fe_xO_{5.5-x-\delta}$ ($0.00 \leq x \leq 0.30$) materials made by the peroxo sol-gel method

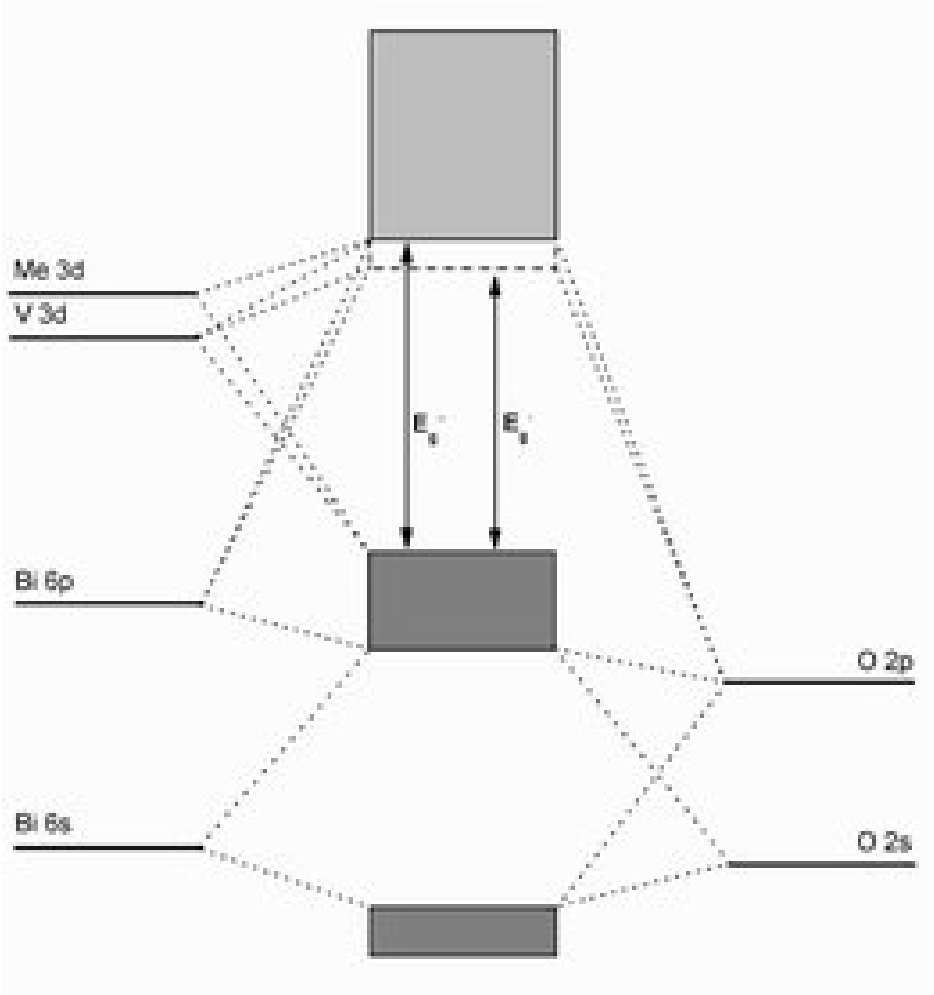

Figure 15 – Schematic molecular orbital diagram of the sequential BiMeVOX materials, Me = Cu or Fe; E_g' = band gap of monoclinic $Bi_2VO_{5.5-\delta}$ and E_g" = band gap of tetragonal BiMeVOX

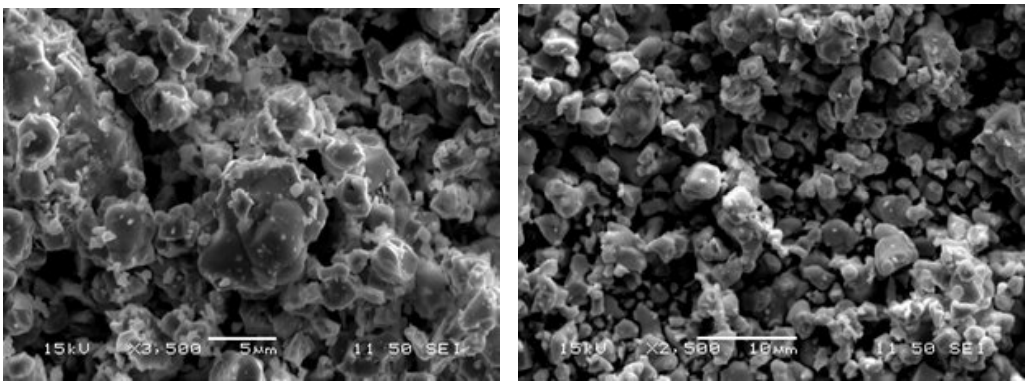

Figure 16 – SEM photographs of BiCuVOX (left) and BiFeVOX (right) materials made by the peroxo sol-gel method

5.6 Conclusions

The synthesis of α-$Bi_2VO_{5.5-\delta\square}$ at temperatures around 700°C produced monoclinic Aurivillius type crystal structure. A combined characterization approach of complementary techniques, i.e. XRD powder diffraction, Raman and XAFS spectroscopy reveals that, both the Cu^{2+} and Fe^{3+} doping of monoclinic α-$Bi_2VO_{5.5-\delta}$ leads to tetragonal γ-$Bi_2V_{1-x}Cu_xO_{5.5-(3x/2)-\delta}$ and γ-$Bi_2V_{1-x}Fe_xO_{5.5-x-\delta}$ Aurivillius type crystal structure.

The BiCuVOX materials can be considered as potential new class of inorganic pigments, whereas the BiFeVOX materials due to the presence of factors such as oxygens vacancies, or relative small difference in effective electronegativity between the doping and the replaced cations, the band gap energy values do not change consistently together with the amount of metals doping.

Arrays of vanadium copper, or vanadium iron, mixed metal oxide compounds are prepared in a high-throughput manner, with the peroxo sol-gel route, using robotic methodologies. These arrays can successfully be analysed for their structural and compositional properties (XRD and XAFS) in a rapid manner providing an increase in efficiency compared to one-at-a-time experiments. Raman analysis of both BiCuVOX, and BiFeVOX arrays did not display any characteristic stretching modes of the vanadate tetrahedra.

5.7 Experimental Section

5.7.1 Preparation of BiMeVOX Sequential Materials

A peroxo sol-gel method of synthesis have been utilised to obtain both the BiFeVOX and BiCuVOX materials:

Peroxo sol-gel synthesis:

Sol-gel specimens were prepared by peroxo sol-gel route. In a typical sequential BiCuVOX peroxo sol-gel synthesis, bismuth nitrate solutions were prepared dissolving 2.00 g of $Bi(NO_3)_3{\cdot}5H_2O$ (98%, Alfa Aesar) in nitric acid (2M). Precursor

vanadium, and copper solutions were prepared separately, from 0.22 g of NH_4VO_3 (99%, Alfa Aesar) dissolved in H_2O_2(30%)/H_2O (1:1), and 0.05 g of $Cu(NO_3)_2 \cdot 3H_2O$ (98%, Alfa Aesar) both dissolved in H_2O. The two peroxide solutions, vanadium and copper, were then added together and stirred for 30 min. Whereas in a typical sequential BiFeVOX peroxo sol-gel synthesis, bismuth nitrate solutions were prepared dissolving 1.2 g of $Bi(NO_3)_3 \cdot 5H_2O$ (98%, Alfa Aesar) in nitric acid (2M). Precursor vanadium, and iron solutions were prepared separately, from 0.13 g of NH_4VO_3 (99%, Alfa Aesar) dissolved in H_2O_2(30%)/H_2O (1:1), and 0.05 g of $Fe(NO_3)_3 \cdot 9H_2O$ (98%, Alfa Aesar) dissolved in H_2O. The two peroxide solutions, vanadium and iron, were then added together and stirred for 30 min.
Finally the bismuth solutions were added drop-wise to the vanadium-copper or to the vanadium-iron solutions for half an hour, while stirring was continued for a further 2 h. The mixed solutions were heated up to 120 °C in air until evaporation of the solvent was completed, after which the red-brown precipitate was heated to 700 °C for 24 h in an O_2 atmosphere, with a temperature gradient of 0.5 °C/min.

5.7.2 Preparation of BiMeVOX Arrays

Arrays of BiMeVOX materials were prepared by peroxo sol-gel route, from solutions of the metal nitrates or ammoniates (about 0.5 M) in diluted nitric acid or hydrogen peroxide in water (1:1) and water. In a typical peroxo sol-gel BiCuVOX array synthesis bismuth nitrate solutions were prepared dissolving 1.73 g of $Bi(NO_3)_3 \cdot 5H_2O$ (98%, Alfa Aesar) in 7 ml of nitric acid (2M). Precursor vanadium, and copper solutions were prepared separately, from 0.30 g of NH_4VO_3 (99%, Alfa Aesar) dissolved in 3 ml of H_2O and 2 ml of H_2O_2(30%), and 0.05 g of $Cu(NO_3)_2 \cdot 3H_2O$ (98%, Alfa Aesar) dissolved in 5 ml of H_2O. Whereas in a typical peroxo sol-gel BiFeVOX array synthesis bismuth nitrate solutions were prepared dissolving 1.74 g of $Bi(NO_3)_3 \cdot 5H_2O$ (98%, Alfa Aesar) in 7 ml of nitric acid (2M). Precursor vanadium, and iron solutions were prepared separately, from 0.30 g of NH_4VO_3 (99%, Alfa Aesar) dissolved in 3 ml of H_2O and 2 ml of H_2O_2(30%), and 1.03 g of $Fe(NO_3)_3 \cdot 9H_2O$ (98%, Alfa Aesar) dissolved in 5 ml of H_2O.
These were dispensed into a standard 54 well plate (reusable Teflon mask system, with a 6 x 9 grid of 5 mm sized holes, pressed on an alumina tile by stainless steel plates) in the appropriate ratios and mixed using a Packard Multiprobe II robot. Then the array was left for 12 hours at ambient temperature in air atmosphere, and after that, the solvent was evaporated at 60 °C overnight in an oven in air

atmosphere before the alumina tile was fired up to 700 °C in a furnace in oxygen atmosphere for 24 h.

5.7.3 XRD Powder diffraction

Diffraction patterns were obtained using a Siemens D5000 (Cu $K_{\alpha 1}$ radiation, λ = 1.5406 Å) for both the sequential and arrays series. The phases were identified by comparison with the PDF2 database [41]. Data refinement of the sequential materials was performed using the GSAS program.

5.7.4 XAS spectroscopy

XAS spectroscopy studies were carried out at the Daresbury Laboratory (Daresbury, U.K.) and at the Hamburger Synchrotronstrahlungslabor (HASYLAB) at Deutsches Elektronen-Synchrotron (DESY).

The Bi L_3 (13419 eV), Cu K (8979 eV), and V K (5465 eV) edge XAS studies were performed at station 9.3 and 7.1 of the SRS using a Si(111) double crystal monochromator, respectively. Data were collected using a 13 element Ge solid state detector. The Bi L_3 edge of the sequential samples (diluted up to 1 wt% in metal) was collected in transmission mode.
Cu K edge (5465 eV) and Fe K edge (7112 eV) of the sequential samples were collected at the X1 beamline of the Hamburger Synchrotronstrahlungslabor (HASYLAB) at Deutsches Elektronen-Synchrotron (DESY). In both cases the data were obtained with a Si(111) double crystal monochromator with a 13 element Ge solid state detector. Pt foil (L_2 edge = 13273 eV) was used for the calibration of the Bi L_3 edge, with V, Cu, and Fe foils for the calibration of V, Cu, and Fe K edges. Data were acquired with a σk of 0.04 $Å^{-1}$ and a data acquisition time of 20 min. per scan. The sequential samples were mounted in a self supporting sample holder. All samples were characterized in the HTP chamber, allowing combined XAS, XRD and Raman [23].

EXAFS data analysis of both sequential and array materials were performed using the *X-Mult* and *Excurve(9.301)* programs [24, 25].

5.7.5 UV/Vis and Raman diffuse reflectance

Absorption measurements of the sequential samples were performed using a Perkin Elmer Lambda 35 UV/vis spectrometer in diffuse reflectance mode. Spectra were collected in the visible range of 380 ï 780 nm. The band gaps energy values are calculated from the maximum of the first derivative of the absorption edges. Raman spectra of both bulk and array samples were collected with an optical fibre Renishaw RM 2000 Spectrometer, using high-power HeNe laser (633 nm) with a resolution of 3 cm^{-1} in the range between 100 and 1000 cm^{-1}. Spectra were calibrated using the 520.5 cm^{-1} line of a silicon wafer.

5.7.6 Electron Microscopy

Transmission Electron Microscopy data were collected using a JEM 3010 transmission electron microscope.

Scanning Electron Microscopy data were collected using a JSM 5910 scanning electron microscope. Images of each spot were taken at 2000x magnification with a spot size of 21, accelerating voltage of 15 kV.

5.8 References

1. G. Mairesse, P. Roussel, R.N. Vannier, M. Anne, and G. Nowogrocki, Sol. St. Sci., **2003**, 5, 861-869.
2. G. Mairesse, P. Roussel, R.N. Vannier, M. Anne, C. Pirovano*, et al.*, Sol. St. Sci., **2003**, 5, 851-859.
3. C.K. Lee and A.R. West, Sol. St. Ion., **1996**, 86-88, 235-239.
4. O. Joubert, M. Ganne, R.N. Vannier, and G. Mairesse, Sol. St. Ion., **1996**, 83, 199-207.
5. I. Abrahams, A.J. Bush, F. Krok, G.E. Hawkes, K.D. Sales*, et al.*, J. Mater. Chem., **1998**, 8, 1213-1217.
6. A.C. Larson and R.B. Von Dreele, *Generalised Structure Analysis System*, Los Alamos National Laboratory, Los Alamos, **2004**.
7. F. Krok, I. Abrahams, W. Wrobel, S.C.M. Chan, M. Malys*, et al.*, Sol. St. Ion., **2002**, 154, 511-516.
8. A.R. West, ed. *Solid State chemistry and its Applicaiton*. 1987, Wiley. 449-450.
9. R.D. Shannon, Acta Crystallogr. Sect. A, **1976**, 32, 751-767.
10. J. Wong, F.W. Lytle, R.P. Messmer, and D.H. Maylotte, Phys. Rev. B, **1984**, 30, 5596-5610.
11. A.V. Chadwick, C. Colli, C. Maltese, G. Morrison, I. Abrahams*, et al.*, Sol. St. Ion., **1999**, 119, 79-84.
12. F.D. Hardcastle and I.E. Wachs, J. Phys. Chem., **1991**, 95, 5031-5041.
13. R. Bacewicz and P. Kurek, Sol. St. Ion., **2000**, 127, 151-156.
14. R.L. Frost, D.A. Henry, M.L. Weier, and W. Martens, J. Raman Spectrosc., **2006**, 37, 722-732.
15. J.Q. Yu and A. Kudo, Adv. Funct. Mater., **2006**, 16, 2163-2169.
16. C.C. Santos, E.N. Silva, A.P. Ayala, I. Guedes, P.S. Pizani*, et al.*, J. Appl. Phys., **2007**, 101, 053511(1-5).
17. M. Schindler, F.C. Hawthorne, and W.H. Baur, Chem. Mat., **2000**, 12, 1248-1259.
18. F.D. Hardcastle and I.E. Wachs, J. Raman Spectrosc., **1990**, 21, 683-691.
19. V.M. Zainullina, V.M. Zhukovskii, E.S. Buyanova, and Y.V. Emel'yanova, Russ. J. Inorg. Chem., **2007**, 52, 225-232.
20. R.T. Sanderson, J. Chem. Educ., **1988**, 65, 112-118.
21. R.T. Sanderson, J. Chem. Educ., **1988**, 65, 227-231.
22. I. Abrahams and F. Krok, Sol. St. Ion., **2003**, 157, 139-145.

23. M. Tromp, S. Russu, A.J. Dent, J.F.W. Mosselmans, J. Evans*, et al.*, A.I.P., **2007**, CP 882, 858-860.
24. N. Binsted, *X-Mult*. University of Southampton, Southampton, **2006**.
25. N. Binsted, *EXCURV(9.301)*. CCLRC Daresbury Laboratory Computer program, **1998**.

CHAPTER SIX

PYROVANADATES

Chapter Six: Pyrovanadates

6.1 Crystal structure of $(Ca,Me)_2V_2O_7$

The synthesis of both $Ca_2V_2O_7$ and $(Ca_{2-x},Me_x)V_2O_7$, with Me = Pb^{2+}, Cd^{2+} and Sr^{2+}, at temperatures above 700°C has been reported to produce a triclinic pyrovanadate type crystal structure with space group P-1 [1]. In the $(Ca_{2-x},Me_x)V_2O_7$ solid phase structure the Me^{2+} seems to directly replace Ca^{2+} in the pyrovanadate structure. In this structure the V atom polyhedra form tetrameric chains, with two VO_4 tetrahedra at the end and two middle edge-sharing VO_5 distorted square pyramids, Figure 1. The Ca, and Me in the doped systems, cations are found between the tetramer, in two different coordination sites, holding them together. Both the Ca are 7-coordinated with O atom, the first with Ca-O bond length between 2.27 and 2.47 Å, and the second with bond length ranging from 2.32 to 2.93 Å [2].

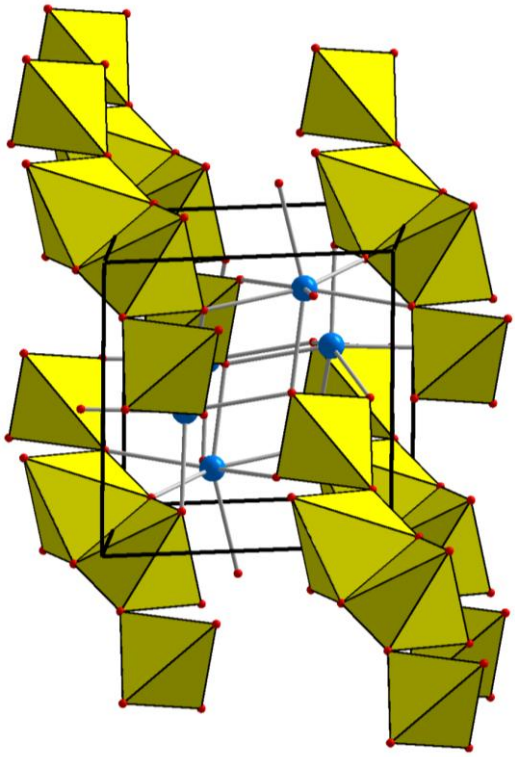

Figure 1 – The triclinic crystal structure of $Ca_2V_2O_7$. Vanadium polyhedra yellow, calcium, lead, strontium and cadmium atoms blue spheres. Oxygen atoms red spheres

In this chapter synthesis and characterisation of sequential (one-by-one) and array $(Ca_{2-x},Me_x)V_2O_7$ (with Me = Pb, Cd, and Sr) materials will be described.

6.2 XRD Powder Diffraction of $(Ca,Me)_2V_2O_7$

The X-ray powder diffraction patterns of sequential $(Ca_{2-x},Pb_x)V_2O_7$ solid solutions synthesised by the sol-gel routes, in the range of $0.00 \leq x \leq 0.40$, are shown in Figures 2. Figure 3 displays XRD data of the $(Ca_{2-x},Pb_x)V_2O_7$ array collected with a Siemens D5000 Diffractometer.

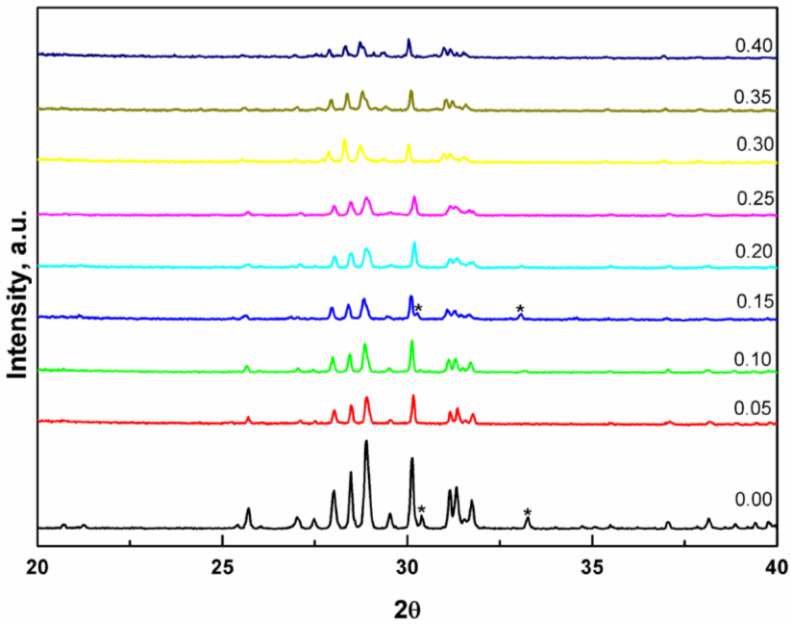

Figure 2 – The XRD powder diffraction data of $(Ca_{2-x},Pb_x)V_2O_7$ ($0.00 \leq x \leq 0.40$) sequential materials synthesised by the sol-gel method, collected with the Siemens D5000 diffractometer (*=secondary phase)

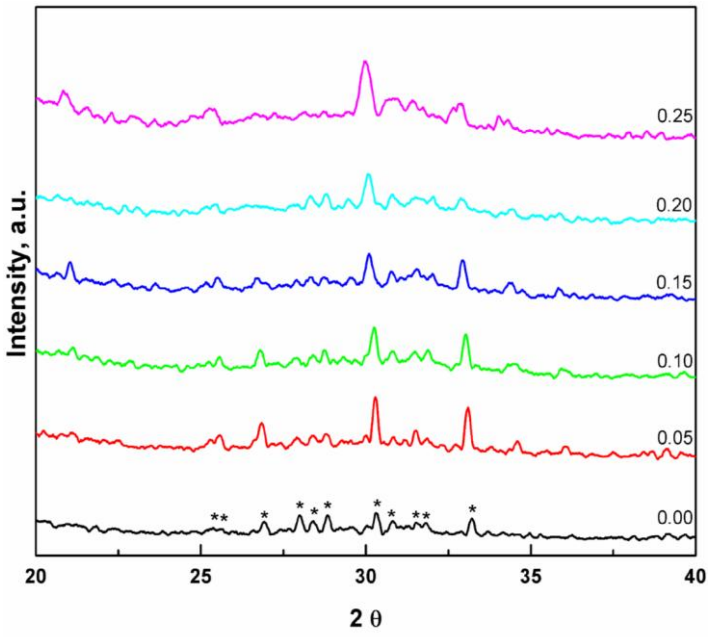

Figure 3 – The XRD powder diffraction data of the $(Ca_{2-x},Pb_x)V_2O_7$ ($0.00 \leq x \leq 0.25$) array synthesised by the peroxo sol-gel method, collected with the Siemens D5000 diffractometer (*= triclinic $Ca_2V_2O_7$ phase)

Lattice parameters of the sequential sol-gel $(Ca_{2-x},Me_x)V_2O_7$ solid solutions were refined by the least-squares method using the program GSAS [3]. Data refinement of $(Ca_{2-x},Me_x)V_2O_7$ with $0.00 \leq x_{Pb} \leq 0.40$, $0.00 \leq x_{Cd} \leq 0.30$ and $0.00 \leq x_{Sr} \leq 0.30$ resulted in the space group P-1. Sequential $Ca_2V_2O_7$ and $(Ca_{1.85},Pb_{0.15})V_2O_7$ display a small amount of rhombohedral $Ca_3(VO_4)_2$ crystal phase with space group R3c, Figure 2. As presented in Table 1, Table 2 and Table 3 the lattice parameters and the cell volume of the doped systems increase with increasing amount of both lead and strontium, while they slightly decrease with increasing amount of cadmium. These changes, in the cell volume of the pyrovanadate doped systems, were expected in consideration of the relative effective ionic radii of the different doping metals, with a coordination number of 7, compared with the calcium ionic radii, Table 4 [4]. The XRD data obtained for the $(Ca_{2-x},Me_x)V_2O_7$ array using a D5000 diffractometer, Figure 3, were good enough to display the triclinic $(Ca_{2-x},Pb_x)V_2O_7$ crystal structures, no full refinement of the data was possible.

Table 1 - Lattice parameters of sequential $(Ca_{2-x},Pb_2)V_2O_7$ ($0.00 \leq x \leq 0.40$)

Comp.	a (Å)	b (Å)	c (Å)	α (°)	β (°)	γ (°)	Cell Volume (Å)^3
x = 0.00	6.6635(4)	6.9209(4)	7.0143(4)	86.488(4)	63.864(3)	83.719(4)	288.63(3)
x = 0.05	6.6509(4)	6.9104(4)	7.0051(5)	86.483(4)	63.835(3)	83.704(4)	287.19(3)
x = 0.10	6.6548(7)	6.9141(7)	7.0103(8)	86.527(6)	63.812(5)	83.743(6)	287.70(5)
x = 0.15	6.6550(8)	6.9214(8)	7.0161(8)	86.589(6)	63.820(5)	83.767(6)	288.28(6)
x = 0.20	6.6596(7)	6.9290(7)	7.0241(8)	86.602(6)	63.816(4)	83.766(6)	289.12(5)
x = 0.25	6.6602(7)	6.9322(7)	7.0257(8)	86.658(6)	63.814(5)	83.811(6)	289.37(6)
x = 0.30	6.6596(7)	6.9332(7)	7.0275(7)	86.686(5)	63.805(4)	83.834(5)	289.45(5)
x = 0.35	6.6640(5)	6.9383(5)	7.0332(6)	86.702(4)	63.789(4)	83.844(4)	290.06(4)
x = 0.40	6.6638(8)	6.9362(8)	7.0320(8)	86.684(7)	63.787(6)	83.848(7)	289.89(6)

Table 2 - Lattice parameters of sequential $(Ca_{2-x},Cd_2)V_2O_7$ ($0.00 \leq x \leq 0.30$)

Comp.	a (Å)	b (Å)	c (Å)	α (°)	β (°)	γ (°)	Cell Volume (Å)^3
x = 0.05	6.6458(5)	6.9029(5)	6.9972(5)	86.347(4)	63.842(4)	83.574(4)	286.27(4)
x = 0.10	6.6465(6)	6.9045(6)	6.9990(6)	86.346(5)	63.841(4)	83.569(5)	286.44(4)
x = 0.15	6.6445(6)	6.9057(6)	6.9976(7)	86.247(5)	63.822(4)	83.465(5)	288.24(5)
x = 0.20	6.6432(7)	6.9078(6)	6.9982(7)	86.155(6)	63.809(4)	83.349(5)	286.19(5)
x = 0.25	6.6423(6)	6.9059(6)	6.9980(7)	86.696(6)	63.795(5)	83.160(5)	285.90(5)
x = 0.30	6.6407(7)	6.9055(7)	6.9973(8)	86.875(6)	63.785(5)	83.054(6)	285.70(5)

Table 3 - Lattice parameters of sequential $(Ca_{2-x},Sr_2)V_2O_7$ ($0.00 \leq x \leq 0.30$)

Comp.	a (Å)	b (Å)	c (Å)	α (°)	β (°)	γ (°)	Cell Volume (Å)^3
x = 0.05	6.6514(5)	6.9087(5)	7.0039(5)	86.512(4)	63.860(4)	83.723(4)	287.17(4)
x = 0.10	6.6426(7)	6.9015(7)	6.9968(8)	86.605(6)	63.854(5)	83.773(6)	286.22(5)
x = 0.15	6.6565(4)	6.9167(4)	7.0137(4)	86.677(3)	63.844(3)	83.818(3)	288.14(3)
x = 0.20	6.6549(6)	6.9196(6)	7.0122(6)	86.698(5)	63.846(4)	83.825(5)	288.03(4)
x = 0.25	6.6589(5)	6.9205(5)	7.0172(6)	86.693(4)	63.855(4)	83.839(4)	288.59(4)
x = 0.30	6.6556(8)	6.9179(8)	7.0136(9)	86.686(7)	63.837(6)	83.811(7)	288.13(6)

Table 4 - Effective ionic radii

ION	E.C.	C.N.	I.R. (Å)
Ca^{2+}	$3p^6$	VI	1.00
		VII	1.06
		VIII	1.12
Pb^{2+}	$6s^2$	VI	1.19
		VII	1.23
		VIII	1.29
Cd^{2+}	$4d^{10}$	VI	0.95
		VII	1.03
		VIII	1.10
Sr^{2+}	$4p^6$	VI	1.18
		VII	1.21
		VIII	1.26

E.C. electronic configuration, C.N. coordination number, I.R. effective ionic radii

6.3 XAFS Spectroscopy of $(Ca,Me)_2V_2O_7$

XAFS spectra of the V K edge, Figure 4, display an intense pre-edge feature at 5470 eV in the XANES region arising from 1s to 3d dipole forbidden transitions. The presence of this pre-edge feature is indicative of p-d hybridization typical of a tetrahedral environment for the x-ray-absorbing transition metal [5, 6]. The multiple edge EXAFS analysis using the program *Excurve* [7], results for the sequential and array sol-gel series are summarized in Table 5-7.

The V K edge EXAFS data for the lead-pyrovanadate materials have been analysed with two shells consisting, respectively, of two oxygens with bond lengths of 1.71 and a vanadium with V-V distance of 2.88 Å for the sequential materials,
Figure 5. The V K edge EXAFS data relative to the $(Ca_{2-x},Me_x)V_2O_7$ arrays have been analysed with one single shell of four oxygens for the Pb and Cd arrays, and three oxygens for the Sr array, bonded to the vanadium with V-O bond lengths between 1.57 and 1.66 Å, Figure 10.

The Ca K-edge EXAFS data of the lead, cadmium and strontium pyrovanadate sequential materials, have been all analysed with two shells of oxygen (with Ca-O bond length values between 2.36 and 2.40 Å) and vanadium (with Ca-V distance values between 3.62 and 3.68 Å) atoms respectively, Figure 6. The Pb L_3 edge EXAFS data have been analysed with two shells of oxygens (with Pb-O bond length values between 2.47 and 2.49 Å and between 2.88 and 2.91 Å, respectively), and a third shell of vanadium atoms (with Pb-V distance of about 3.77 Å), Figure 7. The lead pyrovanadate material for x = 0.05 does not display the second Pb-O shell, and has a Pb-V distance value of 3.70 Å in the third shell. The Cd K edge EXAFS data have been analysed with two shells of oxygen (with Cd-O bond length values between 2.27 and 2.29 Å), and vanadium (with Cd-V distance values of 3.56 Å) atoms, Figure 8. Finally, the Sr K edge EXAFS data have been analysed with two shells of oxygen (with Sr-O bond lengths value between 2.52 and 2.54 Å), and vanadium (with Sr-V distance values between 3.82 and 3.85 Å) atoms, Figure 9.

The bond length values of the V-O and the V-V distances obtained for the lead pyrovanadate sequence were similar to the value reported in the literature [1, 2]. The XAFS V K edge data obtained for the sequential materials allowed for the refinement of the experimental data with two oxygen atoms in the first shell, rather then the four (for the vanadium in tetrahedral coordination) and the five (for the vanadium in distorted square pyramids coordination) V-O bonds expected, Figure 4 and Figure 5. Since these experiments have been performed in fluorescence mode some self absorption, within the sample, of the emitted vanadium K_α photons (4953 eV) accounts for the observed reduction in coordination number. These self absorption effects were more prominent in the sequential materials prepared as pellets compared to the thin array samples.

The XAFS V K edge data obtained for the pyrovanadate arrays, display one single shell made by four oxygens, even though the V-O bond length values appear slightly shorter as compared to the sequential materials. This is due to the lower quality data obtained on the inhomogeneously deposited materials on the array, and consequently to the shorter k range used to refine the arrays data, $\Delta k = 5$ Å^{-1} for the array and $\Delta k = 7$ Å^{-1} for the sequential materials, Figure 10.

The Ca-O bond lengths together with the Ca-V distances, obtained from the data analysis of the sequential lead, cadmium and strontium pyrovanadate materials were also in good agreement with respect to the values reported in literature [1, 2]. The Ca-O coordination number obtained from the lead (four) and from the cadmium and strontium (three) pyrovanadate materials, is not consistent with the seven expected from the pyrovanadate structure. This is a direct consequence of the experimental conditions.

It should be considered that: calcium is a light element, its absorption energy is low (XAFS Ca K edge is about 4038 eV), and therefore the mass absorption coefficient of the matrix (oxygen, vanadium and lead or cadmium or strontium) is very high [8, 9]. Thus, as a consequence, the penetration depths decrease together with the volume of material we are able to sample. Furthermore, since the XAFS Ca K edge experiments have been performed in fluorescence mode some auto absorption, within the sample, of the emitted calcium K_α photons (3692 eV) could result in a reduction of the data quality potentially obtainable from the experiment.
Finally the Pb-O, Cd-O, and Sr-O coordination number and bond length values were consistent with the expected replacement of the calcium by the lead, cadmium, and strontium atoms in the pyrovanadate structure.

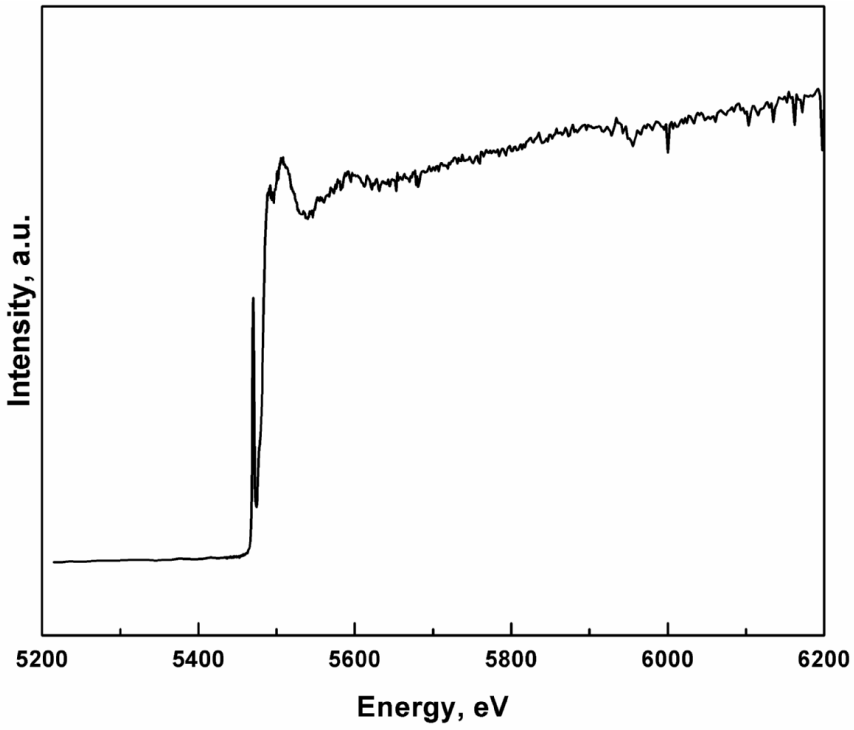

Figure 4 – The experimental raw V K XAFS data of the sequential $(Ca_{1.65},Pb_{0.35})V_2O_7$ sol-gel material

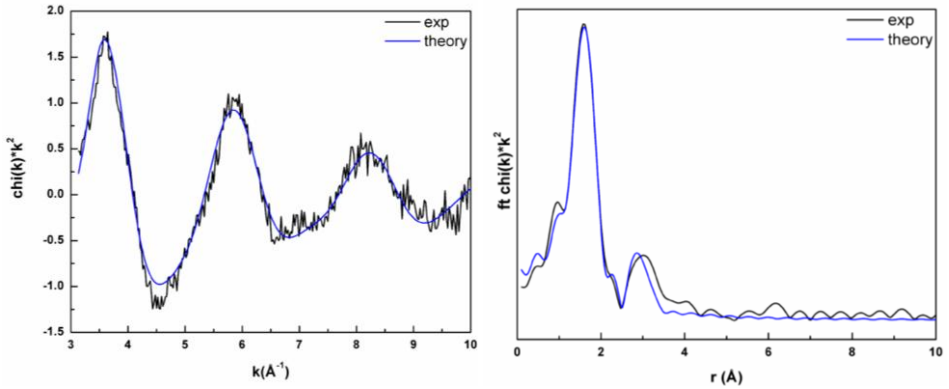

Figure 5 – The experimental raw and fitted k^2-weighted V K edge EXAFS (left) and Fourier transform (right) of the sequential $(Ca_{1.65},Pb_{0.35})V_2O_7$ sol-gel material

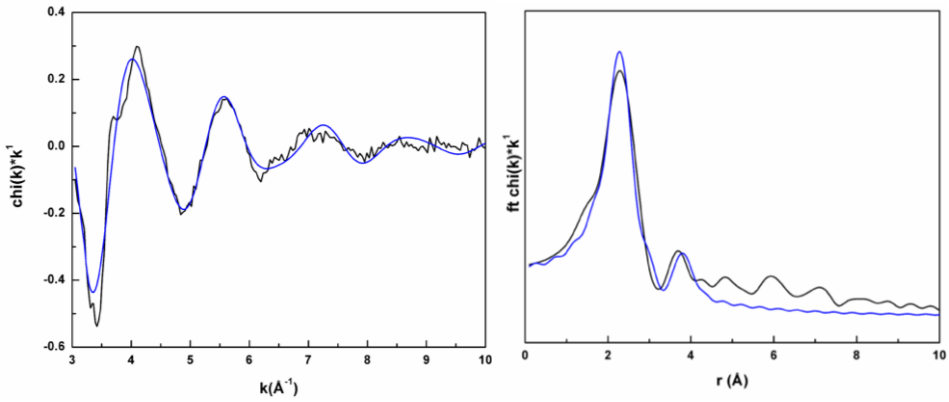

Figure 6 – The experimental raw and fitted k^1-weighted Ca K edge EXAFS (left) and Fourier transform (right) of the sequential $(Ca_{1.65},Pb_{0.35})V_2O_7$ sol-gel material

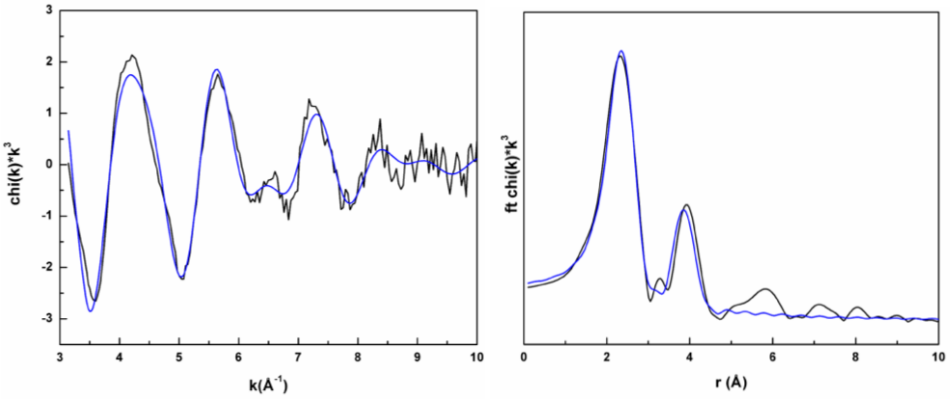

Figure 7 – The experimental raw and fitted k^3-weighted Pb L_3 edge XAFS (left) and Fourier transform (right) of the sequential $(Ca_{1.65},Pb_{0.35})V_2O_7$ sol-gel material

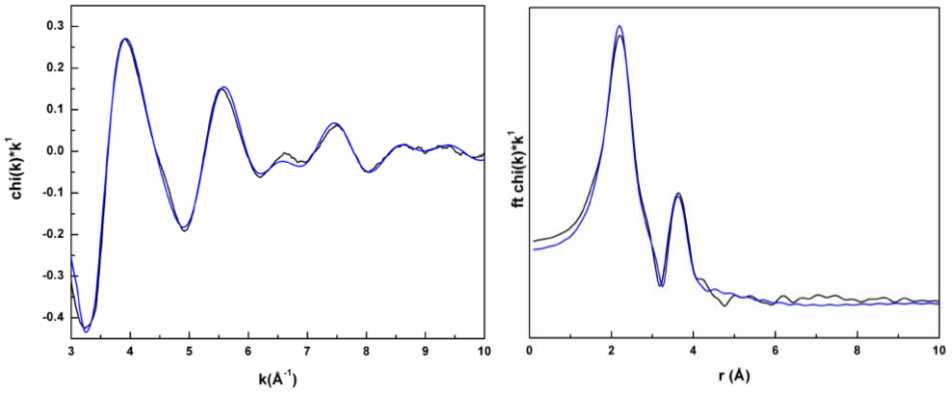

Figure 8 – The experimental raw and fitted k^1-weighted Cd K edge XAFS (left) and Fourier transform (right) of the sequential $(Ca_{1.75},Cd_{0.25})V_2O_7$ sol-gel material

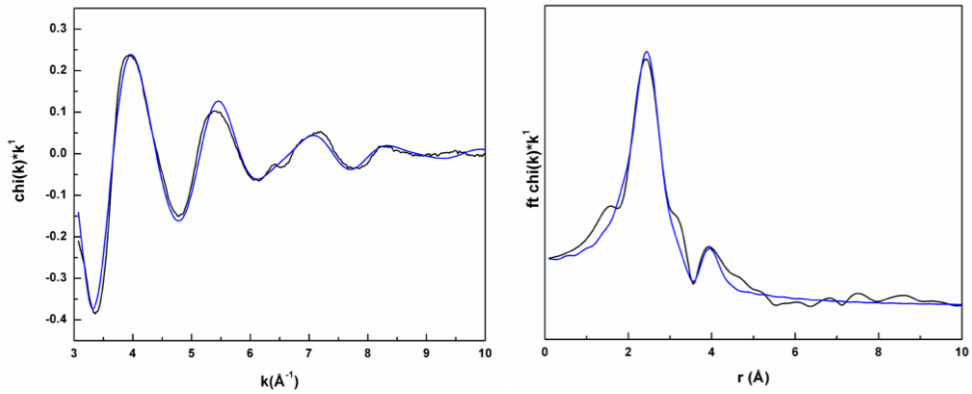

Figure 9 – The experimental raw and fitted k^1-weighted Sr K edge XAFS (left) and Fourier transform (right) of the sequential $(Ca_{1.80},Sr_{0.20})V_2O_7$ sol-gel material

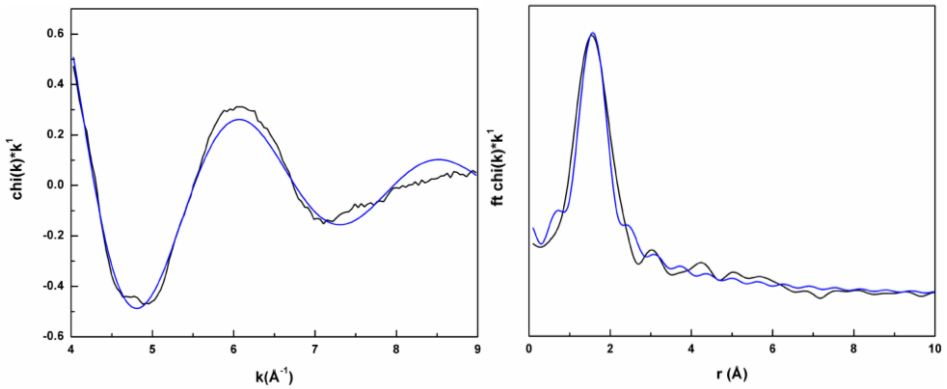

Figure 10 – The experimental raw and fitted k^2-weighted V K edge XAFS (left) and Fourier transform (right) of the $(Ca_{1.70},Pb_{0.30})V_2O_7$ array sol-gel material

Table 5 - Bond length (Å) of sequential sol-gel and array $(Ca_{2-x},Pb_x)V_2O_7$ ($0.00 \leq x \leq 0.35$), calculated from the EXAFS both V and Ca K edge and Pb L_3 edge data analysis

Sample	Ca-O (s.g.)	Ca-V (s.g.)	Pb-O (s.g.)	Pb-O (s.g.)	Pb-V (s.g.)	V-O (s.g.)	V-V (s.g.)	V-O (array)
	C.N.= 4	2	6	1	4	2	1	4
0.00	2.37(1)	3.67(3)	-	-	-	-	-	1.57(2)
0.05	-	-	2.47(1)	-	3.70(2)	1.71(1)	2.88(2)	1.63(1)
0.10	2.38(1)	3.66(3)	-	-	-	-	-	1.65(1)
0.15	2.38(1)	3.68(3)	-	-	-	-	-	1.66(1)
0.20	2.40(1)	3.64(3)	2.49(1)	2.91(4)	3.77(1)	-	-	1.65(1)
0.25	2.37(1)	3.66(4)	2.47(1)	2.89(7)	3.77(1)	-	-	1.64(1)
0.30	2.37(1)	3.66(4)	2.48(1)	2.88(8)	3.77(1)	-	-	-
0.35	2.37(1)	3.67(4)	2.48(1)	2.89(5)	3.78(1)	1.70(1)	2.88(2)	-

Table 6 - Bond length (Å) of sequential sol-gel and array $(Ca_{2-x},Cd_x)V_2O_7$ ($0.00 \leq x \leq 0.30$), calculated from the EXAFS V, Ca and Cd K edge data analysis

Sample	Ca-O (s.g.)	Ca-V (s.g.)	Cd-O (s.g.)	Cd-V (s.g.)	V-O (array)
	C.N.=3	1	6	4	4
0.05	2.36(1)	3.65(4)	2.28(1)	3.56(1)	1.59(1)
0.10	2.37(1)	3.64(3)	2.27(1)	3.56(1)	1.59(1)
0.15	2.36(1)	3.64(3)	2.28(1)	3.56(1)	1.61(1)
0.20	2.36(1)	3.62(3)	2.28(1)	3.56(1)	1.59(1)
0.25	-	-	2.29(1)	3.57(1)	1.64(1)
0.30	-	-	-	-	1.60(1)

Table 7 - Bond length (Å) of sequential sol-gel and array $(Ca_{2-x},Sr_x)V_2O_7$ ($0.00 \leq x \leq 0.25$), calculated from the EXAFS V, Ca and Sr K edge data analysis

Sample	Ca-O (s.g.)	Ca-V (s.g.)	Sr-O (s.g.)	Sr-V (s.g.)	V-O (array)
	C.N.=3	1	6	4	3
0.05	2.38(1)	3.66(3)	2.52(1)	3.82(2)	1.65(1)
0.10	2.38(1)	3.66(3)	2.53(1)	3.82(1)	1.65(1)
0.15	2.38(1)	3.66(4)	2.53(1)	3.83(2)	1.65(1)
0.20	2.38(1)	3.66(3)	2.53(1)	3.85(2)	1.65(1)
0.25	2.38(1)	3.66(4)	2.54(1)	3.85(2)	1.65(1)

6.4 Raman Spectra of $(Ca,Me)_2V_2O_7$

As for the BiMoVOX and BiMeVOX materials, the oxygen atoms in both tetrahedral and distorted square pyramid coordination around the V^{5+}, form strongly bound molecular anions $V_4O_{14}^{8-}$, which are bonded to Ca^{2+} and Me^{2+} (with Me^{2+} = Pb, Cd and Sr) cations in the lattice via relatively weak long-range ionic forces. Consequently, modes within the V_4O_{14} anions, internal modes, are stronger than those of external modes, corresponding to vibrations between lattice ions. Since pyroanions have many degrees of freedom, their Raman spectra contain several tens of lines as can be seen in the Figures 11 and 12 displaying the sequential $Ca_2V_2O_7$ and $(Ca_{2-x},Pb_x)V_2O_7$ sol-gel series respectively
[10, 11].

For simplicity, we considered the symmetric and antisymmetric stretching modes of the terminal V-O groups, and the symmetric and antisymmetric modes of the bridge V-O-V bonds. The low-frequency deformation modes and the lattice modes of the anions, for frequencies lower then 500 cm^{-1}, due to their complexity were not assigned. The spectra of $Ca_2V_2O_7$ and $(Ca_{2-x},Me_x)V_2O_7$ materials show well defined Raman band at 944 cm^{-1} which can be attributed to the ν_1(V-O) symmetric stretching mode, while the Raman bands at 881, 864, 804 and 785 cm^{-1} are attributed to the ν_3 antisymmetric stretching modes of (V-O) terminal bonds, suggesting a complex coordination for the two V^{5+} with different V-O bond lengths. The Raman bands at 704 and 546 cm^{-1} are assigned, respectively, to the asymmetric and symmetric stretching vibration of the longer V-O-V bridge bonds.

The positions of the stretching motions change together with the degree of doping in all the three different sequential pyrovanadate materials, Table 8 – 10, consistently with the UV-visible results. The V-O ν frequencies shift towards lower energy for the Pb^{2+} doped materials, indicating a decreasing of the covalence of the V-O bonds; whereas an increasing of the covalence of the V-O bonds, with a shift towards higher frequencies, is observed for the Cd^{2+} and Sr^{2+} doped materials.

As for the BiMoVOX and BiMeVOX materials, it was possible to correlate the V-O bond lengths with the Raman stretching frequencies, using the Diatomic Approximation [12, 13]. In this approximation, for the sequential $Ca_2V_2O_7$, the Raman band at about 944 cm^{-1} arises from stretches of a V-O bond with a bond length of 1.63 Å; whereas the Raman bands at about 881, 864, 804, 785, 730 and 546 cm^{-1}

are due to stretches of distinct V-O bonds with bond lengths of 1.66, 1.67, 1.71, 1.72, 1.78 and 1.91 Å, almost constant going through the series. These Raman bond distances are similar to those reported from literature for the V-O bond lengths. Although it is difficult to assign the frequencies of the deformation modes and the lattice modes of the anions, they display similar values to those reported in previous investigations on pyrovanadate materials.

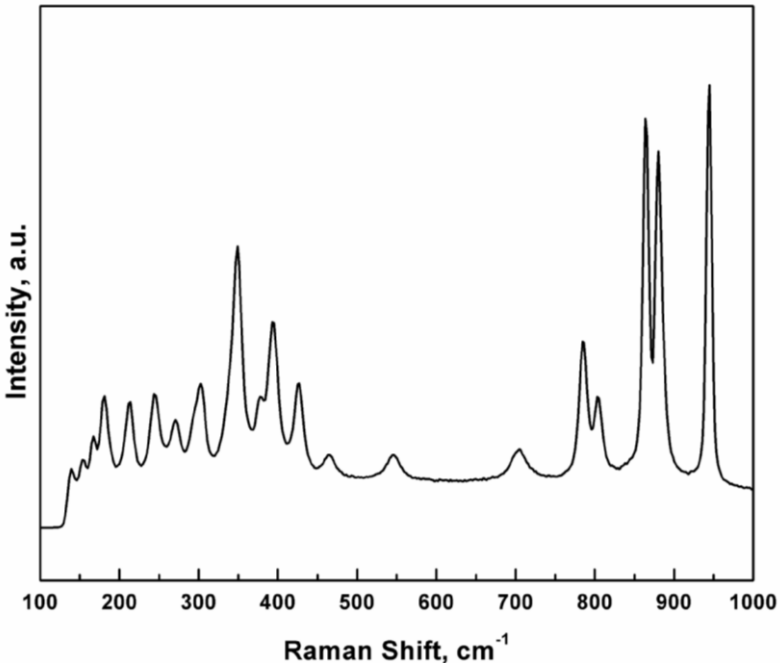

Figure 11 – Raman spectra of $Ca_2V_2O_7$ sequential sol-gel material

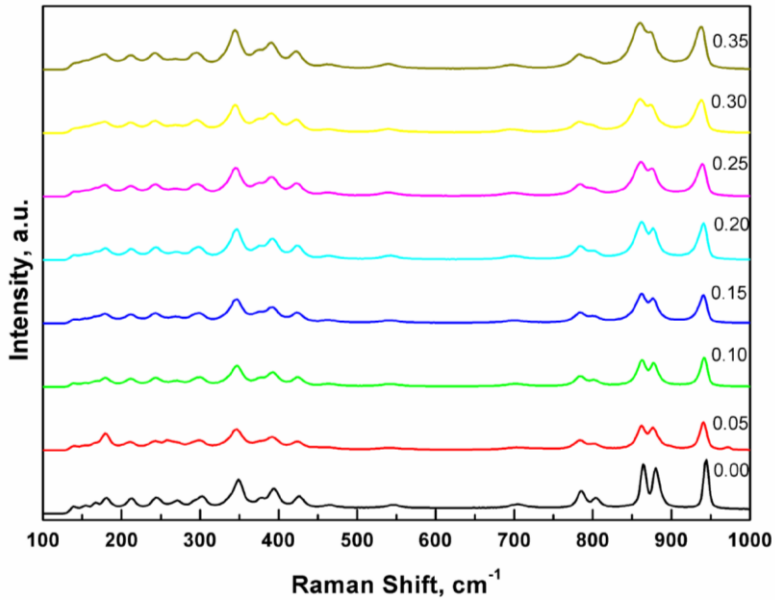

Figure 12 – Raman spectra of $(Ca_{2-x},Pb_x)V_2O_7$ ($0.00 \leq x \leq 0.35$) sequential sol-gel materials

The pyrovanadate array samples display similar Raman modes as in the sequential materials, Figure 13, even if presence of extra vibration modes suggests the existence of small amount of vanadium oxide phases with different stoichiometry. They display the ν_1 symmetric stretching mode at 926 cm^{-1}, and the ν_3 antisymmetric stretching modes of V-O terminal bonds at 864, 846, 787 and 769 cm^{-1}, and the asymmetric and symmetric stretching vibration of the longer V-O-V bridge bonds at 684 and 528 cm^{-1}. The bond lengths calculated from the V-O stretching modes were about 1.63, 1.67, 1.68, 1.72, 1.73, 1.79 and 1.93 Å for the V-O terminal and bridge bonds [12, 13].

Raman data analysis of these $(Ca_{2-x},Me_x)V_2O_7$ array materials are shown in Table 11, 12 and 13. The positions of the V-O stretching motions slightly change together with the degree of doping in all the three different sequential pyrovanadate materials, without any specific trends. In particular data analysis of the calcium lead pyrovanadate array materials result quite complex due to the poor quality of the experimental data. Their intensities was lower if compared with those obtained for the sequential sol-gel samples, and they also change statistically across the array. As discussed for the BiMoVOX array materials, these differences can be attributed to the different thickness, flatness and inhomogeneity of the samples made on the array.

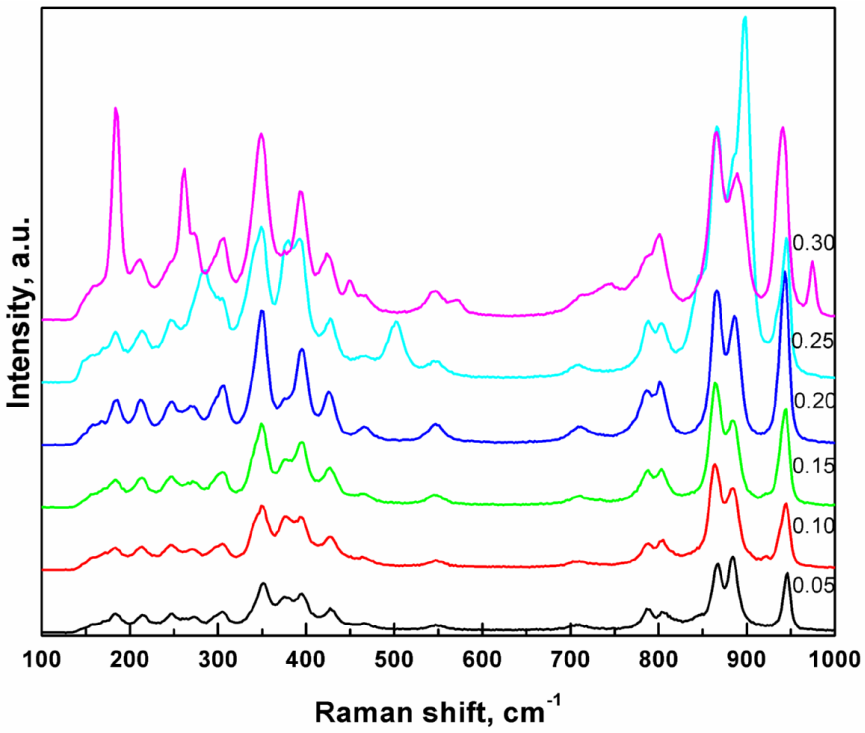

Figure 13 – Raman spectra of $(Ca_{2-x},Cd_x)V_2O_7$ ($0.05 \leq x \leq 0.35$) array sol-gel materials

Table 8 - Results of the Raman spectral analysis (cm^{-1}) of sequential $(Ca_{2-x},Pb_x)V_2O_7$ ($0.00 \leq x \leq 0.35$) sol-gel

Vibr. mode	0.00	0.05	0.10	0.15	0.20	0.25	0.30	0.35
ν_s (V-O)	944	941	941	940	940	938	937	937
ν_s (V-O)	881	877	878	877	877	875	875	874
ν_s (V-O)	864	862	862	862	862	859	858	857
ν_s (V-O)	804	801	801	801	802	801	800	799
ν_s (V-O)	785	784	784	784	785	783	782	781
ν_s (V-O-V)	704	703	701	699	699	699	697	697
ν_s (V-O-V)	546	543	543	542	542	541	541	540

Table 9 - Results of the Raman spectral analysis (cm^{-1}) of sequential $(Ca_{2-x},Cd_x)V_2O_7$ ($0.00 \leq x \leq 0.30$) sol-gel

Vibr. mode	0.00	0.05	0.10	0.15	0.20	0.25	0.30
ν_s (V-O)	944	954	954	953	952	952	953
ν_s (V-O)	881	892	892	893	894	895	894
ν_s (V-O)	864	875	875	875	875	875	875
ν_s (V-O)	804	814	815	814	813	813	813
ν_s (V-O)	785	796	796	796	795	795	796
ν_s (V-O-V)	704	716	720	718	720	720	720
ν_s (V-O-V)	546	557	556	557	557	557	557

Table 10 - Results of the Raman spectral analysis (cm^{-1}) of sequential $(Ca_{2-x},Sr_x)V_2O_7$ ($0.00 \leq x \leq 0.25$) sol-gel

Vibr. mode	0.00	0.05	0.10	0.15	0.20	0.25
ν_s (V-O)	944	955	955	955	955	955
ν_s (V-O)	881	891	890	889	890	889
ν_s (V-O)	864	876	876	876	876	876
ν_s (V-O)	804	816	816	816	817	816
ν_s (V-O)	785	796	796	796	796	795
ν_s (V-O-V)	704	716	714	712	714	713
ν_s (V-O-V)	546	558	557	556	558	556

Table 11 - Results of the Raman spectral analysis (cm^{-1}) of $(Ca_{2-x},Pb_x)V_2O_7$ ($0.00 \leq x \leq 0.25$) array sol-gel

Vibr. mode	0.00	0.05	0.10	0.15	0.20	0.25
ν_s (V-O)	-	-	926	924	925	-
ν_s (V-O)	869	869	864	864	862	868
ν_s (V-O)	831	835	847	845	845	840
ν_s (V-O)	803	803	789	778	786	802
ν_s (V-O)	-	-	769	769	767	-
ν_s (V-O-V)	-	-	684	680	684	-
ν_s (V-O-V)	-	-	528	530	526	546

Table 12 - Results of the Raman spectral analysis (cm^{-1}) of $(Ca_{2-x},Cd_x)V_2O_7$ ($0.05 \leq x \leq 0.30$) array sol-gel

Vibr. mode	0.05	0.10	0.15	0.20	0.25	0.30
ν_s (V-O)	946	944	943	943	944	940
ν_s (V-O)	885	884	885	886	898	890
ν_s (V-O)	866	864	865	866	866	865
ν_s (V-O)	809	806	802	802	803	802
ν_s (V-O)	787	786	785	784	786	784
ν_s (V-O-V)	708	711	712	714	712	713
ν_s (V-O-V)	549	549	547	547	548	546

Table 13 - Results of the Raman spectral analysis (cm^{-1}) of $(Ca_{2-x},Sr_x)V_2O_7$ ($0.00 \leq x \leq 0.20$) array sol-gel

Vibr. mode	0.05	0.10	0.15	0.20
ν_s (V-O)	947	947	947	945
ν_s (V-O)	883	883	882	879
ν_s (V-O)	867	867	866	865
ν_s (V-O)	807	807	809	806
ν_s (V-O)	788	787	787	784
ν_s (V-O-V)	706	705	702	708
ν_s (V-O-V)	549	549	549	545

6.5 UV-visible Diffuse Reflectance Spectra and SEM of $(Ca,Me)_2V_2O_7$

UV-visible spectra of the sequential $(Ca_{2-x},Pb_x)V_2O_7$ materials made by the sol-gel method were monotonically red-shifted together with the Pb loading, Figure 14 (left). These results, displaying only a single optical edge for each sample, indicate that the powders obtained were homogeneous solid-solutions, rather than a mixture of calcium and lead pyrovanadate oxides. The optical trend is clearly visible in Figures 14 (right) in which the band gaps of $(Ca_{2-x},Me_x)V_2O_7$, with Me = Pb^{2+}, Cd^{2+} and Sr^{2+}, materials are shown. The Pb effect on the electronic structure of the $Ca_2V_2O_7$, as well as in the Cd and Sr cases, needs to be taken into account to explain the colour properties observed. Since that the $V_4O_{14}^{8-}$ consists of two VO_4 tetrahedra and two VO_5 distorted square pyramid that share common oxygen atoms, we propose to use the electron structure of the VO_4^{3-} ion as a first approximation in the comparison with the experimental data on the sequential $(Ca_{2-x},Me_x)V_2O_7$ materials [14, 15]. In this approximation, the top of the valence bands of pure $Ca_2V_2O_7$ is composed by O 2p orbitals, while the V 3d the $Ca_2V_2O_7$ contribute to form the bottom of the conduction band, Figure 15.

Lead doping of calcium pyrovanadate results in a Pb 6s – O 2p bonding interaction at the bottom of the valence band, and at the same time a Pb 6s – O 2p antibonding interaction at the top of the valence band. These antibonding interactions destabilise states at the top of the valence band and are responsible for the decrease in the band gap of $(Ca_{2-x},Pb_x)V_2O_7$ with respect to $Ca_2V_2O_7$ [16, 17]. In the case of the strontium doped pyrovanadate materials, since the difference in effective electronegativity between the Sr^{2+} (1.33) respect to the Ca^{2+} (1.35) [18, 19], is quite small, the band gap energy value does not change consistently with the amount of metal doping. A similar result on the colour properties is obtained in the cadmium pyrovanadate materials. The reason in this case arises from the Cd 4d levels contributing to the valence bands. Since they are located at the bottom of these bands [20-23], Cd doping of the calcium pyrovanadate materials does not influence the position of the top of the valence bands and consequently the value of the final band gap of the electronic transition.

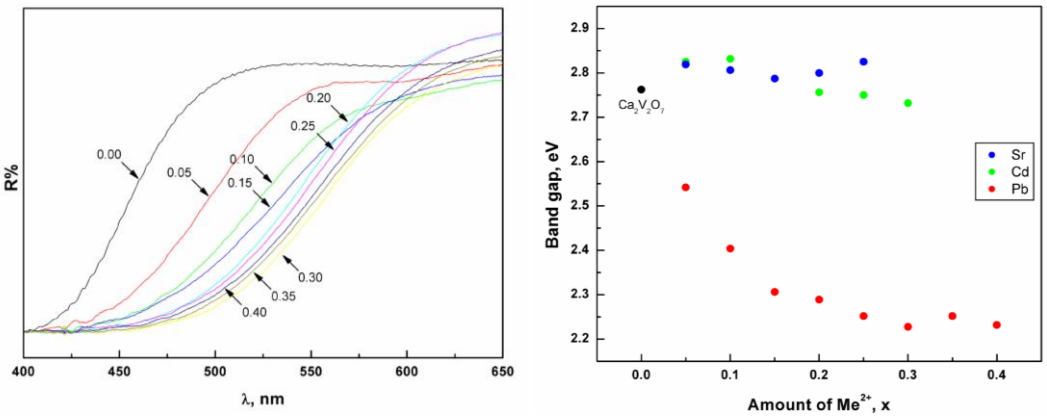

Figure 14 – UV-visible reflectance spectra of sequential $(Ca_{2-x},Pb_x)V_2O_7$ (left) and band gap energies of sequential $(Ca_{2-x},Me_x)V_2O_7$ (right) materials

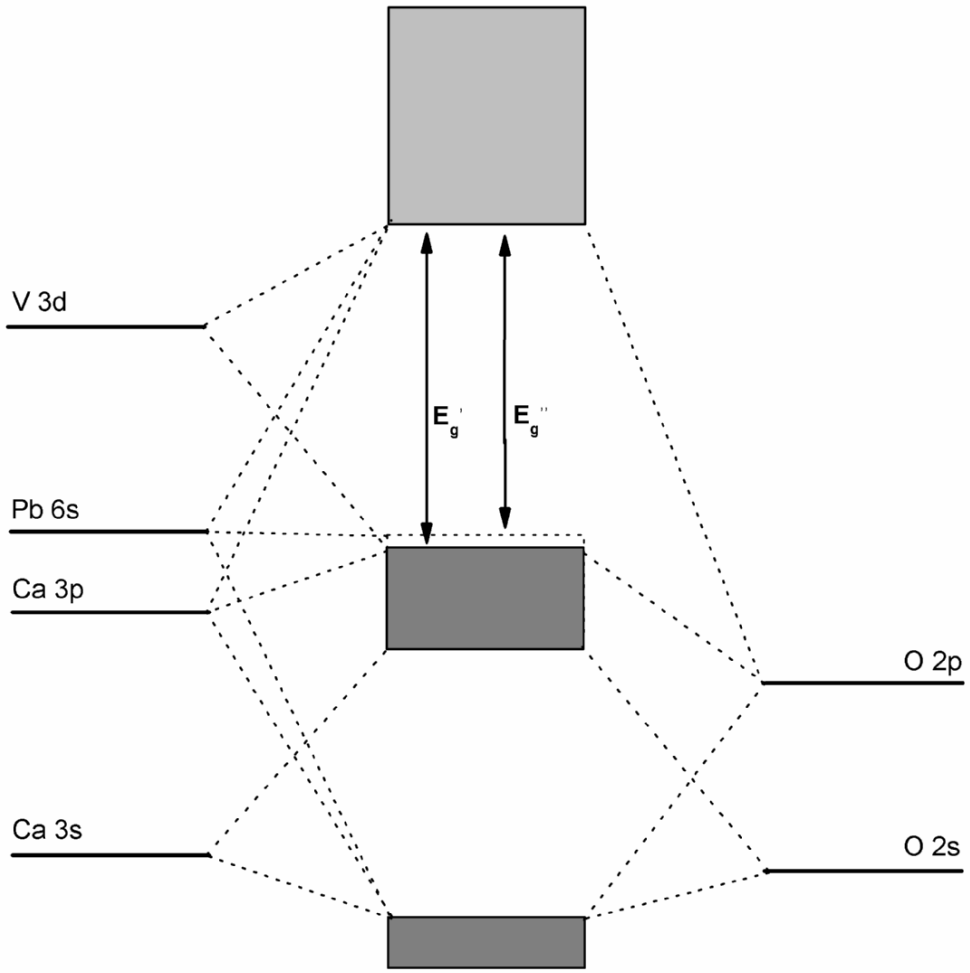

Figure 15 – Schematic molecular orbital diagram of the sequential calcium pyrovanadate materials; E_g' = band gap of triclinic $Ca_2V_2O_7$, E_g'' = band gap of triclinic $(Ca,Pb)_2V_2O_7$

The $(Ca_{2-x},Me_x)V_2O_7$ materials display particles with an irregular shape and size in a range of $1.0 \leq \mu m \leq 4.0$, as can be seen, for example, in the SEM and TEM pictures, Figure 16, for the lead pyrovanadate materials.

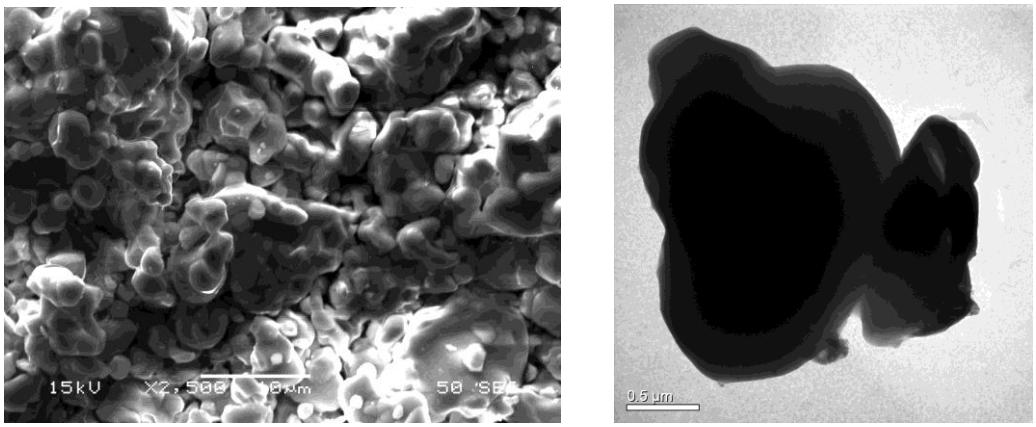

Figure 16 – SEM (left) and TEM (right) photographs of sequential $(Ca_{1.7},Pb_{0.3})V_2O_7$ sol-gel materials

6.6 Conclusions

The synthesis of $Ca_2V_2O_7$ around 700°C produced triclinic pyrovanadate crystal structure. A combined characterization approach of complementary techniques, i.e. XRD powder diffraction, Raman and XAFS spectroscopy reveals that pyrovanadate materials kept their triclinic crystal structure under cadmium, strontium, and lead doping, in which Cd^{2+}, Sr^{2+}, and Pb^{2+} directly replace the Ca^{2+} in the pyrovanadate structure.

The lead pyrovanadate materials can be considered as potential new class of inorganic pigments. Doping produces materials ranging in colour from pale yellow to red depending on the Pb^{2+} cation content. In the cadmium and strontium pyrovanadate materials due to the presence of factors such as relative small difference in effective electronegativity between the doping and the replaced cations, or the low overlapping between the doping metal d orbitals and oxygen 2p, the band gap energy values do not change consistently together with the amount of metals doping.

Arrays of vanadium lead, or strontium, or cadmium mixed metal oxide compounds are prepared in a high-throughput manner, with the peroxo sol-gel route, using robotic methodologies. These arrays can successfully be analysed for their structural and compositional properties in a rapid manner providing an increase in efficiency compared to one-at-a-time experiments.

6.7 Experimental Section

6.7.1 Preparation of $(Ca,Me)_2V_2O_7$ Sequential Materials

A peroxo sol-gel method of synthesis have been utilised to obtain the $(Ca_{2-x},Me_x)V_2O_7$, with Me = Cd, Sr, and Pb materials:

Peroxo sol-gel synthesis:

Sol-gel specimens were prepared by peroxo sol-gel route. In a typical sequential pyrovanadate peroxo sol gel synthesis, calcium nitrate solutions were prepared dissolving 0.95 g of $Ca(NO_3)_2{\cdot}4\ H_2O$ (99.98%, Alfa Aesar) in H_2O. Precursor vanadium, cadmium, strontium, and lead solutions were prepared separately, from 0.5 g of NH_4VO_3 (99%, Alfa Aesar) dissolved in H_2O_2(30%)/H_2O (1:1), 0.07 g of $Cd(NO_3)_2 \cdot 4H_2O$ (99.99%, Alfa Aesar), 0.05 g of $Sr(NO_3)_2$ (99.97%, Alfa Aesar), and 0.07 g of $Pb(NO_3)_2$ (99.999%, Alfa Aesar) dissolved in H_2O. The two nitrate solutions, the calcium solution with the cadmium, strontium or lead, were then added together and stirred for 30 min. Finally the vanadium solutions were added drop-wise to the calcium-doping metal nitrate solutions, while stirring was continued for a further 2 h. The mixed solutions were heated up to 120 °C until evaporation of the solvent was completed, after which the red-brown precipitate was heated to 700 °C for 24 h in an O_2 atmosphere, with a temperature gradient of 0.5 °C/min.

6.7.2 Preparation of $(Ca,Me)_2V_2O_7$ Arrays

Arrays of pyrovanadate materials were prepared by peroxo sol-gel route, from solutions of the metal nitrates or ammoniates (about 0.5 M) in diluted nitric acid or hydrogen peroxide in water (1:1) and water. In a typical peroxo sol-gel pyrovanadate array synthesis, calcium nitrate solutions were prepared dissolving 0.7 g of $Ca(NO_3)_2{\cdot}4\ H_2O$ (99.98%, Alfa Aesar) in H_2O. Precursor vanadium, cadmium, strontium, and lead solutions were prepared separately, from 0.3 g of NH_4VO_3 (99%, Alfa Aesar) dissolved in H_2O_2(30%)/H_2O (1:1), 0.07 g of $Cd(NO_3)_2 \cdot 4H_2O$ (99.99%, Alfa Aesar), 0.05 g of $Sr(NO_3)_2$ (99.97%, Alfa Aesar), and 0.08 g of $Pb(NO_3)_2$ (99.999%, Alfa Aesar) dissolved in H_2O.

These were dispensed into a standard 54 well plate (reusable Teflon mask system, with a 6 x 9 grid of 5 mm sized holes, pressed on an alumina tile by stainless steel plates) in the appropriate ratios and mixed using a Packard Multiprobe II robot. Then

the array was left for 12 hours at ambient temperature in air atmosphere, and after that, the solvent was evaporated at 60 °C overnight in an oven in air atmosphere before the alumina tile was fired up to 700 °C in a furnace in oxygen atmosphere for 24 h.

6.7.3 XRD Powder diffraction

Diffraction patterns were obtained using a Siemens D5000 (Cu $K_{\alpha 1}$ radiation, λ = 1.5406 Å) for both the sequential and arrays series. The phases were identified by comparison with the PDF2 database. Data refinement of the sequential materials was performed using the GSAS program.

6.7.4 XAS spectroscopy

XAS spectroscopy studies were carried out at the Science and Technology Facility Council's (STFC) Synchrotron Radiation Source (SRS) at the Daresbury Laboratory (Daresbury, U.K.), at the Hamburger Synchrotronstrahlungslabor (HASYLAB) at Deutsches Elektronen-Synchrotron (DESY), and at the European Synchrotron Radiation Facility (ESRF) (in Grenoble, France).

The Pb L_3 (13035 eV), and Ca K (4039 eV) edge XAS studies were performed at station 9.3 and 7.1 of the SRS using a Si(111), and Si(220) double crystal monochromator, respectively. In the Pb case the data were obtained in transmission mode, whereas the Ca and V data were collected in fluorescence mode using a 13 element Ge solid state detector.

The V K (5465 eV) of the sequential lead and cadmium pyrovanadate materials were collected at the Beamline E4, whereas the Sr K edge (16105 eV), and Cd K edge (26711 eV) of the sequential samples were collected at Beamline X1 at the Hamburger Synchrotronstrahlungslabor (HASYLAB) at Deutsches Elektronen-Synchrotron (DESY). The V K edge were collected in fluorescence mode using a Si(111) double crystal monochromator, and a 9 element Ge solid state detector. A Si(311) double crystal monochromator was used for the Sr K , Cd K; data were collected in transmission mode.

Bi foil (L_3 edge = 13035 eV) was used for the calibration of the Pb L_3 edge, whereas the V foil (K edge = 5465 eV) was used for the Ca K and V K data. The Bi foil (L_1 edge = 16388 eV) was used for the calibration of the Sr K edge. The Ag foil (K edge = 25514 eV) was used for the calibration of the Cd K edge.

The V K (5465 eV) of the lead, strontium and cadmium pyrovanadate array materials were collected at the ESRF beamline BM26A (DUBBLE). In all cases the data were obtained with a Si(111) double crystal monochromator with a 13 element Ge solid state detector. V foil (K edge = 5465 eV) was used for the calibration of the V edges. Data were acquired with a Δk of 0.04 $Å^{-1}$ and a data acquisition time of 20 min. per scan. The sequential samples were mounted in a self supporting sample holder. All samples were characterized in the HTP chamber, allowing combined XAS, XRD and Raman [24].

EXAFS data analysis of both sequential and array materials were performed using the *X-Mult* and *Excurve(9.301)* programs [7, 25].

6.7.5 UV/Vis and Raman diffuse reflectance

Absorption measurements of the sequential samples were performed using a Perkin Elmer Lambda 35 UV/vis spectrometer in diffuse reflectance mode. Spectra were collected in the visible range of 380 – 780 nm. The band gaps energy values are calculated from the maximum of the first derivative of the absorption edges. Raman spectra of both bulk and array samples were collected with an optical fibre Renishaw RA100U Spectrometer, using high-power NIR laser (785 nm) with a resolution of 3 cm^{-1} in the range between 100 and 1000 cm^{-1}. Spectra were calibrated using the 520.5 cm^{-1} line of a silicon wafer.

6.7.6 Electron Microscopy

Transmission Electron Microscopy data were collected using a JEM 3010 transmission electron microscope.

Scanning Electron Microscopy data were collected using a JSM 5910 scanning electron microscope. Images of each spot were taken at 2000x magnification with a spot size of 21, accelerating voltage of 15 kV.

6.8 References

1. V.K. Trunov, I.A. Velikodnyi, E.V. Murashova, and V.D. Zhuravlev, Dok. Akad. Nauk Sssr, **1983**, 270, 886-887.
2. T.I. Krasnenko, L.V. Andrianova, L.V. Zolotukhina, and A.A. Fotiev, Inorg. Mater., **1998**, 34, 733-736.
3. A.C. Larson and R.B. Von Dreele, *Generalised Structure Analysis System*, Los Alamos National Laboratory, Los Alamos, **2004**.
4. R.D. Shannon, Acta Crystallogr. Sect. A, **1976**, 32, 751-767.
5. J. Wong, F.W. Lytle, R.P. Messmer, and D.H. Maylotte, Phys. Rev. B, **1984**, 30, 5596-5610.
6. S.E. Shadle, B. Hedman, K.O. Hodgson, and E.I. Solomon, Inorg. Chem., **1994**, 33, 4235-4244.
7. N. Binsted, *EXCURV(9.301)*. CCLRC Daresbury Laboratory Computer program, **1998**.
8. U. Turgut, O. Simsek, E. Buyukkasap, and M. Ertugrul, Spectroc. Acta Pt. B-Atom. Spectr., **2002**, 57, 261-266.
9. B.L. Henke, E.M. Gullikson, and J.C. Davis, Atom. Data Nucl. Data Tables, **1993**, 54, 181-342.
10. R.G. Brown and S.D. Ross, Spectrochim. Acta Part a-Molec. Spectr., **1972**, 28A, 1263-1274.
11. Y.K. Voron'ko, A.A. Sobol, and V.E. Shukshin, Inorg. Mater., **2005**, 41, 1097-1106.
12. F.D. Hardcastle and I.E. Wachs, J. Raman Spectrosc., **1990**, 21, 683-691.
13. F.D. Hardcastle and I.E. Wachs, J. Phys. Chem., **1991**, 95, 5031-5041.
14. I.M. Curelaru, K.G. Strid, E. Suoninen, E. Minni, and T. Ronnhult, Phys. Rev. B, **1981**, 23, 3700-3709.
15. I.M. Curelaru, E. Suonien, E. Minni, K.G. Strid, and T. Ronnhult, J. Lumines., **1983**, 28, 123-133.
16. M.W. Stoltzfus, P.M. Woodward, R. Seshadri, J.H. Klepeis, and B. Bursten, Inorg. Chem., **2007**, 46, 3839-3850.
17. D.J. Singh, G.E. Jellison, and L.A. Boatner, Phys. Rev. B, **2006**, 74, 155126(1-6).
18. R.T. Sanderson, J. Chem. Educ., **1988**, 65, 112-118.
19. R.T. Sanderson, J. Chem. Educ., **1988**, 65, 227-231.

20. H. Rozale, B. Bouhafs, and P. Ruterana, Superlattices Microstruct., **2007**, 42, 165-171.
21. Y. Dou, R.G. Egdell, D.S.L. Law, N.M. Harrison, and B.G. Searle, J. Phys.-Condes. Matter, **1998**, 10, 8447-8458.
22. H. Harima, J. Phys. Chem. Solids, **2002**, 63, 1035-1038.
23. Y. Abraham, N.A.W. Holzwarth, and R.T. Williams, Phys. Rev. B, **2000**, 62, 1733-1741.
24. M. Tromp, S. Russu, A.J. Dent, J.F.W. Mosselmans, J. Evans*, et al.*, A.I.P., **2007**, CP 882, 858-860.
25. N. Binsted, *X-Mult*. University of Southampton, Southampton, **2006**.

CHAPTER SEVEN

CONCLUSIONS

Chapter Seven: Conclusions

7.1 Conclusions

The constant improvement of novel inorganic pigments has become essential to deliver materials for the various and challenging applications of a growth market [1]. Improvements of the existing varieties of inorganic pigments include materials with superior chemical properties, together with the possibility to increase the range of colour available. Furthermore, their synthesis and characterisation with high throughput methods can provide an economically, fast and practical solution to the pursuit of novel materials [2]. Therefore this work has aimed at increasing and improving on the current choice of mixed metal oxide pigments by high throughput methods.

The synthesis of $BiVO_4$ and α-$Bi_2VO_{5.5-\delta}$ at temperatures around 700°C produced monoclinic distorted scheelite crystal structure, and monoclinic Aurivillius type crystal structure, respectively; whereas the synthesis of $Ca_2V_2O_7$ a similar temperatures produced triclinic pyrovanadate crystal structure [3-6]. A combined characterization approach of complementary techniques, i.e. XRD powder diffraction, Raman and XAFS spectroscopy reveals that molybdenum doping of monoclinic $BiVO_4$ leads to tetragonal $Bi_{1-x/3}Mo_xV_{1-x}O_4$, in which the Mo^{6+} directly replaces the V^{5+} in the scheelite structure [7].

In similar manner, both the Cu^{2+} and Fe^{3+} doping of monoclinic α-$Bi_2VO_{5.5-\delta}$ leads to tetragonal γ-$Bi_2V_{1-x}Cu_xO_{5.5-(3x/2)-\delta}$ and γ-$Bi_2V_{1-x}Fe_xO_{5.5-x-\delta}$ Aurivillius type crystal structure [8, 9]. Pyrovanadate materials kept their triclinic crystal structure under cadmium, strontium, and lead doping, in which Cd^{2+}, Sr^{2+}, and Pb^{2+} directly replace the Ca^{2+} in the pyrovanadate structure [6].

The multi-edge XAFS and PD combined data refinement of the BiMoVOX materials, performed using the program P shows a clear improvement in the fits for the sequential material, especially for the diffraction data. Furthermore, the simultaneous refinement has the clear advantage in revealing overall structural trends more readily, as well as being faster [10].

Although the photophysical properties and colour intensity of vanadium mixed metal oxide materials depend on many factors including method of synthesis, crystal structure, phase composition, stoichiometry, particle size and morphology; it has been proven possible to control the pigment colours of these materials through the "band-engineering" method. The BiMoVOX, BiCuVOX, and lead pyrovanadate (despite its potential toxicity) materials can be considered as potential new class of inorganic pigments. In the BiFeVOX, cadmium, and strontium pyrovanadate materials due to the presence of factors such as oxygens vacancies, or relative small difference in effective electronegativity between the doping and the replaced cations, the band gap energy values do not change consistently together with the amount of metals doping.

Arrays of vanadium mixed metal oxide compounds are prepared in a high-throughput manner, with the peroxo sol-gel route, using robotic methodologies. The use of such chemistry requires a detailed understanding of the sol-gel chemistry to be developed and optimised for the particular system under study. Once this has been completed then the chemistry may be widely used for generating arrays of complex mixed metal oxide systems. During the development of the synthesis method, the evaporation of the solvent during the ageing step has been the mainly issue. In many cases rings of sample formed instead of spots. This problem has been described in several high throughput studies, and it was attributed to the surface tension of the liquid [2, 11-13]. In this study, the ageing/drying conditions were investigated to minimise this ring effect. The most effective way to produce uniform samples was to remove the Teflon mask while a small amount of solvent remained. Increasing the well diameter from 5 to 7 mm also helped alleviate the problem.

Even though all the array materials displayed a lower crystallinity compared to the sequentially synthesised materials, structural characterisation of the arrays showed that it is possible to study and develop new families of pigments within the high-throughput approach. Automatic acquisition of XAFS, Raman and XRD data for large arrays of samples is performed [14]. Further optimization of the process is required, however, with the current synthesis and analysis system an array of 54 samples can be prepared and characterised in about 2 days. This presents a significant improvement on the standard one-at-a-time approach, which takes about three days for each sample.

The main challenge of high-throughput experimentation is the analysis of the large amounts of data created. Improvements in data handling using specific software developed for combined XAFS/XRD high-throughput data analysis as shown should reduce this problem and will allow more complex pigment systems to be studied efficiently [10, 15].

7.2 References

1. R. Adams, Foc. on Pigm., **2007**, 1, 1-2.
2. S.J. Henderson, Ph.D. Thesis, School of Chemistry, Southampton University, **2006**, Southampton.
3. A.W. Sleight, H.Y. Chen, A. Ferretti, and D.E. Cox, Mater. Res. Bull., **1979**, 14, 1571-1581.
4. G. Mairesse, P. Roussel, R.N. Vannier, M. Anne, C. Pirovano*, et al.*, Sol. St. Sci., **2003**, 5, 851-859.
5. G. Mairesse, P. Roussel, R.N. Vannier, M. Anne, and G. Nowogrocki, Sol. St. Sci., **2003**, 5, 861-869.
6. V.K. Trunov, I.A. Velikodnyi, E.V. Murashova, and V.D. Zhuravlev, Dok. Akad. Nauk Sssr, **1983**, 270, 886-887.
7. W.F. Yao and J.H. Ye, J. Phys. Chem. B, **2006**, 110, 11188-11195.
8. C.K. Lee and A.R. West, Sol. St. Ion., **1996**, 86-88, 235-239.
9. O. Joubert, M. Ganne, R.N. Vannier, and G. Mairesse, Sol. St. Ion., **1996**, 83, 199-207.
10. N. Binsted, M.J. Pack, M.T. Weller, and J. Evans, J. Am. Chem. Soc., **1996**, 118, 10200-10210.
11. B. Wessler, V. Jehanno, W. Rossner, and W.F. Maier, Appl. Surf. Sci., **2004**, 223, 30-34.
12. J.N. Cawse, D. Olson, B.J. Chisholm, M. Brennan, T. Sun*, et al.*, Prog. Org. Coat., **2003**, 47, 128-135.
13. J. Wang and J.R.G. Evans, J. Comb. Chem., **2005**, 7, 665-672.
14. M. Tromp, S. Russu, A.J. Dent, J.F.W. Mosselmans, J. Evans*, et al.*, A.I.P., **2007**, CP 882, 858-860.
15. N. Binsted, *X-Mult*. University of Southampton, Southampton, **2006**.

APPENDICES

APPENDICES:

APPENDICES

Appendix I: Observed calculated distance plots for various samples in Chapter 4.

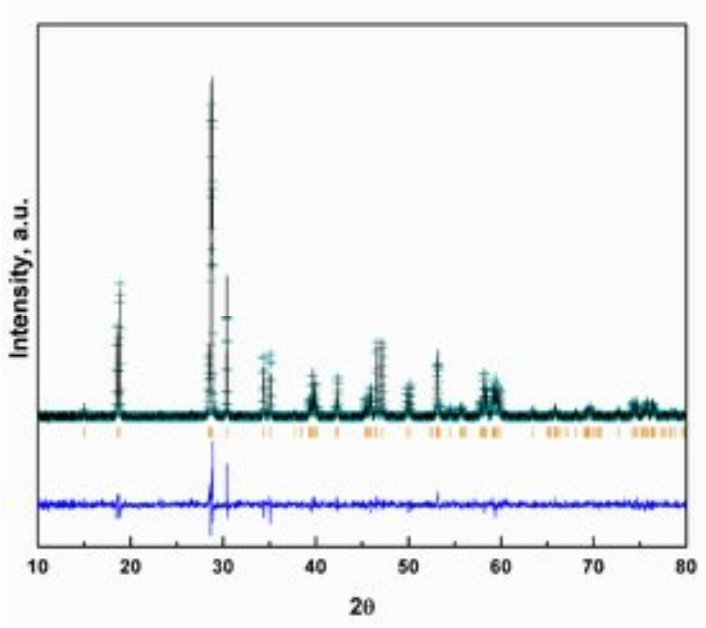

Rietveld refinement fit for the sequential sol-gel monoclinic $BiVO_4$; obtained from PXD data collected on a Siemens D5000. The cross marks are the observed intensities, the upper trace the calculated profile, the orange tick marks the calculated scheelite peak positions and the lower line the difference.

Appendix II: Observed calculated distance plots for various samples in Chapter 4.

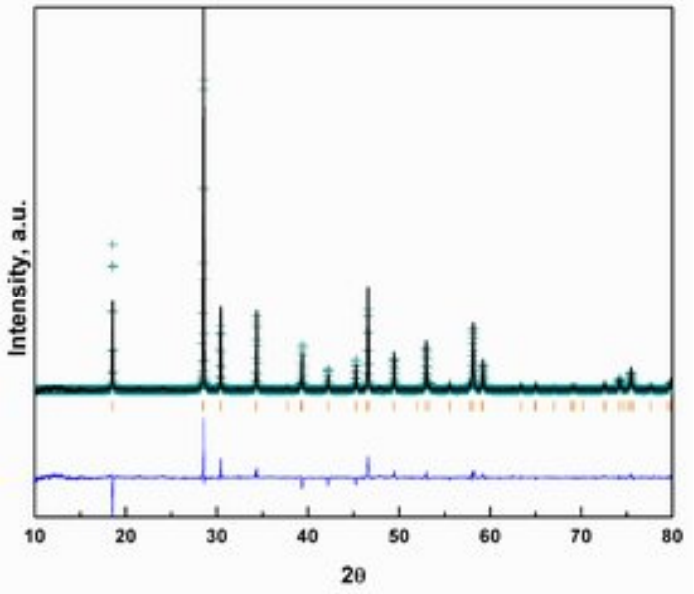

Rietveld refinement fit for the sequential sol-gel tetragonal BiMoVOX; obtained from PXD data collected on a Siemens D5000. The cross marks are the observed intensities, the upper trace the calculated profile, the orange tick marks the calculated scheelite peak positions and the lower line the difference.

Appendix III: XRD powder data refinement of sequential sol-gel $Bi_{1-x/3}Mo_xV_{1-x}O_4$ ($0.00 \leq x \leq 0.45$) in Chapter 4.

Cell par.	0.00	0.05	0.10	0.15	0.20	0.25	0.30	0.35	0.40	0.45
a (Å)	5.1909(2)	5.1795(2)	5.1606(3)	5.1541(2)	5.1592(2)	5.1709(2)	5.1802(2)	5.1835(2)	5.1928(1)	5.1981(1)
b (Å)	5.0899(2)	5.1028(2)	5.1349(3)	a	a	a	a	a	a	a
c (Å)	11.6963(4)	11.6853(4)	11.6723(5)	11.6780(4)	11.6744(5)	11.6818(5)	11.6883(5)	11.6865(4)	11.6981(3)	11.7063(4)
γ (°)	90.374(2)	90.254(3)	90.074(1)	90	90	90	90	90	90	90
Vol. $(Å)^3$	309.03(2)	308.84(2)	309.30(3)	310.23(2)	310.74(2)	312.35(2)	313.65(2)	314.00(2)	315.44(1)	316.31(2)
Rp	0.1294	0.2081	0.1619	0.1992	0.1304	0.1623	0.1270	0.1565	0.1386	0.1754
CHI**2	1.481	2.870	2.549	2.166	2.044	2.046	1.538	2.106	1.289	1.914
Bi $_{Ui/Ue*100}$	1.64	2.77	3.10	2.51	2.91	2.06	3.47	4.35	2.45	3.78
V $_{Ui/Ue*100}$	1.08	1.74	2.50	2.89	2.50	2.50	2.50	2.50	2.50	2.50
Mo $_{Ui/Ue*100}$	-	-	-	2.89	2.50	2.50	2.50	2.50	2.50	2.50
O $_{Ui/Ue*100}$	1.11	1.27	2.50	2.50	2.50	2.50	2.50	2.50	2.50	2.50

Appendix IV: XRD powder data refinement of sequential calcinations $Bi_{1-x/3}Mo_xV_{1-x}O_4$ ($0.00 \leq x \leq 0.45$) in Chapter 4.

Cell par.	0.00	0.05	0.10	0.15	0.20	0.25	0.30	0.35	0.40	0.45
a (Å)	5.1959(2)	5.1755(2)	5.1587(2)	5.1602(1)	5.1648(1)	5.1720(1)	5.1869(1)	5.1849(1)	5.1869(1)	5.1961(2)
b (Å)	5.0925(2)	5.1120(2)	5.1391(2)	a	a	a	a	a	a	a
c (Å)	11.7014(4)	11.6839(4)	11.6724(4)	11.6805(2)	11.6738(3)	11.6734(3)	11.6980(3)	11.6867(3)	11.6879(3)	11.7028(5)
γ (°)	90.373(2)	90.205(3)	90.048(2)	90	90	90	90	90	90	90
Vol. $(Å)^3$	309.62(2)	309.12(2)	309.45(2)	311.02(1)	311.40(1)	312.36(1)	314.72(1)	314.18(1)	314.45(1)	315.97(2)
Rp	0.1359	0.1861	0.1975	0.1126	0.2013	0.1790	0.1247	0.1559	0.1692	0.1491
CHI**2	4.959	1.895	2.045	1.508	2.246	1.804	1.971	1.507	2.141	2.896
Bi $_{Ui/Ue*100}$	2.50	2.48	2.24	2.50	2.66	2.31	2.50	2.78	2.89	3.18
V $_{Ui/Ue*100}$	4.65	2.50	2.50	2.50	2.50	2.50	2.50	2.50	2.50	2.50
Mo $_{Ui/Ue*100}$	-	-	-	2.50	2.50	2.50	2.50	2.50	2.50	2.50
O $_{Ui/Ue*100}$	2.50	2.50	2.50	2.50	2.50	2.50	2.50	2.50	2.50	2.50

Appendix V: EXAFS Bi L3 edge data analysis of sequential sol-gel $Bi_{1-x/3}Mo_xV_{1-x}O_4$ ($0.00 \leq x \leq 0.45$) in Chapter 4.

	Atom	0.00	0.05	0.10	0.15	0.20	0.25	0.30	0.35	0.40	0.45
C.N.	O	4	4	4	4	4	4	4	4	4	4
C.N.	O	4	4	4	4	4	4	4	4	4	4
C.N.	V	4	4	4	4	4	4	4	4	4	4
C.N.	O	4	4	4	4	4	4	4	4	4	4
C.N.	V	2	2	-	-	-	-	-	-	-	-
r_1 (Å)		2.34(1)	2.35(1)	2.36(1)	2.37(2)	2.36(1)	2.35(1)	2.37(1)	2.34(1)	2.33(1)	2.31(2)
r_2 (Å)		2.63(2)	2.63(2)	2.61(2)	2.61(4)	2.60(3)	2.61(3)	2.67(3)	2.63(2)	2.61(2)	2.60(2)
r_3 (Å)		3.69(1)	3.68(1)	3.66(1)	3.66(2)	3.66(1)	3.61(1)	3.71(2)	3.68(2)	3.66(1)	3.66(2)
r_4 (Å)		3.78(2)	3.84(5)	3.80(2)	3.82(2)	3.81(2)	3.83(2)	3.89(2)	3.84(2)	3.83(2)	3.82(2)
r_5 (Å)		4.04(3)	3.99(5)	-	-	-	-	-	-	-	-
$2\sigma^2$ $(Å^2)$		0.030(2)	0.033(3)	0.031(2)	0.043(5)	0.039(3)	0.040(3)	0.040(4)	0.038(3)	0.038(3)	0.036(3)
$2\sigma^2$ $(Å^2)$		0.052(6)	0.060(10)	0.052(7)	0.074(16)	0.071(13)	0.071(14)	0.069(11)	0.062(10)	0.057(8)	0.054(8)
$2\sigma^2$ $(Å^2)$		0.022(2)	0.025(2)	0.024(3)	0.027(3)	0.029(3)	0.031(3)	0.033(5)	0.031(3)	0.034(3)	0.032(4)
$2\sigma^2$ $(Å^2)$		0.028(6)	0.042(29)	0.011(6)	0.013(6)	0.016(5)	0.018(6)	0.019(8)	0.014(5)	0.016(4)	0.014(5)
$2\sigma^2$ $(Å^2)$		0.035(23)	0.041(19)	-	-	-	-	-	-	-	-
E_f		-2(1)	-1(1)	-2(1)	-2(1)	-1(1)	-1(1)	-3(1)	-2(1)	-1(1)	0(1)
R%		20.1	25.1	27.0	34.6	26.8	28.7	28.0	34.0	27.4	33.8

Data fitted k^3-weighted in the 3 Òk Ò10 ranges.

Appendix VI: EXAFS V K edge data analysis of sequential sol-gel $Bi_{1-x/3}Mo_xV_{1-x}O_4$ ($0.00 \leq x \leq 0.45$) in Chapter 4.

	Atom	0.00	0.05	0.10	0.15	0.20	0.25	0.30	0.35	0.40	0.45
C.N.	O	4	4	4	4	4	4	4	4	4	4
r_1 (Å)		1.72(1)	1.72(1)	1.73(1)	1.72(1)	1.72(1)	1.72(1)	1.72(1)	1.72(1)	1.72(1)	1.73(1)
$2\sigma^2$ (Å^2)		0.014(1)	0.013(1)	0.010(1)	0.012(1)	0.012(1)	0.013(1)	0.013(1)	0.013(1)	0.012(1)	0.012(1)
E_f		-10(1)	-10(1)	-10(1)	-10(1)	-10(1)	-10(1)	-9(1)	-9(1)	-9(1)	-10(1)
R%		28.5	26.6	30.3	25.1	25.2	25.3	25.0	27.2	23.6	25.2

Data fitted k^3-weighted in the 3 Òk Ò10 ranges.

Appendix VII: EXAFS Mo K edge data analysis of sequential sol-gel $Bi_{1-x/3}Mo_xV_{1-x}O_4$ ($0.00 \leq x \leq 0.45$) in Chapter 4.

	Atom	0.15	0.20	0.25	0.30	0.35	0.40	0.45
C.N.	O	4	4	4	4	4	4	4
r_1 (Å)		1.74(1)	1.75(1)	1.76(1)	1.74(1)	1.74(1)	1.74(1)	1.75(1)
$2\sigma^2$ (Å^2)		0.006(1)	0.006(2)	0.012(2)	0.009(2)	0.011(1)	0.011(1)	0.013(1)
E_f		-5(1)	-6(1)	-7(1)	-4(1)	-4(1)	-4(1)	-5(1)
R%		22.4	23.4	21.0	20.1	20.9	20.3	22.8

Data fitted k^1-weighted in the 3 Òk Ò10 ranges.

Appendix VIII: EXAFS Bi L3 edge data analysis of array sol-gel $Bi_{1-x/3}Mo_xV_{1-x}O_4$ ($0.00 \leq x \leq 0.45$) in Chapter 4.

	Atom	0.00	0.05	0.10	0.15	0.20	0.25	0.30	0.35	0.40	0.45
C.N.	O	4	-	-	4	4	4	4	4	4	4
C.N.	O	4	-	-	4	4	4	4	4	4	4
r_1 (Å)		2.36(3)	-	-	2.28(5)	2.36(2)	2.36(2)	2.36(2)	2.35(2)	2.33(2)	2.34(2)
r_2 (Å)		2.88(3)	-	-	2.87(4)	-	-	-	-	-	-
$2\sigma^2$ (Å^2)		0.066(4)	-	-	0.086(15)	0.060(4)	0.063(3)	0.072(4)	0.070(3)	0.078(4)	0.078(4)
$2\sigma^2$ (Å^2)		0.094(10)	-	-	0.033(8)	-	-	-	-	-	-
E_f		-6(2)	-	-	5(3)	-3(1)	-3(1)	-2(1)	-1(1)	-1(1)	-2(1)
R%		25.7	-	-	23.3	29.3	25.0	27.8	24.1	29.8	29.1

Data fitted k^3-weighted in the 3 Òk Ò10 ranges.

Appendix IX: EXAFS V K edge data analysis of array sol-gel $Bi_{1-x/3}Mo_xV_{1-x}O_4$ ($0.00 \leq x \leq 0.45$) in Chapter 4.

	Atom	0.00	0.05	0.10	0.15	0.20	0.25	0.30	0.35	0.40	0.45
C.N.	O	4	-	-	-	4	4	-	4	4	4
r_1 (Å)		1.71(1)	-	-	-	1.71(1)	1.71(1)	-	1.71(1)	1.72(1)	1.72(1)
$2\sigma^2$ (Å^2)		0.018(2)	-	-	-	0.017(3)	0.018(3)	-	0.015(2)	0.014(2)	0.014(3)
E_f		-9(1)	-	-	-	-8(1)	-9(1)	-	-9(1)	-10(1)	-10(1)
R%		24.7	-	-	-	29.9	27.7	-	26.0	31.6	43.1

Data fitted k^2-weighted in the 3 Òk Ò10 ranges.

Appendix X: EXAFS Mo K edge data analysis of sequential calcinations $Bi_{1-x/3}Mo_xV_{1-x}O_4$ ($0.00 \leq x \leq 0.45$) in Chapter 4.

	Atom	0.00	0.05	0.10	0.15	0.20	0.25	0.30	0.35	0.40	0.45
C.N.	O	-	-	-	4	4	4	4	4	4	4
r_1 (Å)		-	-	-	1.77(1)	1.77(1)	1.77(1)	1.77(1)	1.77(1)	1.77(1)	1.77(1)
$2\sigma^2$ (Å^2)		-	-	-	0.011(1)	0.009(1)	0.009(1)	0.009(1)	0.008(1)	0.007(1)	0.007(1)
E_f		-	-	-	-10(1)	-9(1)	-9(1)	-10(1)	-9(1)	-10(1)	-12(1)
R%		-	-	-	22.1	20.4	19.9	21.7	22.5	26.3	21.1

Data fitted k^3-weighted in the 3 Òk Ò7 ranges.

Appendix XI: EXAFS V K edge data analysis of sequential calcinations $Bi_{1-x/3}Mo_xV_{1-x}O_4$ ($0.00 \leq x \leq 0.45$) in Chapter 4.

	Atom	0.00	0.05	0.10	0.15	0.20	0.25	0.30	0.35	0.40	0.45
C.N.	O	4	4	4	4	4	4	4	4	4	4
r_1 (Å)		1.72(1)	1.72(1)	1.72(1)	1.72(1)	1.72(1)	1.72(1)	1.72(1)	1.73(1)	1.72(1)	1.72(1)
$2\sigma^2$ (Å^2)		0.014(1)	0.012(1)	0.012(1)	0.012(1)	0.012(1)	0.013(1)	0.013(1)	0.012(1)	0.013(1)	0.013(1)
E_f		-10(1)	-10(1)	-10(1)	-11(1)	-11(1)	-11(1)	-11(1)	-11(1)	-10(1)	-11(1)
R%		31.2	26.6	26.1	26.8	25.5	26.3	27.0	25.2	25.2	24.4

Data fitted k^3-weighted in the 3 Òk Ò10 ranges.

Appendix XII: EXAFS Mo K edge data analysis of sequential calcinations $Bi_{1-x/3}Mo_xV_{1-x}O_4$ ($0.00 \leq x \leq 0.45$) in Chapter 4.

	Atom	0.00	0.05	0.10	0.15	0.20	0.25	0.30	0.35	0.40	0.45
C.N.	O	-	-	-	-	4	4	4	4	4	4
r_1 (Å)		-	-	-	-	1.75(1)	1.75(1)	1.74(1)	1.75(1)	1.75(1)	1.75(1)
$2\sigma^2$ (Å^2)		-	-	-	-	0.015(2)	0.018(2)	0.015(2)	0.013(1)	0.011(1)	0.010(1)
E_f		-	-	-	-	-7(1)	-7(1)	-7(1)	-7(1)	-7(1)	-7(1)
R%		-	-	-	-	22.4	23.7	21.8	20.8	19.6	18.7

Data fitted k^1-weighted in the 3 Òk Ò10 ranges.

Appendix XIII: Results of the Raman spectral analysis (cm^{-1}) of sequential sol-gel $Bi_{1-x/3}Mo_xV_{1-x}O_4$ ($0.00 \leq x \leq 0.45$) in Chapter 4.

Vibr. mode	0.00	0.05	0.10	0.15	0.20	0.25	0.30	0.35	0.40	0.45
ν_s (Mo-O)	0	895	894	895	895	896	896	897	897	897
ν_s (V-O)	842	836	831	831	830	832	832	832	833	834
FWHM	38	49	48	46	48	57	58	62	63	72
ν_{as} (V-O)	726	728	733	734	737	746	754	755	762	771
ν_{as} (V-O)	656	659	-	-	-	-	-	-	-	-
δ_s $(VO_4)^{3-}$	383	379	373	371	369	365	364	362	363	360
δ_{as} $(VO_4)^{3-}$	343	348	352	354	353	354	354	353	352	351
Ext. mode	293	289	287	278	276	271	270	266	265	264
Ext. mode	227	226	223	223	221	219	219	217	216	216
Ext. mode	187	183	178	177	176	179	181	180	181	191
Ext. mode	160	159	156	155	157	161	162	160	162	166
Ext. mode	145	145	143	143	145	147	146	146	147	149

Appendix XIV: Results of the Raman spectral analysis (cm^{-1}) of sequential calcinations $Bi_{1-x/3}Mo_xV_{1-x}O_4$ ($0.00 \leq x \leq 0.45$) in Chapter 4.

Vibr. mode	0.00	0.05	0.10	0.15	0.20	0.25	0.30	0.35	0.40	0.45
ν_s (Mo-O)	0	887	889	888	892	893	888	895	895	895
ν_s (V-O) FWHM	830 77	829 59	829 61	829 65	829 69	830 73	827 79	831 76	831 81	832 79
ν_{as} (V-O)	-	-	-	-	-	-	-	-	-	-
ν_{as} (V-O)	-	-	-	-	-	-	-	-	-	-
$\delta_s (VO_4)^{3-}$	354	358	357	355	354	353	348	352	350	350
$\delta_{as} (VO_4)^{3-}$	-	-	-	-	-	-	-	-	-	-
Ext. mode	-	-	-	-	-	-	-	-	-	-
Ext. mode	-	-	-	-	-	-	-	-	-	-
Ext. mode	170	165	165	167	164	165	169	168	170	171
Ext. mode	-	-	-	-	-	-	-	-	-	-
Ext. mode	145	145	145	147	146	146	148	148	149	149

Appendix XV: Results of the Raman spectral analysis (cm^{-1}) of sequential array sol-gel $Bi_{1-x/3}Mo_xV_{1-x}O_4$ ($0.00 \leq x \leq 0.45$) in Chapter 4.

Vibr. mode	0.00	0.05	0.10	0.15	0.20	0.25	0.30	0.35	0.40	0.45
ν_s (Mo-O)	0	-	-	885	883	883	882	884	-	-
ν_s (V-O) FWHM	831 40	-	-	826 43	826 43	819 48	820 57	820 62	-	-
ν_{as} (V-O)	715	-	-	720	720	729	738	-	-	-
ν_{as} (V-O)	645	-	-	641	646	-	-	-	-	-
$\delta_s (VO_4)^{3-}$	371	-	-	368	367	358	343	341	-	-
$\delta_{as} (VO_4)^{3-}$	332	-	-	334	335	341	-	-	-	-
Ext. mode	279	-	-	277	276	262	240	227	-	-
Ext. mode	216	-	-	215	215	210	205	194	-	-
Ext. mode	171	-	-	174	172	167	168	159	-	-
Ext. mode	148	-	-	149	148	148	149	146	-	-
Ext. mode	134	-	-	133	133	134	135	134	-	-

Appendix XVI: Combined XRD/EXAFS data refinement of sequential sol-gel $Bi_{1-x/3}Mo_xV_{1-x}O_4$ (x = 0.00, and x = 0.45) in Chapter 4.

Cell par.	0.00	0.45
a (Å)	5.1928(2)	5.1997(1)
b (Å)	5.0918(2)	5.1997(1)
c (Å)	11.7005(4)	11.7099(4)
α (°)	90	90
β (°)	90	90
γ (°)	90.374(2)	90
Vol. $(Å)^3$	-	-
Rp	0.1690	0.2107

Edge	Atom		0.00	0.45
V K	O	C.N.	2	4
		r_1 (Å)	1.70(1)	1.73(1)
		$2\sigma^2$ ($Å^2$)	0.012(1)	0.011(1)
	O	C.N.	2	-
		r_2 (Å)	1.75(1)	-
		$2\sigma^2$ ($Å^2$)	0.013(1)	-
		E_f	-8	-8
		R%	24.2	18.6
Mo K	O	C.N.	-	4
		r_1 (Å)	-	1.75(1)
		$2\sigma^2$ ($Å^2$)	-	0.012(1)
		E_f	-	-3
		R%	-	27.7

Appendix XVII: Observed calculated distance plots for various samples in Chapter 5.

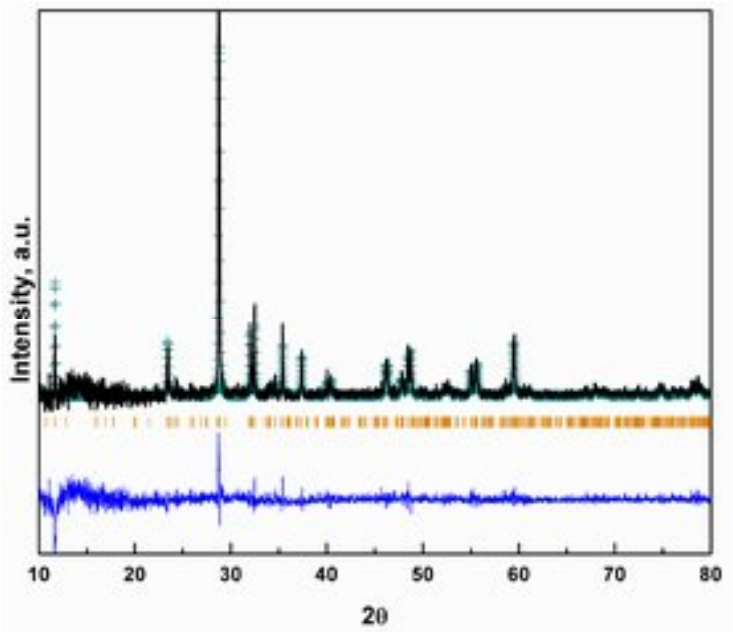

Rietveld refinement fit for the sequential sol-gel monoclinic $Bi_2VO_{5.5}$; obtained from PXD data collected on a Siemens D5000. The cross marks are the observed intensities, the upper trace the calculated profile, the orange tick marks the calculated scheelite peak positions and the lower line the difference.

Appendix XVIII: Observed calculated distance plots for various samples in Chapter 5.

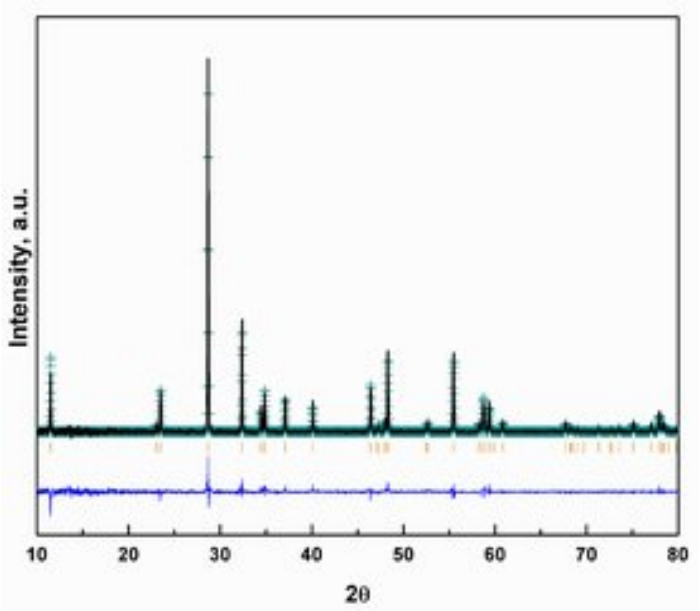

Rietveld refinement fit for the sequential sol-gel tetragonal BiFeVOX, x = 0.15; obtained from PXD data collected on a Siemens D5000. The cross marks are the observed intensities, the upper trace the calculated profile, the orange tick marks the calculated scheelite peak positions and the lower line the difference.

Appendix XIX: XRD powder data refinement of sequential sol-gel BiCuVOX (0.00 ≤ x ≤ 0.25) in Chapter 5.

Cell par.	0.00	0.05	0.10	0.15	0.20	0.25
A (Å)	16.5611(2)	3.9199(3)	3.9109(1)	3.9141(2)	3.9149(2)	3.9179(2)
B (Å)	5.5946(6)	a	a	a	a	a
C (Å)	15.2325(8)	15.3766(15)	15.4285(9)	15.4285(9)	15.4257(4)	15.4399(8)
γ (°)	90.233(2)	90	90	90	90	90
Vol. (Å)^3	1411.3(2)	236.27(4)	235.71(2)	236.37(2)	236.42(1)	237.00(2)
Rp	0.2189	0.2962	0.3084	0.2412	0.2177	0.1666
CHI**2	1.351	1.532	1.343	1.355	2.544	3.064
Bi $_{Ui/Ue*100}$	2.50	2.50	2.50	2.50	2.50	2.50
V $_{Ui/Ue*100}$	2.50	2.50	2.50	2.50	2.50	2.50
Cu $_{Ui/Ue*100}$	2.50	2.50	2.50	2.50	2.50	2.50
O $_{Ui/Ue*100}$	2.50	2.50	2.50	2.50	2.50	2.50

Appendix XX: XRD powder data refinement of array sol-gel BiCuVOX (0.00 ≤ x ≤ 0.25) in Chapter 5.

Cell par.	0.00	0.05	0.10	0.15	0.20	0.25
a (Å)	16.573(3)	3.9192(4)	3.9195(3)	3.9212(3)	3.9207(9)	3.9099(9)
b (Å)	5.590(1)	a	a	a	a	a
c (Å)	15.255(2)	15.451(2)	15.476(1)	15.435(2)	15.459(4)	15.433(5)
γ (°)	90.15(1)	90	90	90	90	90
Vol. (Å)^3	1413.3(4)	237.33(5)	237.75(3)	237.33(4)	237.64(10)	235.92(11)
Rp	0.2988	0.3677	0.4662	0.4555	0.3983	0.3918
CHI**2	0.8643	1.053	1.842	1.296	0.9248	1.952
Bi $_{Ui/Ue*100}$	2.50	2.50	2.50	2.50	2.50	2.50
V $_{Ui/Ue*100}$	2.50	2.50	2.50	2.50	2.50	2.50
Cu $_{Ui/Ue*100}$	2.50	2.50	2.50	2.50	2.50	2.50
O $_{Ui/Ue*100}$	2.50	2.50	2.50	2.50	2.50	2.50

Appendix XXI: EXAFS Bi L3 edge data analysis of sequential sol-gel BiCuVOX (0.00 ≤ x ≤ 0.20) in Chapter 5.

	Atom	0.00	0.05	0.10	0.15	0.20
C.N.	O	2	2	2	2	2
C.N.	O	2	2	2	2	2
C.N.	O	2	2	2	2	2
C.N.	O	2	2	2	2	2
C.N.	Bi	4	-	-	-	-
C.N.	V	4	-	-	-	-
r_1 (Å)		2.22(1)	2.24(1)	2.24(1)	2.24(1)	2.23(1)
r_2 (Å)		2.43(2)	2.52(2)	2.48(2)	2.49(1)	2.49(2)
r_3 (Å)		2.71(2)	2.80(1)	2.76(1)	2.77(2)	2.78(2)
r_4 (Å)		3.00(3)	3.09(5)	3.05(2)	3.06(2)	3.07(2)
r_5 (Å)		3.72(1)	-	-	-	-
r_6 (Å)		4.21(3)	-	-	-	-
$2\sigma^2$ (Å^2)		0.014(1)	0.013(2)	0.011(2)	0.011(2)	0.012(2)
$2\sigma^2$ (Å^2)		0.026(5)	0.030(8)	0.025(8)	0.025(6)	0.032(10)
$2\sigma^2$ (Å^2)		0.026(5)	0.026(7)	0.023(8)	0.023(7)	0.027(9)
$2\sigma^2$ (Å^2)		0.037(9)	0.033(7)	0.034(8)	0.040(10)	0.040(10)
$2\sigma^2$ (Å^2)		0.026(2)	-	-	-	-
$2\sigma^2$ (Å^2)		0.060(11)	-	-	-	-
E_f		-1(1)	-3(1)	-4(1)	-4(1)	-3(1)
R%		28.5	19.0	21.3	21.1	19.1

Data (x=0.00) fitted k^3 weighted in the 3 Òk Ò12 ranges.
Data (0.05 Òx Ò0.20) fitted k^1 weighted in the 3 Òk Ò12 ranges.

Appendix XXII: EXAFS V K edge data analysis of sequential sol-gel BiCuVOX (0.00 ≤ x ≤ 0.15) in Chapter 5.

	Atom	0.00	0.05	0.10	0.15
C.N.	O	4	4	4	4
C.N.	O	2	2	2	2
r_1 (Å)		1.71(1)	1.72(1)	1.72(1)	1.72(1)
r_2 (Å)		2.13(4)	2.09(2)	2.08(2)	2.08(2)
$2\sigma^2$ (Å^2)		0.016(1)	0.012(1)	0.012(1)	0.010(1)
$2\sigma^2$ (Å^2)		0.056(14)	0.038(8)	0.036(10)	0.038(10)
E_f		-7(1)	-11(1)	-11(1)	-11(1)
R%		21.7	17.7	21.7	21.0

Data fitted k^2 weighted in the 3.5 Òk Ò12 ranges.

Appendix XXIII: EXAFS Cu K edge data analysis of sequential sol-gel BiCuVOX (0.05 ≤ x ≤ 0.20) in Chapter 5.

	Atom	0.05	0.10	0.15	0.20
C.N.	O	4	4	4	4
r_1 (Å)		1.89(1)	1.88(1)	1.90(1)	1.92(1)
$2\sigma^2$ (Å^2)		0.036(2)	0.029(2)	0.024(1)	0.019(2)
E_f		9(1)	9(1)	7(1)	4(1)
R%		34.3	32.7	26.9	27.8

Data fitted k^1-weighted in the 3 Òk Ò10 ranges.

Appendix XXIV: EXAFS Bi L3 edge data analysis of array sol-gel BiCuVOX (0.00 ≤ x ≤ 0.20) in Chapter 5.

	Atom	0.00	0.05	0.10	0.15	0.20
C.N.	O	1	1	1	1	1
r_1 (Å)		2.19(2)	2.19(2)	2.19(2)	2.20(2)	2.19(2)
$2\sigma^2$ (Å^2)		0.010(4)	0.011(4)	0.011(4)	0.008(3)	0.010(3)
E_f		-4(1)	-4(1)	-4(1)	-6(1)	-51)
R%		48.8	39.8	38.3	40.4	37.7

Data fitted k^1weighted in the 3 Òk Ò10 ranges.

Appendix XXV: EXAFS Cu K edge data analysis of array sol-gel BiCuVOX (0.05 ≤ x ≤ 0.25) in Chapter 5.

	Atom	0.05	0.10	0.15	0.20	0.25
C.N.	O	4	4	4	4	4
r_1 (Å)		1.92(1)	1.92(1)	1.92(1)	1.93(1)	1.92(1)
$2\sigma^2$ (Å^2)		0.021(2)	0.018(2)	0.017(2)	0.017(2)	0.012(2)
E_f		2.5(1)	1.3(1)	1.0(1)	1.0(1)	1.0(1)
R%		31.3	29.9	28.3	28.3	24.0

Data fitted k^1-weighted in the 3 Òk Ò12 ranges.

Appendix XXVI: Results of the Raman spectral analysis (cm^{-1}) of sequential sol-gel BiCuVOX ($0.00 \leq x \leq 0.25$) in Chapter 5.

Vibr. mode	0.00	0.05	0.10	0.15	0.20	0.25
ν_s $(VO_3)_n^{n-}$	922	-	-	-	-	-
ν_s (V-O) FWHM	842 61	854 62	865 50	860 57	867 53	853 65
ν_{as} (V-O-V)	797	807	830	830	836	825
ν_s (V-O)	733	744	780	789	793	789
ν_{as} (V-O)	645	688	700	702	704	721
δ_{as} $(VO_4)^{3-}$	497	457	454	470	455	408

Appendix XXVII: XRD powder data refinement of sequential sol-gel BiFeVOX ($0.00 \leq x \leq 0.30$) in Chapter 5.

Cell par.	0.00	0.05	0.10	0.15	0.20	0.25	0.30
a (Å)	16.5611(20)	16.6144(11)	3.9182(1)	3.9119(1)	3.9100(1)	3.9085(1)	3.9116(2)
b (Å)	5.5946(6)	5.5746(4)	a	a	a	a	a
c (Å)	15.2325(8)	15.3914(10)	15.4058(5)	15.4442(5)	15.4744(5)	15.5316(5)	15.5489(8)
γ (°)	90.233(2)	90.124(8)	90	90	90	90	90
Vol. $(Å)^3$	1411.3(2)	1425.5(2)	236.51(1)	236.35(1)	236.57(1)	237.27(1)	237.91(2)
Rp	0.2189	0.2137	0.1604	0.1559	0.2120	0.1436	0.1866
CHI**2	1.351	2.892	1.808	1.589	1.709	1.755	2.236
Bi $_{Ui/Ue*100}$	2.50	2.50	2.50	2.50	2.50	2.50	2.50
V $_{Ui/Ue*100}$	2.50	2.50	2.50	2.50	2.50	2.50	2.50
Fe $_{Ui/Ue*100}$	2.50	2.50	2.50	2.50	2.50	2.50	2.50
O $_{Ui/Ue*100}$	2.50	2.50	2.50	2.50	2.50	2.50	2.50

Appendix XXVIII: XRD powder data refinement of array sol-gel BiFeVOX ($0.00 \leq x \leq 0.25$) in Chapter 5.

Cell par.	0.00	0.05	0.10	0.15	0.20	0.25
a (Å)	16.573(3)	3.9260(4)	3.9213(3)	3.9209(6)	3.9218(5)	3.9215(3)
b (Å)	5.590(1)	a	a	a	a	a
c (Å)	15.255(2)	15.476(2)	15.505(1)	15.493(3)	15.494(2)	15.508(2)
γ (°)	90.15(1)	90	90	90	90	90
Vol. $(Å)^3$	1414.3(4)	238.53(4)	238.42(4)	238.17(6)	238.31(5)	238.48(3)
Rp	0.2988	0.1124	0.1025	0.1122	0.1099	0.0939
CHI**2	0.8643	0.36633	0.3255	0.8074	0.8200	0.2951
Bi $_{Ui/Ue*100}$	2.50	2.50	2.50	2.50	2.50	2.50
V $_{Ui/Ue*100}$	2.50	2.50	2.50	2.50	2.50	2.50
Fe $_{Ui/Ue*100}$	2.50	2.50	2.50	2.50	2.50	2.50
O $_{Ui/Ue*100}$	2.50	2.50	2.50	2.50	2.50	2.50

Appendix XXIX: EXAFS Bi L3 edge data analysis of sequential sol-gel BiFeVOX (0.00 ≤ x ≤ 0.30) in Chapter 5.

	Atom	0.00	0.05	0.10	0.15	0.20	0.25	0.30
C.N.	O	2	2	2	2	2	2	2
C.N.	O	2	2	2	2	2	2	2
C.N.	O	2	2	2	2	2	2	2
C.N.	O	2	2	2	2	2	2	2
C.N.	Bi	4	-	-	-	-	-	-
C.N.	V	4	-	-	-	-	-	-
r_1 (Å)		2.22(1)	2.24(1)	2.24(1)	2.24(1)	2.24(1)	2.25(1)	2.23(1)
r_2 (Å)		2.43(2)	2.48(1)	2.48(1)	2.50(2)	2.51(1)	2.47(2)	2.47(1)
r_3 (Å)		2.71(2)	2.74(2)	2.74(2)	2.75(2)	2.77(2)	2.73(3)	2.74(2)
r_4 (Å)		3.00(3)	3.04(2)	3.05(2)	3.06(2)	3.09(2)	3.03(3)	3.03(3)
r_5 (Å)		3.72(1)	-	-	-	-	-	-
r_6 (Å)		4.21(3)	-	-	-	-	-	-
$2\sigma^2$ (Å^2)		0.014(1)	0.011(2)	0.011(2)	0.011(2)	0.011(1)	0.011(2)	0.011(2)
$2\sigma^2$ (Å^2)		0.026(5)	0.023(5)	0.021(6)	0.027(8)	0.021(5)	0.028(10)	0.027(7)
$2\sigma^2$ (Å^2)		0.026(5)	0.024(7)	0.024(7)	0.028(10)	0.024(7)	0.030(12)	0.029(9)
$2\sigma^2$ (Å^2)		0.037(9)	0.040(9)	0.042(9)	0.039(9)	0.044(10)	0.049(15)	0.053(13)
$2\sigma^2$ (Å^2)		0.026(2)	-	-	-	-	-	-
$2\sigma^2$ (Å^2)		0.060(11)	-	-	-	-	-	-
E_f		-1(1)	-3(1)	-3(1)	-3(1)	-5(1)	-3(1)	-3(1)
R%		28.5	21.0	23.0	21.8	23.2	21.8	19.1

Data (x=0.00) fitted k^3 weighted in the 3 Òk Ò12 ranges.
Data (0.05 Òx Ò0.20) fitted k^1 weighted in the 3 Òk Ò12 ranges.

Appendix XXX: EXAFS Fe K edge data analysis of sequential sol-gel BiFeVOX (0.20 ≤ x ≤ 0.25) in Chapter 5.

	Atom	0.20	0.25
C.N.	O	4	4
r_1 (Å)		2.00(2)	1.97(2)
$2\sigma^2$ (Å^2)		0.022(3)	0.031(4)
E_f		-2(1)	0(2)
R%		46.9	51.3

Data fitted k^1-weighted in the 3 Òk Ò10 ranges.

Appendix XXXI: Results of the Raman spectral analysis (cm^{-1}) of sequential sol-gel BiFeVOX (0.00 ≤ x ≤ 0.30) in Chapter 5.

Vibr. mode	0.00	0.05	0.10	0.15	0.20	0.25	0.30
ν_s $(VO_3)_n^{n-}$	922	920	910	-	-	-	-
ν_s (V-O) FWHM	842 61	847 55	851 66	851 66	855 65	852 64	846 62
ν_{as} (V-O-V)	797	800	801	806	810	818	-
ν_s (V-O)	733	737	733	713	715	709	714
ν_{as} (V-O)	645	654	676	604	-	605	610
δ_{as} $(VO_4)^{3-}$	497	-	-	-	-	-	-

Appendix XXXII: Observed calculated distance plots for various samples in Chapter 6.

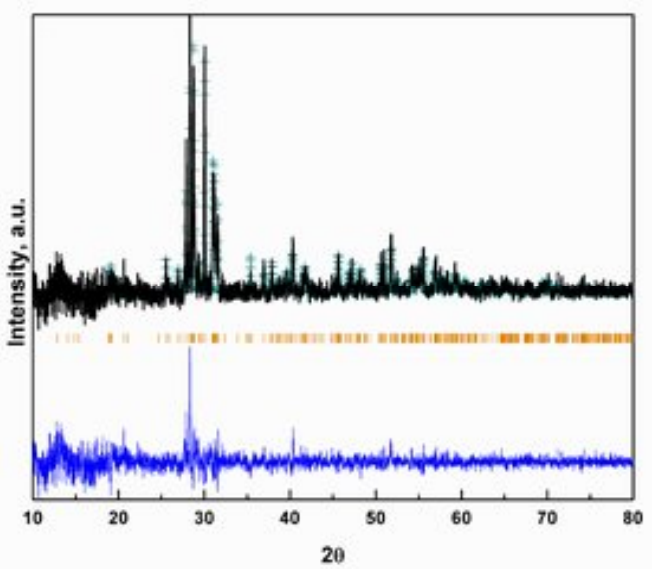

Rietveld refinement fit for the sequential sol-gel triclinic $(Ca_{2-x},Pb_x)V_2O_7$, x = 0.30; obtained from PXD data collected on a Siemens D5000. The cross marks are the observed intensities, the upper trace the calculated profile, the orange tick marks the calculated scheelite peak positions and the lower line the difference.

Appendix XXXIII: XRD powder data refinement of sequential sol-gel $(Ca,Cd)_2V_2O_7$ (0.00 ≤ x ≤ 0.30) in Chapter 6.

Cell par.	0.00	0.05	0.10	0.15	0.20	0.25	0.30
a (Å)	6.6635(4)	6.6458(5)	6.6465(6)	6.6445(6)	6.6432(6)	6.6423(6)	6.6407(7)
b (Å)	6.9209(4)	6.9029(5)	6.9045(6)	6.9057(6)	6.9078(6)	6.9059(6)	6.9055(7)
c (Å)	7.0143(4)	6.9972(5)	6.9990(6)	6.9976(7)	6.9982(7)	6.9980(7)	6.9973(8)
α (°)	86.488(4)	86.347(4)	86.346(5)	86.247(5)	86.155(6)	86.969(6)	86.875(6)
β (°)	63.864(3)	63.842(4)	63.841(4)	63.822(4)	63.809(4)	63.795(5)	63.785(5)
γ (°)	83.719(4)	83.574(4)	83.569(5)	83.465(5)	83.349(5)	83.160(5)	83.054(6)
Vol. $(Å)^3$	288.63(3)	286.27(4)	286.44(4)	288.24(5)	286.19(5)	285.90(5)	285.70(5)
Rp	0.2126	0.1152	0.1620	0.1195	0.1319	0.1180	0.1243
CHI**2	5.960	1.690	2.065	1.717	1.831	1.676	1.718
Ca $_{Ui/Ue*100}$	2.50	2.50	2.50	2.50	2.50	2.50	2.50
V $_{Ui/Ue*100}$	2.50	2.50	2.50	2.50	2.50	2.50	2.50
Pb $_{Ui/Ue*100}$	2.50	2.50	2.50	2.50	2.50	2.50	2.50
O $_{Ui/Ue*100}$	2.50	2.50	2.50	2.50	2.50	2.50	2.50

Appendix XXXIV: EXAFS Ca K edge data analysis of sequential sol-gel $(Ca,Cd)_2V_2O_7$ (0.05 ≤ x ≤ 0.20) in Chapter 6.

	Atom	0.05	0.10	0.15	0.20
C.N.	O	3	3	3	3
C.N.	V	1	1	1	1
r_1 (Å)		2.36(1)	2.37(1)	2.36(1)	2.36(1)
r_2 (Å)		3.65(4)	3.64(3)	3.64(3)	3.62(3)
$2\sigma^2$ $(Å^2)$		0.010(3)	0.012(2)	0.010(2)	0.006(2)
$2\sigma^2$ $(Å^2)$		0.015(13)	0.009(8)	0.011(9)	0.009(8)
E_f		-4(1)	-5(1)	-4(1)	-4(1)
R%		33.1	27.9	26.0	28.5

Data (0.05 Òx Ò0.20) fitted k^1 weighted in the 3 Òk Ò10 ranges.

Appendix XXXV: EXAFS Cd K edge data analysis of sequential sol-gel $(Ca,Cd)_2V_2O_7$ ($0.05 \leq x \leq 0.25$) in Chapter 6.

	Atom	0.05	0.10	0.15	0.20	0.25
C.N.	O	6	6	6	6	6
C.N.	V	4	4	4	4	4
r_1 (Å)		2.28(1)	2.27(1)	2.28()	2.28(1)	2.29(1)
r_2 (Å)		3.56(1)	3.56(1)	3.56(1)	3.56(1)	3.57(1)
$2\sigma^2$ (Å^2)		0.019(1)	0.020(1)	0.020(1)	0.020(1)	0.018(1)
$2\sigma^2$ (Å^2)		0.018(2)	0.017(2)	0.017(2)	0.017(2)	0.016(2)
E_f		-8(1)	-8(1)	-8(1)	-7(1)	-7(1)
R%		11.6	10.3	10.7	11.1	11.7

Data 0.05 Òx Ò0.25 fitted k^1 weighted in the 3 Òk Ò10 ranges.

Appendix XXXVI: EXAFS V K edge data analysis of array sol-gel $(Ca,Cd)_2V_2O_7$ ($0.05 \leq x \leq 0.30$) in Chapter 6.

	Atom	0.05	0.10	0.15	0.20	0.25	0.30
C.N.	O	4	4	4	4	4	4
r_1 (Å)		1.59(1)	1.59(1)	1.61(1)	1.59(1)	1.64(1)	1.60(1)
$2\sigma^2$ (Å^2)		0.012(1)	0.011(1)	0.012(1)	0.007(1)	0.011(1)	0.007(1)
E_f		7(1)	8(1)	4(1)	8(1)	0(1)	6(1)
R%		15.3	15.8	14.5	16.4	15.0	15.0

Data fitted k^1-weighted in the 4 Òk Ò9 ranges.

Appendix XXXVII: Results of the Raman spectral analysis (cm^{-1}) of sequential sol-gel $(Ca,Cd)_2V_2O_7$ ($0.00 \leq x \leq 0.30$) in Chapter 6.

Vibr. mode	0.00	0.05	0.10	0.15	0.20	0.25	0.30
ν_s (V-O)	944	954	954	953	952	952	953
ν_s (V-O)	881	892	892	893	894	895	894
ν_s (V-O)	864	875	875	875	875	875	875
ν_s (V-O)	804	814	815	814	813	813	813
ν_s (V-O)	785	796	796	796	795	795	796
ν_s (V-O-V)	704	716	720	718	720	720	720
ν_s (V-O-V)	546	557	556	557	557	557	557
δ_s $(VO_4)^{3-}$	465	477	459	477	477	477	477
δ_s $(VO_4)^{3-}$	426	438	437	437	437	437	437
δ_s $(VO_4)^{3-}$	394	406	407	405	405	406	406

Appendix XXXVIII: Results of the Raman spectral analysis (cm^{-1}) of array sol-gel $(Ca,Cd)_2V_2O_7$ ($0.05 \leq x \leq 0.30$)in Chapter 6.

Vibr. mode	0.05	0.10	0.15	0.20	0.25	0.30
ν_s (V-O)	746	944	943	943	944	940
ν_s (V-O)	885	884	885	886	898	890
ν_s (V-O)	866	864	865	866	866	865
ν_s (V-O)	809	806	802	802	803	802
ν_s (V-O)	787	786	785	784	786	784
ν_s (V-O-V)	708	711	712	714	712	713
ν_s (V-O-V)	549	549	547	547	548	546
δ_s $(VO_4)^{3-}$	467	462	465	467	465	467
δ_s $(VO_4)^{3-}$	428	427	427	426	428	425
δ_s $(VO_4)^{3-}$	396	395	395	395	393	394

Appendix XXXIX: XRD powder data refinement of sequential sol-gel $(Ca,Pb)_2V_2O_7$ ($0.00 \leq x \leq 0.40$) in Chapter 6.

Cell par.	0.00	0.05	0.10	0.15	0.20	0.25	0.30	0.35	0.40
a (Å)	6.6635(4)	6.6509(4)	6.6548(7)	6.6550(8)	6.6596(7)	6.6602(7)	6.6596(7)	6.6640(5)	6.6638(8)
b (Å)	6.9209(4)	6.9104(4)	6.9141(7)	6.9214(8)	6.9290(7)	6.9322(7)	6.9332(7)	6.9383(5)	6.9362(8)
c (Å)	7.0143(4)	7.0051(5)	7.0103(8)	7.0161(8)	7.0241(8)	7.0257(8)	7.0275(7)	7.0332(6)	7.0320(8)
α (°)	86.488(4)	86.483(4)	86.527(6)	86.589(6)	86.602(6)	86.658(6)	86.686(5)	86.702(4)	86.684(7)
β (°)	63.864(3)	63.835(3)	63.812(5)	63.589(6)	63.816(4)	63.814(5)	63.805(4)	63.789(4)	63.787(6)
γ (°)	83.719(4)	83.704(4)	83.743(6)	83.767(6)	83.766(6)	83.811(6)	83.834(5)	83.844(4)	83.848(7)
Vol. $(Å)^3$	288.63(3)	287.19(3)	287.70(5)	288.28(6)	289.12(5)	289.37(6)	289.45(5)	290.06(4)	289.89(6)
Rp	0.2126	0.1255	0.1300	0.1194	0.1368	0.1367	0.1144	0.1290	0.1163
CHI**2	5.960	1.968	1.792	1.830	1.720	1.522	1.543	1.655	1.779
Ca $_{Ui/Ue*100}$	2.50	2.50	2.50	2.50	2.50	2.50	2.50	2.50	2.50
V $_{Ui/Ue*100}$	2.50	2.50	2.50	2.50	2.50	2.50	2.50	2.50	2.50
Pb $_{Ui/Ue*100}$	2.50	2.50	2.50	2.50	2.50	2.50	2.50	2.50	2.50
O $_{Ui/Ue*100}$	2.50	2.50	2.50	2.50	2.50	2.50	2.50	2.50	2.50

Appendix XL: EXAFS Ca K edge data analysis of sequential sol-gel $(Ca,Pb)_2V_2O_7$ ($0.00 \leq x \leq 0.35$) in Chapter 6.

	Atom	0.00	0.10	0.15	0.20	0.25	0.30	0.35
C.N.	O	3	4	4	4	4	4	4
C.N.	V	2	2	2	2	2	2	2
r_1 (Å)		2.37(1)	2.38(1)	2.38(1)	2.40(1)	2.37(1)	2.37(1)	2.37(1)
r_2 (Å)		3.67(3)	3.66(3)	3.68(3)	3.64(3)	3.66(4)	3.66(4)	3.67(4)
$2\sigma^2$ $(Å^2)$		0.024(2)	0.022(2)	0.021(2)	0.014(3)	0.014(2)	0.012(2)	0.010(2)
$2\sigma^2$ $(Å^2)$		0.035(9)	0.028(10)	0.026(9)	0.022(10)	0.029(12)	0.030(14)	0.028(13)
E_f		-5(1)	-5(1)	-5(1)	-5(1)	-5(1)	-5(1)	-5(1)
R%		24.2	22.9	22.7	28.3	24.4	27.0	26.4

Data (0.00 Òx Ò0.35) fitted k^1 weighted in the 3 Òk Ò10 ranges.

Appendix XLI: EXAFS Pb L3 edge data analysis of sequential sol-gel $(Ca,Pb)_2V_2O_7$ ($0.05 \leq x \leq 0.35$) in Chapter 6.

	Atom	0.05	0.20	0.25	0.30	0.35
C.N.	O	6	6	6	6	6
C.N.	O	-	1	1	1	1
C.N.	V	4	4	4	4	4
r_1 (Å)		2.47(1)	2.49(1)	2.47(1)	2.48(1)	2.48(1)
r_2 (Å)		-	2.91(4)	2.89(7)	2.88(8)	2.89(5)
r_3 (Å)		3.70(2)	3.77(1)	3.77(1)	3.77(1)	3.78(1)
$2\sigma^2$ $(Å^2)$		0.038(2)	0.038(2)	0.040(2)	0.040(2)	0.042(2)
$2\sigma^2$ $(Å^2)$		-	0.029(12)	0.050(25)	0.051(30)	0.041(19)
$2\sigma^2$ $(Å^2)$		0.024(5)	0.037(3)	0.041(3)	0.036(3)	0.042(4)
E_f		-1(1)	-3(1)	-2(1)	-2(1)	-2(1)
R%		27.9	23.9	25.3	27.6	22.1

Data (0.05 Òx Ò0.35) fitted k^3 weighted in the 3 Òk Ò10 ranges.

Appendix XLII: EXAFS V K edge data analysis of sequential sol-gel $(Ca,Pb)_2V_2O_7$ ($0.05 \leq x \leq 0.35$) in Chapter 6.

	Atom	0.05	0.35
C.N.	O	2	2
C.N.	V	1	1
r_1 (Å)		1.71(1)	1.70(1)
r_2 (Å)		2.88(2)	2.87(2)
$2\sigma^2$ $(Å^2)$		0.015(1)	0.007(1)
$2\sigma^2$ $(Å^2)$		0.027(6)	0.023(6)
E_f		-13(1)	-12(1)
R%		27.5	21.1

Data fitted k^2-weighted in the 3.5 Òk Ò10 ranges.

Appendix XLIII: EXAFS V K edge data analysis of array sol-gel $(Ca,Pb)_2V_2O_7$ ($0.00 \leq x \leq 0.25$) in Chapter 6.

	Atom	0.00	0.05	0.10	0.15	0.20	0.25
C.N.	O	4	4	4	4	4	4
r_1 (Å)		1.57(2)	1.63(1)	1.65(1)	1.66(1)	1.65(1)	1.64(1)
$2\sigma^2$ (Å^2)		0.012(2)	0.006(1)	0.007(1)	0.007(1)	0.006(1)	0.005(1)
E_f		9(1)	-2(1)	-4(1)	-6(1)	-6(1)	-4(1)
R%		24.6	13.9	14.8	14.6	15.9	18.6

Data fitted k^1-weighted in the 4 Òk Ò9 ranges.

Appendix XLIV: Results of the Raman spectral analysis (cm^{-1}) of sequential sol-gel $(Ca,Pb)_2V_2O_7$ ($0.00 \leq x \leq 0.35$) in Chapter 6.

Vibr. mode	0.00	0.05	0.10	0.15	0.20	0.25	0.30	0.35
ν_s (V-O)	944	941	941	940	940	938	937	937
ν_s (V-O)	881	877	878	877	877	875	875	874
ν_s (V-O)	864	862	862	862	862	859	858	857
ν_s (V-O)	804	801	801	801	802	801	800	799
ν_s (V-O)	785	784	784	784	785	783	782	781
ν_s (V-O-V)	704	703	701	699	699	699	697	697
ν_s (V-O-V)	546	543	543	542	542	541	541	540
δ_s $(VO_4)^{3-}$	465	461	465	464	465	465	465	465
δ_s $(VO_4)^{3-}$	426	424	425	424	424	423	423	422
δ_s $(VO_4)^{3-}$	394	391	393	391	392	392	391	391

Appendix XLV: Results of the Raman spectral analysis (cm^{-1}) of array sol-gel $(Ca,Pb)_2V_2O_7$ ($0.00 \leq x \leq 0.35$) in Chapter 6.

Vibr. mode	0.00	0.05	0.10	0.15	0.20	0.25
ν_s (V-O)	-	-	926	924	925	-
ν_s (V-O)	869	869	864	864	862	868
ν_s (V-O)	831	835	847	845	845	840
ν_s (V-O)	803	803	789	778	786	802
ν_s (V-O)	-	-	769	769	767	-
ν_s (V-O-V)	-	-	684	680	684	-
ν_s (V-O-V)	-	-	528	530	526	546
δ_s $(VO_4)^{3-}$	414	417	449	-	448	418
δ_s $(VO_4)^{3-}$	398	399	408	408	408	-
δ_s $(VO_4)^{3-}$	357	356	376	378	375	355

Appendix XLVI: XRD powder data refinement of sequential sol-gel $(Ca,Sr)_2V_2O_7$ ($0.00 \leq x \leq 0.30$) in Chapter 6.

Cell par.	0.00	0.05	0.10	0.15	0.20	0.25	0.30
a (Å)	6.6635(4)	6.6514(5)	6.6426(7)	6.6565(4)	6.6549(6)	6.6589(5)	6.6556(8)
b (Å)	6.9209(4)	6.9087(5)	6.9015(7)	6.9167(4)	6.9196(6)	6.9205(5)	6.9179(8)
c (Å)	7.0143(4)	7.0039(5)	6.9968(8)	7.0137(4)	7.0122(6)	7.0172(6)	7.0136(9)
α (°)	86.488(4)	86.512(4)	86.605(6)	86.677(3)	86.698(5)	86.693(4)	86686(7)
β (°)	63.864(3)	63.860(4)	63.854(5)	63.844(3)	63.846(4)	63.855(4)	63.837(6)
γ (°)	83.719(4)	83.723(4)	83.773(6)	83.818(3)	83.825(5)	83.839(4)	83.811(7)
Vol. (Å)^3	288.63(3)	287.17(4)	286.22(5)	288.14(3)	288.03(4)	288.59(4)	288.13(6)
Rp	0.2126	0.1344	0.2639	0.1242	0.1295	0.2179	0.1470
CHI**2	5.960	1.735	1.636	1.803	1.855	1.928	2.642
Ca $_{Ui/Ue*100}$	2.50	2.50	2.50	2.50	2.50	2.50	2.50
V $_{Ui/Ue*100}$	2.50	2.50	2.50	2.50	2.50	2.50	2.50
Pb $_{Ui/Ue*100}$	2.50	2.50	2.50	2.50	2.50	2.50	2.50
O $_{Ui/Ue*100}$	2.50	2.50	2.50	2.50	2.50	2.50	2.50

Appendix XLVII: EXAFS Ca K edge data analysis of sequential sol-gel $(Ca,Sr)_2V_2O_7$ ($0.05 \leq x \leq 0.25$) in Chapter 6.

	Atom	0.05	0.10	0.15	0.20	0.25
C.N.	O	3	3	3	3	3
C.N.	V	1	1	1	1	1
r_1 (Å)		2.38(1)	2.38(1)	2.38(1)	2.38(1)	2.38(1)
r_2 (Å)		3.66(3)	3.66(3)	3.66(4)	3.66(3)	3.66(4)
$2\sigma^2$ (Å^2)		0.015(2)	0.016(2)	0.012(2)	0.014(2)	0.011(2)
$2\sigma^2$ (Å^2)		0.014(9)	0.014(10)	0.016(11)	0.015(10)	0.017(12)
E_f		-5(1)	-5(1)	-5(1)	-5(1)	-5(1)
R%		27.0	27.3	26.1	25.5	27.4

Data (0.05 Òx Ò0.25) fitted k^1 weighted in the 3 Òk Ò10 ranges.

Appendix XLVIII: EXAFS Sr K edge data analysis of sequential sol-gel $(Ca,Sr)_2V_2O_7$ ($0.05 \leq x \leq 0.25$) in Chapter 6.

	Atom	0.05	0.10	0.15	0.20	0.25
C.N.	O	6	6	6	6	6
C.N.	V	4	4	4	4	2
C.N.	V	-	-	-	-	2
r_1 (Å)		2.52(1)	2.53(1)	2.53(1)	2.53(1)	2.54(1)
r_2 (Å)		3.82(2)	3.82(1)	3.83(2)	3.85(2)	3.85(3)
r_3 (Å)		-	-	-	-	3.48(3)
$2\sigma^2$ (Å^2)		0.018(1)	0.019(1)	0.018(1)	0.020(1)	0.020(1)
$2\sigma^2$ (Å^2)		0.032(5)	0.032(6)	0.034(6)	0.050(8)	0.020(6)
$2\sigma^2$ (Å^2)		-	-	-	-	0.032(8)
E_f		-4(1)	-4(1)	-4(1)	-4(1)	-4(1)
R%		19.7	17.5	17.6	16.1	16.4

Data 0.05 Òx Ò0.25 fitted k^1 weighted in the 3 Òk Ò10 ranges.

Appendix XLIX: EXAFS V K edge data analysis of array sol-gel $(Ca,Sr)_2V_2O_7$ ($0.00 \leq x \leq 0.25$) in Chapter 6.

	Atom	0.00	0.05	0.10	0.15	0.20	0.25
C.N.	O	3	3	3	3	3	3
r_1 (Å)		1.65(1)	1.65(1)	1.65(1)	1.65(1)	1.65(1)	1.65(1)
$2\sigma^2$ (Å^2)		0.014(2)	0.014(1)	0.009(1)	0.010(1)	0.017(2)	0.010(1)
E_f		-3(1)	-3(1)	-2(1)	-2(1)	-2(1)	-3(1)
R%		25.4	21.9	23.5	24.2	27.3	23.7

Data fitted k^1-weighted in the 3 Òk Ò10 ranges.

Appendix L: Results of the Raman spectral analysis (cm^{-1}) of sequential sol-gel $(Ca,Sr)_2V_2O_7$ ($0.00 \leq x \leq 0.25$) in Chapter 6.

Vibr. mode	0.00	0.05	0.10	0.15	0.20	0.25
ν_s (V-O)	944	955	955	955	955	955
ν_s (V-O)	881	891	890	889	890	889
ν_s (V-O)	864	876	876	876	876	876
ν_s (V-O)	804	816	816	816	817	816
ν_s (V-O)	785	796	796	796	796	795
ν_s (V-O-V)	704	716	714	712	714	713
ν_s (V-O-V)	546	558	557	556	558	556
δ_s $(VO_4)^{3-}$	465	478	478	478	480	478
δ_s $(VO_4)^{3-}$	426	439	439	439	439	439
δ_s $(VO_4)^{3-}$	394	406	406	406	406	406

Appendix LI: Results of the Raman spectral analysis (cm^{-1}) of array sol-gel $(Ca,Sr)_2V_2O_7$ ($0.05 \leq x \leq 0.20$) in Chapter 6.

Vibr. mode	0.05	0.10	0.15	0.20
ν_s (V-O)	947	947	947	945
ν_s (V-O)	883	883	882	879
ν_s (V-O)	867	867	866	865
ν_s (V-O)	807	807	809	806
ν_s (V-O)	788	787	787	784
ν_s (V-O-V)	706	705	702	708
ν_s (V-O-V)	549	549	549	545
δ_s $(VO_4)^{3-}$	467	467	429	470
δ_s $(VO_4)^{3-}$	429	429	396	397
δ_s $(VO_4)^{3-}$	398	397	377	380